Available online at www.sciencedirect.com
ScienceDirect
Progress in Energy and Combustion Science 33 (2007) 497–551
PROGRESS IN ENERGY AND COMBUSTION SCIENCE
www.elsevier.com/locate/pecs

Modeling of combustion and ignition of solid-propellant ingredients

Merrill W. Beckstead[a], Karthik Puduppakkam[a], Piyush Thakre[b], Vigor Yang[b,*]

[a]*Brigham Young University, Provo, UT 84602, USA*
[b]*The Pennsylvania State University, 104 Research Building East, University Park, PA 16802, USA*

Received 4 May 2006; accepted 2 February 2007
Available online 11 April 2007

Abstract

Techniques for modeling energetic-material combustion and ignition have evolved tremendously in the last two decades and have been successfully applied to various solid-propellant ingredients. There has been a paradigm shift in the predictive capability of solid-propellant combustion models as the field has advanced from a simple and global-kinetics approach to a detailed approach that employs elementary reaction mechanisms in the gas phase, and accommodates thermal decomposition and subsequent reactions in the condensed phase. The detailed models not only allow calculation of propellant burning-rate characteristics, such as pressure and temperature sensitivities, but also of the surface conditions and entire combustion-wave structure, including the spatial variations in temperature and species concentrations.

This paper provides a comprehensive review of recent advances in the modeling and simulation of various solid-propellant ingredients over a wide range of ambient conditions. The specific materials of concern include nitramines (RDX, HMX), azides (GAP), nitrate esters (NG, BTTN, TMETN), ADN, and AP monopropellants, as well as homogeneous mixtures representing binary (RDX/GAP, HMX/GAP, and AP/HTPB) and ternary (RDX/GAP/BTTN) pseudo-propellants. Emphasis is placed on the steady-state combustion and laser-induced ignition of nitramines. The capabilities and deficiencies of existing approaches are addressed. In general, the detailed gas-phase reaction mechanisms developed so far represent the chemistry of monopropellants and associated mixtures consistently well, and help understand the intricate processes of solid-propellant combustion. The reaction mechanisms in the condensed phase, however, still pose an important challenge. Furthermore, the current knowledge of the initial decomposition of molecules emerging from the propellant surface is insufficient to render the models fully predictive. Modeling is thus not yet a predictive tool, but it is a useful guide. In the near future, it is likely that detailed combustion models can assist in the formulation of advanced solid propellants meeting various performance and emission requirements.
© 2007 Elsevier Ltd. All rights reserved.

Keywords: Combustion and ignition of solid propellants; Energetic materials; Combustion modeling

*Corresponding author. Tel.: +1 814 863 1502; fax: +1 814 865 3389.
E-mail address: vigor@psu.edu (V. Yang).

0360-1285/$ - see front matter © 2007 Elsevier Ltd. All rights reserved.
doi:10.1016/j.pecs.2007.02.003

Contents

1. Introduction

A solid propellant consists of several chemical ingredients such as oxidizer, fuel, binder, plasticizer, curing agent, stabilizer, and cross-linking agent. The specific chemical composition depends on the desired combustion characteristics for a particular application. Two main types of propellants (homogeneous and heterogeneous) are distinguished by the condition in which their constituent ingredients are interconnected. In a homogeneous propellant, the ingredients are linked chemically and the resulting physical structure is homogeneous throughout. Typical examples of homogeneous propellants are single-base (NC nitrocellulose) or double-base (NC and NG nitroglycerine) propellants. In a heterogeneous or composite propellant, the ingredients are physically mixed, leading to a heterogeneous physical structure. It is composed of crystalline particles acting as oxidizer and organic plastic fuels acting as binder to adhere oxidizer particles together [1]. The ingredients often used as oxidizers are ammonium perchlorate (AP), ammonium nitrate (AN), ammonium dintramide (ADN), cyclotrimethylenetrinitramine (RDX), and cyclotetramethylenetetranitramine (HMX). The most commonly employed binders are either inert (typically HTPB, hydroxyl-terminated polybutadiene, with various plasticizers, ballistic modifiers, and cross-linking agents), or active (NG and NC, polyether polymer, and azide polymer such as GAP glycidyl azide polymer, BAMO bis-azidomethyl oxetane, and AMMO 3-azidomethyl-3-methyl oxetane) [1,2].

The quest for more energetic propellants with reduced pollutant emissions has resulted in the use of several non-AP ingredients in solid propellants. The ingredients belong to a wide spectrum of chemical families, but mostly fall into one of four categories:

Nomenclature

A	cross-sectional area of propellant sample
A_g	fractional cross-sectional area consisting of gas bubbles in two-phase region
A_j	pre-exponential factor for rate constant in reaction j
A_s	liquid–gas interface area per unit volume
a	pre-exponential factor in burning-rate law
B_j	temperature exponent for rate constant in reaction j
C_i	molar concentration of species i
C_p, c_{pi}	constant-pressure specific heat of species i
E_j	activation energy for reaction j
e	internal energy
H_v	enthalpy of vaporization
h	enthalpy
h_i	static enthalpy of species i
$h^\circ_{f_i}$	standard heat of formation of species i
k_j	rate constant for reaction j
$\dot{m}''$	mass flux
N	total number of species
n	pressure exponent
N_R	total number of reactions
p	pressure
p_o	pre-exponential factor for vapor pressure in Arrhenius form
r_b	propellant burning rate
R_u	universal gas constant
T	temperature
T_o	preconditioned temperature
s	sticking coefficient
t	time
u	bulk velocity
V_i	diffusion velocity of species i
$\dot{Q}''_{laser}$	external laser heat flux
$\dot{Q}'''_{rad}$	volumetric absorption of laser energy
W_i	molecular weight of species i
$\dot{w}_i$	mass production rate of species i
$\dot{w}_{Rj}$	mass production rate of reaction j
X_i	molar fraction of species i
x	spatial coordinate
Y_i	mass fraction of species i

Greek symbols

ϕ	void fraction
ρ	density
λ	thermal conductivity
$\dot{\omega}$	molar production rate

Subscripts

0^+	gas-phase side of propellant surface
0^-	condensed-phase side of propellant surface
c	condensed phase
$c-g$	from condensed to gas phase
cond	condensation
eq	equilibrium condition
evap	evaporation
f	mass-averaged quantity in subsurface foam layer
g	gas phase
l	liquid phase
s	propellant surface or solid phase
v	vapor

nitramines (RDX, HMX, HNIW hexanitrohexaazaisowurtzitane also known as CL-20, HNF hydrazinium nitroformate), azides (GAP, BAMO, AMMO), nitrate esters (NG, NC, BTTN 1,2,4-butane triol trinitrate, TMETN metriol trinitrate, DEGDN diethylene glycol dinitrate), or nitrates (ADN, AN). Fig. 1 shows the molecular structures of the above propellant ingredients. Their material densities, heats of formation (ΔH°_f), and adiabatic flame temperatures (T_f) are given in Table 1 [3]. The material densities are typically in the range of 1.2–2.0 g/cm^3. The heat of formation varies widely and is instrumental in determining the flame temperature and the total energy released during combustion.

Given the wide variety of energetic materials and possible compositions, large test matrices for their detailed characterization are difficult, time consuming, and expensive to develop. Hence, new opportunities to advance the field of energetic materials increasingly rest on the predictive capability of combustion models. Accurate models can elucidate the interplay between the chemical and physical phenomena and the resulting mechanisms that produce the observed burning behavior and combustion characteristics as functions of pressure, initial temperature, external stimuli, and propellant chemical formulation. This will help us verify the proposed chemical pathways and identify the

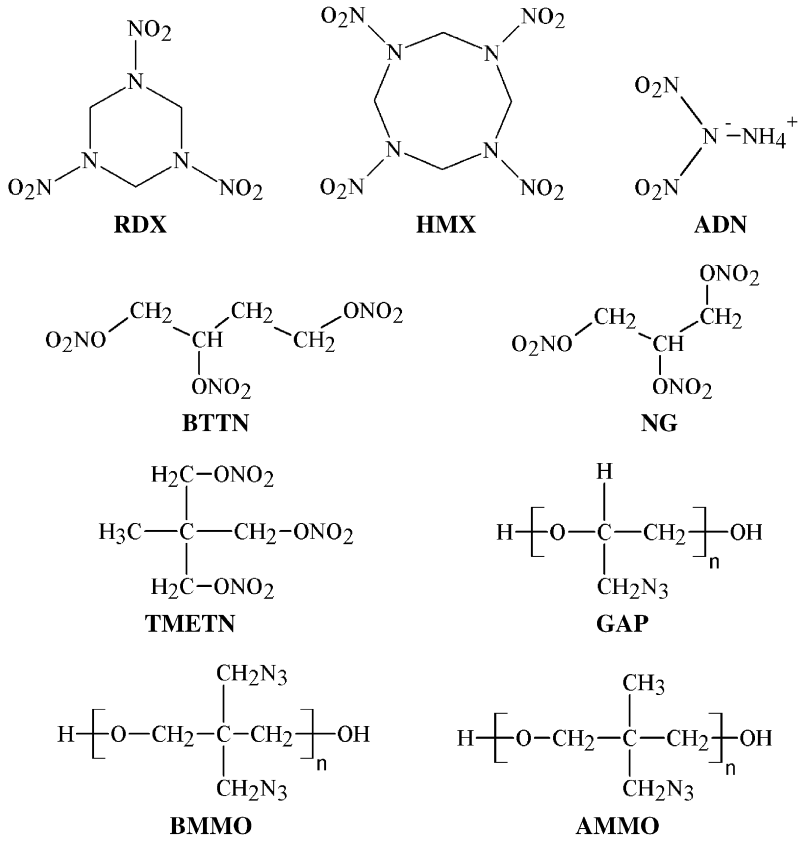

Fig. 1. Molecular structures of RDX, HMX, ADN, BTTN, NG, TMETN, GAP, BMMO, and AMMO.

chemical kinetics involved. Sensitivity analysis using established models allows a natural link between experimental and modeling efforts, and can be used to design experiments and to identify key reactions and species that require further theoretical study. The development of such models is a significant step towards more accurate and comprehensive predictions, and helps optimize chemical compositions to meet the required needs. Thus, the necessary level of insight can be attained and successfully embodied in the predictive models for effective propellant design, development, and testing activities.

Understanding the thermal decomposition of energetic materials and their ensuing combustion characteristics is one of the central objectives of the modeling efforts. The combustion characteristics of concern include pressure and temperature sensitivities of burning rate, propellant surface conditions, and spatial distributions of energy release, temperature, and species concentration. A well-rounded model should be able to predict all these properties in good agreement with experimental measurements. The current paper aims to provide a comprehensive review of recent advances in theoretical modeling and numerical simulation of solid-propellant ingredient combustion and ignition over a wide range of ambient conditions. The specific materials of concern include nitramines (RDX, HMX), azides (GAP), nitrate esters (NG, BTTN), ADN, and AP monopropellants, as well as homogeneous mixtures representing binary (RDX/GAP, HMX/GAP, and AP/HTPB) and ternary (RDX/GAP/BTTN) pseudo-propellants. Emphasis is placed on nitramines due to the substantial accomplishments in this area in the past decade. Only homogeneous-propellant compositions involving premixed flames are considered, a situation that holds true if there are no particles in the composition, or the particulate phase is on the order of 10 μm or less [4].

The paper is structured as follows. Section 2 summarizes the physiochemical mechanisms underlying the combustion process of solid-propellant ingredients, along with the challenges involved in the modeling issues. Section 3 gives a detailed theoretical formulation of the phenomenon. Sections 4 and 5

Table 1
Monopropellant ingredient properties (Ref. [3])

Ingredient	Density (g/cm^3)	ΔH_f° (kcal/mole)	T_f (K) (~68 atm)
Nitrates			
ADN	1.72	−35.8	2062
AN	1.73	−87.3	1247
Perchlorate			
AP	1.95	−70.7	1405
Nitramines			
HNIW	1.96	90.0	3571
HMX	1.90	18.1	3278
RDX	1.82	14.7	3286
HNF	1.86	−17.2	3090
Nitrate esters			
NG	1.60	−90.7	3287
TMETN	1.47	−106.0	2839
DEGDN	1.39	−103.5	2513
NC	1.65	−61.4	2425
BTTN	1.52	−92.97	3190
Azides			
BAMO	1.28	53.3[a]	1725
GAP	1.27	2.85[a]	1570
AMMO	1.26	4.32[a]	1536

[a]For polymers, the heat of formation is given in kcal/100 g.

present an overview of simplified models developed in the earlier stage. Section 6 deals with the state-of-the-art modeling approaches applied to both monopropellants and pseudo-propellants. Results from those modeling efforts are also summarized to provide direct insight into the phenomena of concern. Section 7 describes the ignition models based on global and detailed chemical kinetics. An overall summary is given in Section 8.

2. Physiochemical processes in homogeneous solid-propellant combustion

2.1. Combustion-wave structures

Combustion of a solid propellant involves an array of intricate physiochemical processes evolving from the various ingredients that constitute the propellant. Most of the individual ingredients in solid-propellant formulations burn as monopropellants [5]. To facilitate discussion, we first consider the example of self-deflagrating RDX monopropellant in a stagnant environment. The entire combustion-wave structure can generally be segmented into three regions: (1) solid phase, (2) subsurface two-phase, and (3) gas phase as shown schematically in Fig. 2 [6]. The underlying physical processes in each of these regimes are illustrated in Fig. 3. During burning, the propellant remains thermally stable in the solid phase until the temperature reaches the melting point at which thermodynamic phase transition occurs. Molecular degradation and evaporation then takes place in the liquid layer, generating bubbles and forming a subsurface two-phase region, also referred to as a foam layer. The ensuing products subsequently undergo a sequence of rapid decomposition in the near field immediately above the foam layer. For convenience, the propellant-burning surface ($x = 0$) is defined herein as an interface between the foam layer and the gas-phase region, at which rapid gasification or decomposition takes place. In the gas-phase region, the species emanating from the burning surface react with each other and/or decompose to form other species. A wide variety of oxidation reactions continue to occur and release an enormous amount of energy in the gas phase with the final temperature reaching the adiabatic flame temperature. The heat feedback from the exothermic reactions occurring in the gas phase along with the condensed-phase heat release sustains the combustion process.

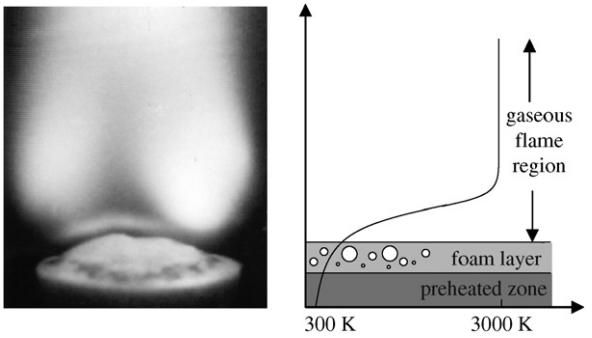

Fig. 2. Strand of RDX burning in a stagnant environment; self-sustained combustion (not to the scale) [6].

The specific processes in the condensed and gas phases depend on the particular ingredient under consideration. For example, in the case of HMX monopropellant, a polymorphic phase transition occurs from β-HMX to δ-HMX at about 460 K [7]. For AP, a similar transition from an orthorhombic to a cubic structure occurs at 513 K [8]. Owing to the low liquefaction temperature (478 K for RDX and 558 K for HMX), the solid-phase reactions are usually neglected in comparison to the much faster liquid- and gas-phase reactions. This situation holds true for most ingredients, except for AP

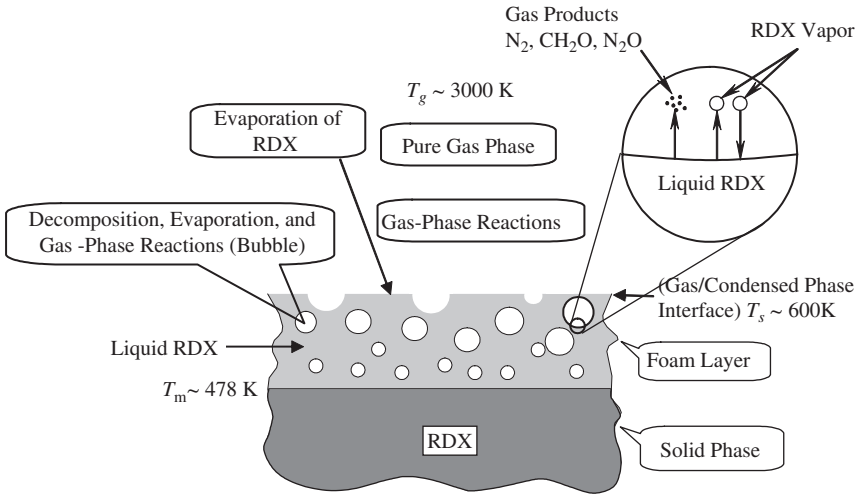

Fig. 3. Schematic illustration of combustion-wave structure of RDX monopropellant; self-sustained combustion (not to the scale).

(T_{melt}~725–825 K) [9] and ADN (T_{melt}~365–368 K) [10], which undergo significant exothermic reactions in the solid phase. For energetic polymers like GAP, the liquefaction (depolymerization) point is not well defined and a temperature corresponding to the onset of decomposition reactions needs to be judiciously selected for modeling purposes [11]. Both RDX and HMX monopropellant combustion exhibits a visible, definite foam layer at low and moderate pressures. The thickness of the foam layer and the gas-phase reaction zone vary with pressure. At 1 atm, the foam layer is ~70 and ~130 μm for HMX and RDX, respectively, and the gas phase reaches equilibrium within ~4 and ~1 mm from the burning surface [12,13]. At higher pressures (70–100 atm), the foam layer is less than 20 μm thick, and the equilibrium temperature is reached within ~100–200 μm from the surface for nitramine monopropellants.

2.2. Challenges involved in modeling solid-propellant combustion

In order to accurately model all the burning characteristics of concern for solid propellants, a detailed description of the gas-phase, condensed-phase, and surface mechanisms is essential. In the gas phase, a variety of chemical species undergo a gamut of chemical reactions coupled with the processes of molecular diffusion, convection, conduction, and radiation. In the condensed phase, decomposition reactions and/or evaporation occur in the foam layer, along with subsequent reactions in the embedded bubbles (see Fig. 3). Developing a theoretical model that faithfully describes such a complex reacting, multi-phase transport system with variable thermophysical properties is a great challenge.

Different opinions exist about the relative importance between the gas- and condensed-phase heat release in dictating the combustion characteristics of a solid propellant. A recent work [14] claims that condensed-phase reactions dominate the burning behaviors of many propellant ingredients, according to thermocouple measurements in the pressure range of 1–70 atm [15]. Such a statement, however, remains to be clarified. At a pressure above ~10 atm, the flame stands so close to the burning surface that the spatial resolution of thermocouple measurement becomes insufficient to accurately explore the detailed physiochemistry near the surface. For example, Zenin [15] reported a flame standoff distance of ~0.3 mm for HMX at 20 atm using thermocouples, whereas Parr and Hanson-Parr measured a value of ~0.12 mm at 12 atm using spectroscopic techniques [12]. Because a higher flame standoff distance implies a lower heat transfer from the flame zone to the condensed phase, the thermocouple measurements often underpredict, especially at high pressures, the role of gas-phase reactions in determining the propellant-burning rate. Thus, one must consider both the condensed and gas-phase processes in an integrated manner to provide a high-fidelity description of the combustion of propellant ingredients. At low pressures, the flame stands off relatively farther from the surface, and

the condensed-phase heat release may dominate the burning rate. At high pressures, however, the temperature gradient in the gas phase near the surface becomes much steeper, and the residence time in the condensed phase decreases considerably due to a thinner melt layer. As a consequence, the gas-phase heat release dominates the propellant combustion at high pressures.

It is formidable to obtain experimental data on the thermophysical properties of the foam layer or on the kinetics of reactions within the foam layer due to its exceedingly small dimension and short residence time. Furthermore, it is not possible to extract quantitative information about species concentrations in the condensed phase by means of spectroscopic diagnostics (e.g., IR and RAMAN derivative spectroscopies), especially for trace radicals. The reactions in the gas phase, however, are more amenable to diagnosis, either by experimental measurements or by *ab initio* calculations. Therefore, the extensive knowledge and experience established so far mainly focus on the gas phase, although a number of theoretical and experimental diagnostics have confirmed an active role of condensed-phase processes for many widely used propellants. Uncertainties as to the gas-phase processes currently center on the decomposition of large molecules and the rate coefficients of certain reactions in the desired ranges of pressure and temperature. There is a general lack of fundamental understanding of the condensed-phase processes. The knowledge of subsurface reactions is limited; not only in terms of pathways and rate coefficients, but also with respect to the very identities of both reactants and products involved in the condensed-phase reactions [16]. Thus, the challenges in establishing a faithful modeling approach lie in the exact determination of chemical species that emerge from the subsurface layer into the gas phase and the corresponding chemical pathways and reaction rates.

3. Theoretical formulation

The theoretical formulation of the various physiochemical processes in the combustion zone is summarized below. As a first approximation to the problem, a quasi one-dimensional model is established with the origin of the coordinate system fixed at the propellant surface ($x = 0$). The model consists of conservation equations for the solid-phase, subsurface two-phase, and gas-phase regions, along with appropriate boundary conditions.

3.1. Solid-phase region

Chemical reactions are generally ignored in the solid-phase region due to the low-temperature condition and short residence time [6,17]. Thus, only heat conduction governed by the following:

$$\rho_s c_s \frac{\partial T_s}{\partial t} + \rho_s u_s c_s \frac{\partial T_s}{\partial x} = \frac{\partial}{\partial x}\left(\lambda_s \frac{\partial T_s}{\partial x}\right) + \dot{Q}'''_{rad,s}, \qquad (1)$$

where ρ_s is the density, c_s the specific heat, λ_s the thermal conductivity, and u_s the recession rate for the solid state. In the case of pseudo-propellant mixtures, the thermophysical properties can be estimated based on the mass fractions of the constituent ingredients. By neglecting the effect of radiation, a closed form solution of Eq. (1) at steady state is available subject to appropriate boundary conditions and the propellant-burning rate.

3.2. Subsurface two-phase region

The liquid and gas bubbles underneath the propellant surface are treated together and referred to as the subsurface two-phase region or foam layer. The physiochemical processes in this region are extremely complex, involving an array of intricacies such as thermal decomposition, evaporation, bubble formation, gas-phase reactions in bubbles, and interfacial transport of mass and energy between the gas and condensed phases. Consequently, the subsurface layer is the least understood of the three regimes, and there have been significant variations in modeling this region. Taking full account of all the processes is not practical, and simplifications are made to render the analysis manageable. A two-phase fluid dynamic model based on a spatial averaging technique was employed by Liau and Yang [6,18] and Davidson and Beckstead [17] to formulate these complicated phenomena. The analysis is based on the integral form of conservation laws for control volumes occupied separately by the gas-bubbles and condensed phases, using a fractional-volume voidage (ϕ) defined as

$$A_g = \phi A, \qquad (2)$$

where A is the cross-sectional area of the propellant sample, and A_g the fractional area consisting of gas bubbles. The assumption is valid so long as numerous gas bubbles are present and distributed randomly. The mass diffusion velocities in the two-phase region are relatively small compared to their

convective counterparts, and thus are ignored to simplify the analysis. The conservation equations for both the liquid phase and gas bubbles are combined into the following:

Mass:

$$\frac{\partial[(1-\phi_f)\rho_c+\phi_f\rho_g]}{\partial t}+\frac{\partial}{\partial x}[(1-\phi_f)\rho_c u_c+\phi_f\rho_g u_g]=0. \quad (3)$$

Liquid species concentration:

$$\frac{\partial[(1-\phi_f)\rho_c Y_{c_i}]}{\partial t}+\frac{\partial}{\partial x}[(1-\phi_f)\rho_c u_c Y_{c_i}]=\dot{w}_{c_i} \quad (i=1,2,\ldots,N_c). \quad (4)$$

Gaseous species concentration:

$$\frac{\partial(\phi_f\rho_g Y_{g_i})}{\partial t}+\frac{\partial(\phi_f\rho_g u_g Y_{g_i})}{\partial x}=\dot{w}_{\dot{g}_i} \quad (i=1,2,\ldots,N_g). \quad (5)$$

Energy:

$$\rho_f c_f\frac{\partial T_f}{\partial t}-\frac{\partial p}{\partial t}+\rho_f u_f c_f\frac{\partial T_f}{\partial x}=\frac{\partial}{\partial x}\left(\lambda_f\frac{\partial T_f}{\partial x}\right)-\sum_{j=1}^{N_g}\dot{w}_{g_j}h_{g_j}-\sum_{j=1}^{N_c}\dot{w}_{c_j}h_{c_j}+\sum_{j=1}^{N_g}h_{g_j}Y_{g_j}\dot{w}_{c-g}-\sum_{j=1}^{N_c}h_{c_j}Y_{c_j}\dot{w}_{c-g}+\dot{Q}'''_{rad,c}, \quad (6)$$

where the subscript f denotes the mass-averaged quantity in the foam layer. The source terms, $\dot{w}_{c_i}$ and $\dot{w}_{g_i}$ represent the mass production rates of the ith species in the liquid phase and the gas bubbles, respectively, and $\dot{w}_{c-g}$ the rate of mass conversion from liquid to gas. The properties are mass-averaged as follows:

$$\rho_f c_f=(1-\phi_f)\rho_c c_c+\phi_f\rho_g c_g, \quad (7)$$

$$\rho_f u_f c_f\equiv(1-\phi_f)\rho_c u_c c_c+\phi_f\rho_g u_g c_g, \quad (8)$$

$$\lambda_f=\frac{[(1-\phi_f)\rho_c u_c\lambda_c+\phi_f\rho_g u_g\lambda_g]}{[(1-\phi_f)\rho_c u_c+\phi_f\rho_g u_g]}, \quad (9)$$

where

$$c_c=\sum_{i=1}^{N_c}c_{c_i}Y_{c_i},\quad c_g=\sum_{i=1}^{N_g}c_{g_i}Y_{g_i},$$

$$\lambda_c=\sum_{i=1}^{N_c}\lambda_{c_i}Y_{c_i},\quad\text{and}\quad\lambda_g=\sum_{i=1}^{N_g}\lambda_{g_i}Y_{g_i}. \quad (10a–d)$$

The mass and energy production terms depend on the specific chemical reaction mechanisms in the subsurface foam layer. In addition to thermal decomposition and subsequent reactions, thermodynamic phase transition from liquid to vapor is considered to provide a complete description of the mass conversion process. For instance, in the case of RDX monopropellant combustion [6], the phase transition is represented by (R.1).

$$\mathrm{RDX}_{(l)}\Leftrightarrow\mathrm{RDX}_{(g)}. \quad (R.1)$$

The process consists of both evaporation and condensation and can be modeled using gas-kinetic theory. If the thermodynamic phase equilibrium exists, then the evaporation process proceeds at the same rate as the condensation process. At nonequilibrium conditions, the net evaporation rate is taken to be the difference between the evaporation and condensation rates [18], and can be expressed as

$$\dot{m}''_{net}=s\frac{1}{4}\sqrt{\frac{8R_uT}{\pi W_{RDX}}}\frac{pW_{RDX}}{R_uT}\left(\frac{p_{v,eq}}{p}-X_{RDX}\right), \quad (11)$$

where s is the sticking coefficient. Thus, the specific mass conversion rate due to evaporation becomes

$$\dot{w}_{evap}=A_{sp}\dot{m}''_{net}. \quad (12)$$

The specific surface area, A_{sp}, is a function of void fraction and number density of bubbles, and is derived as follows:

$$A_{sp}=(36\pi n)^{1/3}\phi_f^{2/3},\quad \phi<1/2,$$
$$A_{sp}=(36\pi n)^{1/3}(1-\phi_f)^{2/3},\quad \phi>1/2, \quad (13)$$

where n is the number density of gas bubbles to be determined empirically [18]. A recent model that treats the multi-phase effects in the subsurface region also includes a description of the surface tension of the bubbles in the liquid layer [19].

3.3. Gas-phase region

The analysis for the gas phase is based on the mass, energy, and species transport for a multi-component chemically reacting system, and accommodates finite-rate chemical kinetics and variable thermophysical properties. The so-called gas phase may sometimes contain dispersed condensed-phase species. Consequently, a multi-phase treatment similar to that described for the subsurface

two-phase region is employed [20]. A pure single-phase treatment can be applied by taking $\phi_g = 1$ [6,7,17]. Unlike the situation in the subsurface two-phase layer, the cross-sectional area A in the gas phase is not always constant, because of the effect of flame expansion. By ignoring body force, viscous dissipation, and kinetic energy, the isobaric conservation equations for the gas phase can be written as follows:

Mass:

$$\frac{\partial[(1-\phi_g)A\rho_c + \phi_g A\rho_g]}{\partial t} + \frac{\partial}{\partial x}[(1-\phi_g)A\rho_c u_c + \phi_g A\rho_g u_g] = 0. \quad (14)$$

Species concentration:

$$\frac{\partial[(1-\phi_g)A\rho_c Y_{c_i}]}{\partial t} + \frac{\partial}{\partial x}[(1-\phi_g)A\rho_c u_c Y_{c_i}] = A\dot{w}_{c_i} \quad (i = 1, 2, \ldots, N_c). \quad (15)$$

Gaseous species concentration:

$$\phi_g A\rho_g \frac{\partial Y_{g_i}}{\partial t} + \phi_g A\rho_g u_g \frac{\partial Y_{g_i}}{\partial x} + \frac{\partial(\phi_g A\rho_g V_{gi} Y_{g_i})}{\partial x} = A\dot{w}_{g_i} - Y_{gi} A\dot{w}_{c-g} \quad (i = 1, 2, \ldots, N_g). \quad (16)$$

Energy:

$$\rho c_p A\frac{\partial T_g}{\partial t} - \frac{\partial(pA)}{\partial t} + \rho u c_p A\frac{\partial T_g}{\partial x} = \frac{\partial}{\partial x}\left(\lambda A\frac{\partial T_g}{\partial x}\right) - \phi_g A\sum_{j=1}^{N_g}\rho_g Y_{g_i} V_{g_i} c_{p_{g_i}}\frac{\partial T_g}{\partial x} - A\sum_{j=1}^{N_g}\dot{w}_{g_j}h_{g_j} - A\sum_{j=1}^{N_c}\dot{w}_{c_j}h_{c_j} + A\sum_{j=1}^{N_g}h_{g_j}Y_{g_j}\dot{w}_{c-g} - A\sum_{j=1}^{N_c}h_{c_j}Y_{c_j}\dot{w}_{c-g} + A\dot{Q}'''_{rad,g}. \quad (17)$$

The thermophysical properties used in Eq. (17) are mass-averaged as follows:

$$\rho c_p = (1-\phi_g)\rho_c c_c + \phi_g\rho_g c_g, \quad (18)$$

$$\rho u c_p = (1-\phi_g)\rho_c u_c c_c + \phi_g\rho_g u_g c_g, \quad (19)$$

$$\lambda_g = \frac{[(1-\phi_g)\rho_c u_c\lambda_c + \phi_g\rho_g u_g\lambda_g]}{[(1-\phi_g)\rho_c u_c + \phi_g\rho_g u_g]}. \quad (20)$$

The enthalpy of gaseous or condensed species i is defined as

$$h_{g_i} = \int_{T_{ref}}^{T} c_{g_i}\,\mathrm{d}T + h^{\circ}_{f_{gi}}. \quad (21)$$

The mass diffusion velocity V_i consists of contributions from both concentration (i.e., Fick's law) and temperature (i.e., the Soret effect) gradients:

$$V_i = -D_i\frac{1}{X_i}\frac{\partial X_i}{\partial x} + D_i\frac{D_{T_i}}{X_i}\frac{1}{T}\frac{\partial T_g}{\partial x}. \quad (22)$$

Finally, the equation of state for a multi-component system is used to close the formulation

$$p = \rho_g R_u T_g\sum_{i=1}^{N_g}\frac{Y_{g_i}}{W_{g_i}}. \quad (23)$$

3.4. Boundary conditions

The physical processes in the gas phase and subsurface foam layer must be matched at the propellant surface to provide the boundary conditions for each region. This procedure requires balances of mass and energy, and eventually determines propellant surface conditions and burning rate. With the neglect of mass diffusion in the condensed phase, the conservation laws at the propellant surface can be written as follows:

Mass:

$$[(1-\phi_f)\rho_c u_c + \phi_f\rho_g u_g]_{0^-} = [(1-\phi_g)\rho_c u_c + \phi_g\rho_g u_g]_{0^+}. \quad (24)$$

Species:

$$[(1-\phi_f)\rho_c u_c Y_{c_i} + \phi_f\rho_g u_g Y_{g_i}]_{0^-} = (1-\phi_g)\rho_c u_c Y_{c_i} + \phi_g\rho_g(u_g + V_{g_i})Y_{g_i}]_{0^+}. \quad (25)$$

Energy:

$$\left[\lambda_f\frac{\mathrm{d}T_f}{\mathrm{d}x} + (1-\phi_f)\rho_c u_c Y_{i,c}h_{i,l\to g}\right]_{0^-} = \left[\lambda_g\frac{\mathrm{d}T_g}{\mathrm{d}x}\right]_{0^+} + \alpha_{sur}\dot{Q}''_{laser}, \quad (26)$$

where subscripts 0^+ and 0^- represent conditions at the interface on the gas-phase and subsurface sides, respectively, and α_{sur} is the fraction of laser heat flux absorbed by the propellant surface. The temperature is identical on both sides of the interface, but the void fraction and species mass

fractions may be different. Eq. (24) is essentially the summation of mass fluxes of all species governed by Eq. (25), and thus cannot be used independently to determine the propellant surface conditions and eigenvalue of the problem (i.e., the burning rate). An additional condition is required in the form of thermodynamic phase transition from liquid to vapor at the propellant surface ($x = 0$), giving [6,18,20–23],

$$\left[(1-\phi_f)\rho_c u_c\right]_{0^-} = \dot{m}''_{net}, \tag{27}$$

where $\dot{m}''_{net}$ is given by Eq. (11). It has been shown that $T_g = T_c$ and $\rho_c u_c = \rho_g u_g$ are reasonable assumptions in the subsurface two-phase region, rendering Eq. (24) trivial [6]. These simplified assumptions coupled with Eqs. (25)–(27) are sufficient to solve the set of unknowns (u, T, Y_i, ϕ) at the propellant surface.

The boundary conditions at the interface between the solid phase and foam layer (i.e., the melt front) are

$$T_c = T_f = T_{melt} \quad \text{and} \quad \phi = 0 \quad \text{at} \quad x = x_{melt}, \tag{28}$$

$$\left[\lambda_s \frac{\mathrm{d}T_s}{\mathrm{d}x} + \rho_s u_s Y_i h_{i_{s\to l}}\right]_{x^-_{melt}} = \left[\lambda_f \frac{\mathrm{d}T_f}{\mathrm{d}x}\right]_{x^+_{melt}}. \tag{29}$$

The far-field conditions for the gas phase require the gradients of flow properties to be zero at $x = \infty$

$$\frac{\partial \rho}{\partial x} = \frac{\partial u}{\partial x} = \frac{\partial Y_i}{\partial x} = \frac{\partial T}{\partial x} = 0 \quad \text{at} \quad x = \infty. \tag{30}$$

The condition at the cold boundary for the solid phase ($x = -\infty$) is

$$T_c = T_o \quad \text{as} \quad x \to -\infty, \tag{31}$$

where T_o is the pre-conditioned temperature of the propellant. The initial mass fractions of the propellant ingredients are also provided as input parameters.

4. Classification of solid-propellant combustion models

Existing models of solid-propellant combustion can be broadly classified into three general categories: (1) simple models that do not account for chemical kinetics and typically solve only the mass and energy equations in the condensed and gas phases; (2) global-kinetics models based on simplified chemical reaction mechanisms in either, or in both, the gas and condensed phases; and (3) detailed models with elementary kinetics mechanisms in the gas phase, and thermal decomposition and subsequent reactions in the condensed phase. In addition, various ignition models have also been developed. Most of the existing analyses use global reactions to simulate ignition, but some recent efforts have modeled the entire process of ignition with detailed kinetics.

5. Simple combustion models

5.1. Mathematical formulation

The motivation for establishing simple models for solid-propellant combustion stems primarily from the universal behavior of the observed burning rate as a function of pressure and initial temperature. Simplified modeling is very useful for treating multidimensional transient problems. In some cases, the models can provide an insight where the elementary reaction mechanisms make it difficult to perform adequate sensitivity analysis. The combustion process is usually described by the mass and energy conservation equations for the condensed-(generally assumed to be solid) and the gas-phase regions with their mutual interplay at the phase boundary. The species transport equations are not considered and the chemical reactions are treated in a lumped manner to mimic the heat release. Surface gasification is modeled as either evaporation or pyrolysis. Thermophysical properties are generally assumed to be constant for the sake of simplicity, and radiation is neglected. A unity Lewis-number assumption is employed in the gas phase.

In principle, the burning rate can be obtained by solving the conservation equations in the solid and gas phases separately, and then matching the solutions at the interface in a manner consistent with the assumed surface mechanism. Reaction rates expressed in the Arrhenius form render the conservation equations nonlinear, placing an exact analytical solution beyond reach. Several approximations have thus been made in order to obtain analytic expressions for the burning-rate as a function of pressure [24]. In the condensed phase, with assumption of constant thermophysical properties and a steady-state condition, the mass and energy conservation equations (3) and (6), respectively, reduce to

$$\dot{m}'' = \rho_c r_b, \tag{32}$$

$$\lambda_c \frac{d^2T}{dx^2} - \rho_c r_b c_c \frac{dT}{dx} + Q_c \dot{w}_c(x) = 0, \tag{33}$$

subject to the boundary conditions

$$T = T_o \quad \text{at} \quad x = -\infty,$$
$$T = T_s \quad \text{at} \quad x = 0,$$

where λ_c is the thermal conductivity, c_c the specific heat, and Q_c the heat of reaction per unit mass in the condensed phase. If no chemical reaction is assumed ($\dot{w}_c(x) = 0$), then Eq. (33) can be integrated to obtain the temperature profile in the condensed phase given by

$$T(x) = T_o + (T_s - T_o) \exp\left[\frac{r_b}{\alpha_c} x\right], \tag{34}$$

where $\alpha_c (\equiv \lambda_c/\rho_c c_c)$ is the thermal diffusivity. The ratio α_c/r_b represents the thermal penetration depth (i.e. the thickness of the preheat zone) in the condensed phase, and is on the order of 100 μm at typical rocket motor operating pressures. The heat feedback from the burning surface to the condensed phase can be obtained by integrating Eq. (33) from 0 to $-\infty$

$$\lambda_c \left[\frac{dT}{dx}\right]_{x=-0} = \rho_c r_b c_c (T_s - T_o) + Q_c \int_0^{-\infty} \dot{w}_c(x)\, dx. \tag{35}$$

The last term in the above equation represents the net heat release in the condensed phase. Most of the simple models that consider condensed-phase reactions employ the assumption of high activation energy to model the heat release. This allows an approximate solution for the condensed-phase mass flux to be obtained from Eq. (33). With the use of a zeroth-order, high activation-energy decomposition reaction ($\dot{w}_c = \rho_c A_c \exp(-E_c/R_u T)$) in the condensed phase, Merzhanov and Dubovitskii [25] arrived at an Arrhenius-like expression given by

$$\dot{m}''^2 = \frac{A_c R_u T_s^2 \lambda_c \rho_c \exp(-E_c/R_u T_s)}{E_c[c_c(T_s - T_o) - Q_c/2]}, \tag{36}$$

where A_c is the frequency factor and E_c the activation energy of the condensed-phase reactions. The equation was later obtained by Lengellé using an approach based on activation energy asymptotics (AEA) [26]. The assumption of high activation-energy implies that the condensed-phase reactions occur in a very thin region (i.e. the reactive-diffusive zone on the order of a few microns) underneath the burning surface [25,26]. The surface temperature T_s is not known and an additional equation in the form of surface energy balance is essential.

A simplified form of Eq. (36) represented by an Arrhenius-like pyrolysis law is often employed [27] as follows:

$$\dot{m}'' = m_o \exp(-E_s/R_u T_s), \tag{37}$$

where E_s is the surface activation energy, and m_o a constant. In most cases, E_s assumes a value, which is characteristic of the family of chemicals that the propellant belongs to, but m_o is typically an empirical parameter used for fitting experimental data [24]. While Eq. (37) provides an effective correlation of propellant burning rate and surface temperature, Eq. (36) is a more complete representation of the physiochemical processes that occur in the condensed phase, and thus can be applied to a broader range of physical conditions. The situation is especially true for problems involving transient and erosive burning, where Eq. (36) offers more accurate predictions [28].

Mitani and Williams [29] developed an expression similar to Eq. (36) for nitramine deflagration given by

$$\dot{m}''^2 = \frac{A_c R_u T_s^2 \lambda_c \rho_c \exp(-E_c/R_u T_s)}{E_c[Q_c(1-G) + (c_c(T_s - T_o) - Q_c)\ln(1/G)]}, \tag{38}$$

where G is the mass fraction of the propellant entering the gas phase. Eq. (36) assumes complete propellant decomposition within the condensed phase, whereas Eq. (38) assumes that a fraction of undecomposed propellant gasifies at the burning surface.

In the gas phase, with the assumption of constant thermophysical properties and a steady-state condition, the mass and energy conservation equations (14) and (17), respectively, reduce to

$$\dot{m}'' = \rho_c r_b = \rho_g u_g, \tag{39}$$

$$\lambda_g \frac{d^2T}{dx^2} - \rho_c r_b c_{pg} \frac{dT}{dx} + Q_g \dot{w}_g(x) = 0, \tag{40}$$

subject to the boundary conditions

$$T = T_f \quad \text{or} \quad \frac{dT}{dx} = 0 \quad \text{at} \quad x = \infty,$$
$$T = T_s \quad \text{at} \quad x = 0,$$

where λ_g is the thermal conductivity, c_{pg} the specific heat, and Q_g the heat of reaction per unit mass in the gas phase. Integration of Eq. (40) gives the conductive feedback flux from the gas phase at the

propellant surface

$$\lambda_g \left[\frac{dT}{dx}\right]_{x=+0} = Q_g \int_0^\infty \exp\left(-\frac{\rho_c r_b c_{pg}}{\lambda_g} x\right) \dot{w}_g(x)\, dx. \tag{41}$$

Several different approaches have been employed to model the heat-release distribution in the gas phase. A general description provided by Kubota [1] is represented as

$$\begin{aligned} &\dot{w}_g Q_g = 0 \quad \text{at} \quad 0 < x < x_i, \\ &\dot{w}_g Q_g > 0 \quad \text{at} \quad x_i < x < x_f, \\ &\dot{w}_g Q_g = 0 \quad \text{at} \quad x > x_f. \end{aligned} \tag{42}$$

One of the limiting cases given by $x_i = 0$ implies that the reaction commences at the burning surface, corresponding to a low activation-energy treatment. Another limiting case with $x_i = x_f$ implies a flame-sheet assumption, corresponding to a high activation-energy treatment. Williams assumed a high activation-energy for gas-phase reactions and obtained an expression for the mass flux by means of asymptotic analysis [30]

$$\dot{m}''^2 = \frac{2\lambda_g B_g R_u^2 p^n c_{pg} T_f^4 \exp(-E_g/R_u T_f)}{E_g^2 Q_g^2}, \quad \left(\frac{E_g}{R_u T_f} \gg 1\right), \tag{43}$$

where B_g is the frequency factor, n is the overall order of the gas-phase reaction, and E_g the activation energy in the gas phase. The equation was earlier obtained by Denison and Baum [31] in a simplified model of unstable solid-propellant combustion. Eq. (43) contains several empirical parameters and is not constrained enough to capture the underlying physiochemical processes. The model does not account for the condensed-phase decomposition explicitly. The effect of the heat released in the condensed phase is included in the overall energy balance to determine the final flame temperature, T_f. The model was further improved by Mitani and Williams [29] to explicitly accommodate partial decomposition of the propellant in the condensed phase. The modified equation takes the form

$$\dot{m}''^2 = \frac{2\lambda_g B_g R_u^2 p^n c_{pg} T_f^4 \exp(-E_g/R_u T_f)}{G^2 E_g^2 Q_g^2}, \quad \left(\frac{E_g}{R_u T_f} \gg 1\right). \tag{44}$$

In general, the burning rate is obtained through the energy balance at the burning surface as

$$\lambda_g \left[\frac{dT}{dx}\right]_{x=+0} = \rho_c r_b c_c (T_s - T_o) + \dot{m}'' Y_s H_v - \dot{m}''(1 - Y_s) Q_c, \tag{45}$$

where Y_s is the mass fraction of the propellant undergoing evaporation at the burning surface. Eq. (45) contains three unknowns: $\dot{m}''$, T_s, and Y_s. Thus, two more equations are necessary to obtain a solution. The first results from the assumed surface mechanism. There are two schools of thought in this regard, one assuming surface pyrolysis and the other surface evaporation [24]. For such mono-propellants as nitrate esters, only surface pyrolysis is considered important with $Y_s = 0$ [32]. Thus the only two unknowns are $\dot{m}$ and T_s, and the additional equation is either in the form of Eq. (36) or Eq. (37). For such monopropellants as nitramines, evaporation prevails at the burning surface and an additional equation in terms of the Clasius–Clapeyron relation is employed to characterize the thermodynamic phase transition given by

$$p_v = p_o \exp(-H_v/R_u T_s), \tag{46}$$

where H_v is the heat of vaporization and p_o a constant. The vapor pressure p_v is a function of Y_s. In the case of evaporative surface mechanism, the third equation is generally obtained from the unity Lewis number assumption by relating T_s and Y_s. The appropriate linear combination of the species and energy equation provides,

$$Y_s = c_{pg} \frac{(T_f - T_s)}{Q_g}. \tag{47}$$

Several different analyses were established to determine the propellant-burning rate, depending on the various assumptions employed to treat the condensed- and gas-phase processes as well as the surface mechanism. One of the earliest models for mono- and composite-propellant combustion was the Beckstead–Derr–Price (BDP) model [27,33]. The monopropellant combustion submodel employed consists essentially of three coupled equations as follows:

$$\dot{m}'' = A \exp(-E_s/R_u T_s), \tag{48a}$$

$$T_s = T_o - \frac{Q_s}{c_{pg}} + \frac{Q_g}{c_{pg}} \exp\left(\frac{-c_{pg}\dot{m}''}{\lambda_g} x^*\right) \quad \text{with} \quad Q_g = c_{pg}(T_f - T_o) - Q_s, \tag{48b}$$

$$x^* = \frac{\dot{m}''}{kp^{\delta}}, \tag{48c}$$

where Q_s is the energy released at the burning surface, x^* the flame standoff distance, k the gas-phase rate constant in an Arrhenius form based on the flame temperature, and δ the reaction order. The above equations are derived based respectively on the surface pyrolysis mechanism, the energy balance at the burning surface, and the flame-sheet assumption for the gas phase. There is no condensed-phase treatment. For composite propellants, the BDP modeling approach is similar to the one described by Eq. (48), except that multiple flames are taken into account, as summarized in Table 2. The flame-sheet approach used in the BDP model [27,33] in essence follows the assumption of high activation energy in the gas phase.

Mitani and Williams [29] in their nitramine-deflagration model, considered exothermic decomposition in the condensed phase, equilibrium evaporation, and an exothermic gas-phase reaction. The burning rate was obtained iteratively by enforcing the energy balance and phase equilibrium at the burning surface along with the assumption of a unity Lewis number. In contrast with the Williams model [30], Ward et al. [34] assumed a vanishingly low activation energy for the gas phase, and employed a high activation energy approach (AEA) similar to Lengellé's model [26] for the condensed phase.

5.2. Representative models

Beckstead and McCarty [35] summarized the simplified combustion models for nitramine monopropellants published prior to 1975. Gusachenko and Zarko [36] reviewed solid-propellant modeling for homogeneous materials, with specific applications to Russian powder N, AP, and nitramines. Most of the models listed are based on some form of the energy equation assuming heat release in both the gas and condensed phases. The thermophysical properties are generally assumed constant. The species transport equations are generally not taken into account. The models were able to match the experimentally measured pressure sensitivity of the burning rate with reasonable accuracy in spite of the diverse physical assumptions. Optimization of empirical parameters is often required to ensure good agreement with experimental data. Some representative simple models and their prominent features are summarized in Table 2.

6. Combustion models based on global kinetics

Models of this type treat reduced chemical kinetics and solve both the energy and species transport equations. Unlike the simple models discussed in the preceding section, analytical expressions for the pressure and temperature sensitivities of burning rate cannot be derived. Global kinetics is immensely useful for multi-dimensional modeling, where the use of detailed mechanisms is not viable due to numerical stiffness problems attributed to the wide variety of time and length scales involved and limited computing sources.

Price and coworkers applied a modified BDP model to HMX considering two competing reactions in the condensed phase [50]. To predict the observed temperature sensitivity of HMX, two reactions were considered, one with exothermic decomposition (R.2) producing CH_2O and the other with endothermic decomposition (R.3) producing HCN. The latter had a greater role in dictating the combustion behavior [51]

$$HMX_{(c)} \rightarrow 4CH_2O + 4N_2O, \tag{R.2}$$

$$HMX_{(c)} \rightarrow 4HCN + 4NO_2 + 2H_2. \tag{R.3}$$

The model was further extended to treat transient phenomena such as ignition [52] and deflagration to detonation transition (DDT) [53]. Ben-Reuven et al. [54,55] included an in-depth condensed-phase reaction zone in their modeling of RDX and HMX combustion by considering a single first-order decomposition reaction (R.4). The gaseous species thus formed were assumed to be dissolved in the liquid, and bubble formation was neglected. Surface evaporation was calculated using the Clasius–Clapeyron expression by assuming vapor–liquid equilibrium. In the gas phase, in addition to (R.4), a secondary global reaction (R.5) between the decomposition products of (R.4) was considered. The energy and species conservation equations were numerically integrated to a converged steady-state solution. The calculations proceed from the surface until the entire RDX vapor decomposes, after which the remaining portion of the flame was assumed to have a negligible effect on the burning-rate characteristics. This results in a low-temperature inner flame (i.e. the primary flame, ~1100 K) that controls the burning rate. The model also provides the

Table 2
Representative simple models of solid-propellant combustion, 1970–2006

Ingredients	Researchers	Major assumptions and results
AP-based composite propellant	Beckstead et al. (1970) [27] (BDP model)	1. Three separate flame zones were considered, (a) a primary flame consisting of the decomposition products of oxidizer and the binder; (b) a premixed oxidizer flame; (c) a final diffusion flame consisting of the products from the other two flames 2. A flame-sheet assumption was used for the gas phase, and surface decomposition was represented by a simple Arrhenius expression 3. Calculated burning rate, surface temperature and temperature sensitivity were in good agreement with experimental data
AP	Manelis and Strunin (1971) [37]	1. The controlling mechanism for the burning rate was based on the condensed-phase decomposition by an equilibrium proton transfer to form perchloric acid and ammonia, and their ensuing sublimation 2. Results explain the peculiar burning-rate characteristics as a function of pressure, showing an initial rise with pressure, followed by a drop, and then a subsequent rise at higher pressures 3. The burning rate behavior was related to the change of equilibrium concentration of perchloric acid ($HClO_4$) with pressure, limiting the decomposition reactions
AP, HMX	Beckstead et al. (1971) [33]	1. The BDP model (1970) for composite propellants was modified to study AP and HMX monopropellants 2. For AP, 75% of the energy was assumed to be released as a surface reaction 3. The calculated pressure and temperature sensitivities of the burning rate showed good agreement with experimental data. The flame stand-off distance was also estimated 4. The calculated surface temperatures for HMX was erroneously high (1093 K at 13.6 atm) due to the high exothermic heat release assumed at the surface
AP	Guirao and William (1971) [38]	1. A one-step, second-order gas-phase reaction, deduced from a 10-step gas-phase mechanism, was assumed 2. A unity Lewis number was employed in the gas phase 3. The calculations suggested that 70% of AP decomposes at the surface by condensed-phase reactions and the remaining 30% vaporizes into $NH_{3(g)}$ and $HClO_{4(g)}$ 4. Calculated burning rate and pressure deflagration limit (20 atm) are in good agreement with experimental data
General	Ibiricu and Williams (1975) [39]	1. Both the condensed- and gas-phase analyses were based on the high activation-energy assumption 2. The effect of radiative heat transfer was considered
AP	Sohn (1975) [40]	1. The burning rate and pressure deflagration limit were predicted by considering the microstructure of the burning surface 2. The gas-phase chemical kinetics were represented by an overall second-order reaction 3. The same reaction mechanisms prevailed during deflagration and near the pressure limit. Extinction is attributed to the heat loss rather than the change in the reaction mechanism
HMX	Beckstead and McCarty (1976) [35]	1. The status of monopropellant combustion modeling prior to 1975 was summarized 2. Optimization of model parameters was achieved by comparison with experimental data 3. The pressure and temperature sensitivities of burning rate were obtained
AP	Strunin et al. (1977) [41]	1. A single-step, first-order reaction was considered in both the condensed and gas phases, along with the evaporation in the condensed phase 2. The pressure and temperature sensitivities of the burning rate were calculated for three different cases by including the condensed- or gas-phase reactions, or both 3. Agreement between the predictions and experimental data were not very good

Table 2 (*continued*)

Ingredients	Researchers	Major assumptions and results
AP	Price et al. (1978) [8]	1. Variable specific heats and thermal conductivity were taken into account, along with parallel reactions 2. The pressure and temperature sensitivities of burning rate, surface temperature, and flame standoff distance were predicted 3. Results were compared with BDP model [33], Manelis and Strunin [37], and Guirao and William [38]
DB (NC/NG)	Beckstead (1980) [42]	1. BDP model (1970) was modified and applied to DB propellants 2. Burning rate was obtained as a function of pressure, initial temperature and binder energy 3. Good agreement was achieved with experimental data
General	Miller and Coffee (1983) [43]	1. Five different sets of propellant data were developed spanning a wide range of kinetics values. Pressure and temperature dependence of burning rate was compared with experimental results 2. Weakness in the basic model idealization was identified
General	Miller and Coffee (1983) [44]	1. The numerical reliability of several models was identified by direct comparison of results with accurate numerical integrations of the conservation equations 2. Four different sets of propellant data spanning a wide range of kinetics parameters were utilized. None of the approximations proved accurate for all the data sets, but some models were quite accurate in certain limiting cases 3. It was concluded that a simple 1-D model cannot correctly predict all combustion characteristics
HMX	Mitani and Williams (1986) [29]	1. Exothermic reactions in the condensed and gas phases, along with equilibrium vaporization, were considered 2. The condensed phase analysis was similar to Guirao and Williams' approach (1971) and the gas-phase model employed the AEA method [30] 3. A lower flame temperature of 1330 K was used 4. Results indicated that 20–40% of HMX decomposed in the condensed phase depending on the pressure 5. Reasonable predictions for the pressure and temperature sensitivities of burning rate were made
AN, AP, HMX, DB (NG/NC)	Beckstead (1989) [45]	1. The basic BDP model (1971) was applied for AP, AN, and HMX, but slightly modified for double-base propellant 2. The dark-zone temperature for DB was chosen to be the flame temperature as the primary flame controls the burning rate 3. The model for HMX considered two major competing reactions in the initial decomposition, a low-temperature reaction dominant at low pressures and a high-temperature reaction at high pressures
RDX, HMX	Li et al. (1990) [46]	1. Mitani and Williams' model (1986) [29] was extended to account for the presence of bubbles and droplets in a two-phase layer near the propellant surface 2. An inner (primary) flame and a dark zone were assumed 3. Evaporation was the dominant surface process for RDX, and to a lesser extent for HMX 4. Good agreement with the measured pressure and temperature sensitivities of burning rate was achieved through reasonable approximations concerning overall kinetic parameters
HMX	Ward et al. (1998) [34] (WSB Model)	1. A zeroth order, high activation-energy thermal decomposition reaction was considered in the condensed phase, along with a bimolecular reaction in the gas phase with vanishingly small activation energy 2. A unity Lewis number was assumed in the gas phase 3. Predicted pressure sensitivity of burning rate, surface temperature, spatial distribution of temperature, and flame standoff distance showed good agreement with experimental data

Table 2 (*continued*)

Ingredients	Researchers	Major assumptions and results
		4. The calculated HMX temperature sensitivity matches closely the experimental data even at lower pressures
HNF	Louwers et al. (1999) [47]	1. The condensed phase was treated with high activation-energy asymptotics 2. The gas phase was treated with two limiting cases: the classical high activation-energy approximation, and vanishingly low activation-energy approximation similar to the WSB model [34]. The calculations using the latter approximation shows better agreement with the experimental data for mass burning rate, temperature sensitivity, surface temperature, and flame standoff distance
DB (NG/NC)	Brewster et al. (2000) [48]	1. The WSB model [34] for HMX was extended to DB propellants 2. The effect of radiant heat flux was considered 3. Predictions were made for steady-state burning-rate sensitivity parameters, temperature profile, and oscillatory combustion response
HMX	Kuznetsov and Stewart (2005) [49]	1. Variable properties and thermal expansion were included in the condensed-phase formulation 2. A zeroth order, high activation-energy thermal decomposition reaction was considered in the condensed phase 3. Numerical results indicate that for the gas-phase reaction the low activation-energy approximation gives a better agreement with the experimental data than the high activation-energy approximation 4. Thermal expansion tends to decrease the burning rate and the flame stand-off distance
General	Gusachenko and Zarko (2005) [14]	1. Existing combustion models were reviewed to investigate the role of condensed-phase processes in dictating the mass burning rate 2. It was concluded that the condensed-phase reactions play a dominant role in controlling the burning rate in the rocket range of pressure 3. A combustion model was proposed, assuming a partially vaporizing solid propellant and condensed-phase reactions playing a dominant role in the burning-rate control

temperature distribution and concentration profiles for the nine most prominent species. For RDX [54], the burning rate was predicted reasonably well in the pressure range of 10–40 atm, but for HMX [55] the burning rate was specified.

$$RDX_{(c),(g)} \rightarrow 1.5N_2 + N_2O + NO_2 + 3CH_2O, \tag{R.4}$$

$$\tfrac{5}{7}CH_2O + NO_2 \rightarrow NO + \tfrac{2}{7}CO_2 + \tfrac{3}{7}CO + \tfrac{5}{7}H_2O. \tag{R.5}$$

Cohen et al. [56] modified Ben-Reuven's HMX model [55] by including reactions among the decomposition products of HMX in the condensed phase (R.6)–(R.8) and the gas phase (R.9)–(R.12). A unity Lewis number and constant physical properties were assumed in the gas phase. They concluded that there is very little condensed phase decomposition and ~95% of the HMX evaporates. The model was able to match the measured pressure dependence of the burning rate.

Condensed phase:

$$HMX \rightarrow 4N_2O + 4CH_2O, \tag{R.6}$$

$$N_2O + CH_2O \rightarrow CO + H_2O + N_2, \tag{R.7}$$

$$CO + H_2O \rightarrow CO_2 + H_2. \tag{R.8}$$

Gas phase:

$$HMX \rightarrow 2N_2 + \tfrac{4}{3}N_2O + \tfrac{4}{3}NO_2 + 4CH_2O, \tag{R.9}$$

$$NO_2 + CH_2O \rightarrow CO + H_2O + NO, \tag{R.10}$$

$$N_2O + CH_2O \rightarrow CO + H_2O + N_2, \tag{R.11}$$

$$NO + CH_2O \rightarrow CO + H_2O + \tfrac{1}{2}N_2. \tag{R.12}$$

Lengellé et al. [57] developed a scheme for double-base propellants that solves the mass and energy conservation equations for both the condensed and gas phases. The species transport was treated using a temperature similarity parameter. Bizot and Beckstead [58] employed an approach similar to Lengellé et al. [57]. Three parallel reactions were considered in the condensed phase; a zeroth-order propellant degradation reaction, a first-order reaction of NO_2, and a second-order reaction of complex aldehydes. Four reactions were considered in the gas phase; a first-order reaction of NO_2, a second-order reaction of aldehydes, a first-order reaction of NO-carbon, and a second-order reaction of NO reduction. Mass diffusion and phase changes were neglected and constant properties were assumed. The calculations agreed fairly well with experimental data for the burning rate, surface temperature, and dark-zone thickness. Roh et al. [59] improved the double-base propellant combustion model by Bizot and Beckstead [58] to include two reactions (R.13) and (R.14) in the condensed phase and five reactions (R.14)–(R.18) in the gas phase. The mechanism led to an accurate prediction of the two-zone flame structure over a wide range of pressure. Good agreement with experimental data was achieved for the burning rate, temperature and species profiles, and dark-zone thickness

$$\mathrm{DB} \rightarrow 2.49\mathrm{NO_2} + 2.36\mathrm{CH_2O} + 1.26(\mathrm{CHO})_2 + 0.17\mathrm{CO} + \text{minor residual}, \quad \text{(R.13)}$$

$$\mathrm{NO_2} + 0.56\mathrm{CH_2O} + 0.16(\mathrm{CHO})_2 \rightarrow \mathrm{NO} + 0.38\mathrm{CO} + 0.5\mathrm{CO_2} + 0.5\mathrm{H_2O} + 0.22\mathrm{H_2}. \quad \text{(R.14)}$$

$$\mathrm{CH_2O} + \mathrm{CH_2O} \rightarrow \mathrm{CO} + 0.5\mathrm{C_2H_2} + \mathrm{H_2O}, \quad \text{(R.15)}$$

$$(\mathrm{CHO})_2 + (\mathrm{CHO})_2 \rightarrow 4\mathrm{CO} + 2\mathrm{H_2}, \quad \text{(R.16)}$$

$$\mathrm{NO} + 0.16\mathrm{CO} + 0.12\mathrm{C_2H_2} + 0.12\mathrm{H_2} \rightarrow 0.5\mathrm{N_2} + 0.4\mathrm{CO_2} + 0.36\mathrm{H_2O}, \quad \text{(R.17)}$$

$$\mathrm{C} + \mathrm{NO} \rightarrow \mathrm{CO} + 0.5\mathrm{N_2}. \quad \text{(R.18)}$$

For AP monopropellant, Guirao and Williams [38] first constructed a gas-phase kinetic mechanism consisting of 10 reactions, but reduced it to a single-step global reaction in order to obtain an analytical solution for the burning rate. Price et al. [8,60] developed a deflagration model for AP considering two parallel reactions in the gas phase. In the modeling of AP/HTPB composite propellant combustion, two-dimensional effects must be taken into account because of the involvement of diffusion flames [61–63]. Cai and Yang [62] developed a two-dimensional steady-state model for AP/HTPB accommodating finite-rate chemical kinetics with variable thermophysical properties. In the condensed phase, a zeroth-order AP decomposition (R.19) was taken into account. In the gas phase, in addition to (R.19), a global binder reaction with AP oxidizer products (R.21) was considered. Knott and Brewster [64] also developed a two-dimensional steady-state model for AP/HTPB composite propellant. A two-step global reaction sequence (R.19) and (R.21) similar to the chemical kinetics adopted by Cai and Yang [62] was employed. Recently, efforts have been applied by Jackson et al. [65–67] to study AP and AP/HTPB propellant combustion with complex particle packing. The multi-dimensional nature of the concerned physical models could only permit the use of simplified global kinetics. The initial two-dimensional heterogeneous combustion model that employed a two-step gas-phase kinetic scheme [66] was later improved to accommodate a three-dimensional, three-step reaction mechanism [67]. The model (R.19)–(R.21) captures the flame structure proposed by the original BDP combustion model [27]. An Arrhenius pyrolysis law, Eq. (37), is used to treat the surface regression without any explicit treatment of the condensed phase. The kinetic parameters [67] were treated as arbitrary coefficients and adopted so that the calculated one-dimensional AP and AP/HTPB burning rates could be predicted correctly. The model is capable of predicting the dependence of burning rate on pressure and the AP particle size

$$\mathrm{AP} \rightarrow \text{decomposition product } (Z), \quad \text{(R.19)}$$

$$\beta\mathrm{AP} + \text{binder } (Y) \rightarrow \text{final products}, \quad \text{(R.20)}$$

$$\beta Z + \text{binder } (Y) \rightarrow \text{final products}. \quad \text{(R.21)}$$

7. Combustion models based on detailed kinetics

7.1. Detailed gas-phase reaction mechanisms

A brief summary of the combustion models with detailed gas-phase kinetics through 1997 can be found in Refs. [5,68]. Table 3 lists some of the representative models and the gas-phase reaction mechanisms employed. Elementary kinetics were proposed for monopropellants such as AP, NG,

Table 3
Detailed gas-phase reaction models of monopropellant combustion, 1984–1998

Ingredient	Researchers	No. of species	No. of reactions	Comments
AP	Ermolin et al. (1984) [71]	24	80	Boundary conditions at the propellant surface were prespecified. Qualitative agreement was obtained with mass spectrometry data at 0.58 atm
AP	Narahari et al. (1984) [82]	14	17	A melt layer was considered in the condensed phase. The predicted burning rates are substantially lower than experimental values
AP	Sahu et al. (1990) [83]	18	22	ClO, an important species included in the conventional pathways, was not considered. Some rate constants were not reasonable. Eighty percent of AP was assumed to decompose in the condensed phase
AP	Cohen (1992) [84]	35	136	Reviewed several AP reaction mechanisms and proposed a new one. Rate constants for several important reactions were not provided
NG	Hatch (1986) [72]	21	60	Predicted the dark-zone temperature plateau. Burning-rate predictions do not match well with experimental data
DB	Anderson et al. (1995) [85]	41	189	The reaction mechanism was able to predict the dark-zone temperature plateau (1–30 atm)
RDX	Ermolin et al. (1986) [74]	23	90	Boundary conditions at the propellant surface were prespecified. Reasonable agreement with experimental data at 0.5 atm
HMX	Hatch (1987) [73]	25	77	Assumed two HMX decomposition pathways in the condensed phase; one leading to CH_2O and N_2O, and the other leading to HCN, NO_2, and H
RDX	Melius (1990) [75]	38	158	Properties and kinetic parameters were calculated using the BAC-MP4 (bound-additivity corrected Moller–Plesset fourth-order perturbation) technique
RDX	Yetter et al. (1995) [78]	38	178	Improvements to the Melius (1990) mechanism
ADN	Park et al. (1998) [86]	32	152	Studied the thermal decomposition of ADN by mass spectrometry under low pressure and performed kinetics modeling using *ab initio* method

nitramines (RDX and HMX), and ADN. Ermolin and coworkers measured concentration profiles for AP combustion at 0.58 atm [69] and proposed a detailed mechanism consisting of 24 species and 80 reactions [70]. The gas-phase conservation equations were solved by neglecting mass and thermal diffusion and prespecified boundary conditions at the propellant surface. Reasonable agreement was obtained between calculations and experimental data. The model was later improved by including mass and thermal diffusion to provide a more accurate prediction of the flame structure [71]. Hatch developed an NG combustion model [72] with a gas-phase reaction mechanism including 21 species and 60 reactions. Also proposed was an HMX combustion model [73] involving 25 species and 77 reactions. The formation of bubbles in the two-phase subsurface region, along with further reactions, was taken into account in both models. For NG, the dark-zone temperature plateau was predicted successfully but the modeling results were very sensitive to the rates of reactions involving HCO. In the case of HMX, results were presented for two different initial decomposition pathways, one leading to the formation of HCN and other to CH_2O. The models failed to match the burning-rate data accurately for both NG and HMX.

Ermolin et al. [74] developed a gas-phase kinetic mechanism consisting of 23 species and 90 reactions for RDX combustion. The measured

species concentrations at the propellant surface were used as input for the gas phase. Good agreement with experimental species–concentration profiles was achieved within 10% at 0.5 atm. Melius [75] developed an approach to calculate thermodynamic properties and reaction-rate constants for the decomposition of RDX vapor and other intermediate decomposition products. Based on this work, Melius proposed a 158-step reaction mechanism involving 38 species to describe the ignition of RDX [76], derived by extending a generalized hydrocarbon/air flame model by Miller and Bowman [77]. The mechanism includes oxidation of HCN, conversion of NH_x species to NO and N_2, and the flame chemistry of C_2N_2/NO_2. Additional reactions are considered to model the decomposition of RDX and the subsequent reactions of intermediate species. The condensed phase was treated with a single decomposition reaction, with evaporation serving as cold boundary condition to the gas phase. The model reasonably predicted the burning rate and the surface temperature at 1 and 20 atm. Yetter et al. [78] adopted the initial decomposition scheme of Melius for RDX monopropellant, but used a modified set of subsequent reactions. The model was based on a hierarchical approach for collecting kinetics data and the specific chemical submodels that are required to form the gas-phase combustion mechanisms. In particular, three submodels of increasing complexity (N_2O decomposition, H_2/NO_2 reaction, and CH_4/N_2O reaction) were established using the results from kinetics experiments over a broad range of temperature and pressure. The overall scheme consisting of 38 species and 178 reactions was later extended to 48 species and 228 reactions by Prasad et al. [79]. Chakraborty et al. [80] further added reactions involving the consumption of H_2CNNO_2, H_2CNNO, H_2CNO, and H_2CN, extending the RDX kinetics model to 49 species and 250 reactions. Cor and Branch [81] reviewed several mechanisms for solid-propellant combustion, with emphasis on those based primarily on the Miller–Bowman mechanism [77].

7.2. Detailed combustion models

The enormous growth in available computational speed, combined with improved experimental diagnostics, enabled further development of detailed combustion models. The combustion of several monopropellants, including RDX [6,17,75,76,78,79,87], HMX [7,22,88], GAP [11,89], BTTN [90], NG [16,91,92], NC and DEGDN [91], AP [93], and ADN [94–96], has been extensively studied by various researchers since the 1990s. The conservation equations are solved for both the condensed and gas phases, using detailed chemical kinetics in the gas phase and global reaction mechanisms in the condensed phase. The CHEMKIN/PREMIX package developed by Kee et al. [97,98] established a standard format for solving multi-component gas-phase equations with variable properties. Table 4 lists monopropellants that have been modeled using this paradigm. In addition to issues related to burning-rate characteristics, the existence of dark-zone temperature plateaus in nitrate ester and nitramine propellant flames has been addressed [16,92,99].

Efforts were also devoted to the modeling of binary pseudo-propellants such as RDX/GAP [23,100], HMX/GAP [20], and AP/HTPB [101], and ternary pseudo-propellants such as RDX/GAP/BTTN [102,103]. The composite systems of RDX/GAP, HMX/GAP and RDX/GAP/BTTN were selected as they are representative of existing non-AP propellants, and experimental data for nitramines/azide and RDX/GAP/BTTN was available [104–107]. Table 5 lists the pseudo-propellants that have been modeled. The pseudo-propellant models are typically based on the corresponding monopropellant models. One-dimensional transient models have also been developed to simulate processes such as oscillatory combustion [108,109], ignition [21,110–112], and fast cook-off [113]. Table 6 lists the experimental data used for validation in various models.

7.3. Chemical kinetics employed in detailed combustion models

The chemical kinetics schemes employed in various detailed combustion models are described herein. Thermal decomposition is usually neglected in modeling the solid-phase process due to the low-temperature condition and short residence time [6,17]. One exception is in the combustion models of AP monopropellant [93] and AP/HTPB pseudo-propellant [101], where a single global reaction accounting for solid AP decomposition was considered.

7.3.1. Subsurface chemical kinetics and phase transition

The subsurface two-phase region is typically on the order of tens of microns at one atmosphere and

Table 4
Monopropellant combustion models with detailed chemical kinetics, 1990–2005

Chemical family	Monopropellant	Researchers
Nitramine	RDX	Ermolin (1986, 2001) [74,114,115] Melius (1990) [76] Liau and Yang (1995) [6] Prasad et al. (1997) [79] Davidson and Beckstead (1997) [17] Miller and Anderson (2000) [16]
	RDX (ignition)	Liau et al. (2001) [21]
	HMX	Davidson and Beckstead (1996) [7] Prasad et al. (1998) [88] Kim (1999) [22]
	HMX (ignition)	Liau and Lyman (2002) [111] Meredith and Beckstead (2003) [112]
Azide	GAP	Davidson and Beckstead (1996) [89] Puduppakkam and Beckstead (2003) [11]
Nitrate esters	NG, DEGDN, NC (three nitration levels)	Miller and Anderson (2000, 2004) [16,91]
	NG	Puduppakkam and Beckstead (2005) [92]
	BTTN	Puduppakkam and Beckstead (2003, 2005) [90,92]
	TMETN	Puduppakkam and Beckstead (2005) [92]
AP	Perchlorate	Jing et al. (1998) [93]
AND	Nitrates	Liau et al. (1998, 1999) [94,96] Korobeinichev et al. (2001) [95]

Table 5
Pseudo-propellant combustion models with detailed chemical kinetics

Pseudo-propellant	Composition by mass fraction	Researchers
AP/HTPB	100% AP—77.5/22.5 AP/HTPB	Jeppson et al. (1998) [101]
RDX/GAP	100% RDX—70/30 RDX/GAP	Liau et al. (2000) [23]
	100% RDX—70/30 RDX/GAP	Puduppakkam and Beckstead (2002) [100]
HMX/GAP	100% HMX—70/30 HMX/GAP	Kim et al. (2002) [20]
HMX/GAP	80/20 HMX/GAP	Paletsky et al. (2005) [116]
M10	100% NC (three nitration levels)	Miller and Anderson (2004) [91]
M2	79.9/20.1 NC/NG	
M9	59.1/40.9 NC/NG	
JA2	60/15/25 NC/NG/DEGDN	
RDX/GAP/BTTN	70/9/21 RDX/GAP/BTTN	Puduppakkam and Beckstead (2003) [102]
	71/9/20 RDX/GAP/BTTN	Yoon et al. (2005) [103]

reduces to a few microns at rocket motor operating pressures. Experimental characterization of this region is very challenging because of the phase heterogeneity, spatially small dimensions of the reaction zone, and steep temperature and concentration gradients [13]. The reaction mechanisms typically include global decomposition steps, evaporation, and ensuing gas-phase reactions within the bubbles [6,7,17]. Experiments to analyze such processes in the subsurface region have been conducted at different heating rates; low-heating rate ($<10^3$ K/s), high-heating rate (up to 10^7 K/s), and combustion conditions ($\sim 10^7$ K/s) [13]. Low-heating rate studies provide the kinetic parameters for global reactions, while high-heating rate studies provide a more realistic set of species–concentration data. Experiments are typically performed at sub-atmospheric pressures as the flame is more spread out to allow more accurate diagnostics.

Based on experimental data, specific subsurface global kinetics models have been developed for different solid propellants. Only a few global

Table 6
Experimental data available for model validation

Propellant	Researchers	Type of data	Comments
AP	Ermolin et al. (1982) [70]	Spatial variation of mass fractions of H_2O, HCl, O_2, $HClO_4$, Cl_2, ClOH, NO, NO_2, N_2O, ClO_2	0.5 atm
AP, HMX, RDX, ADN, CL-20, HNF	Atwood et al. (1999) [117,118]	Burning rate r_b (P, T_{init})	2.4–3450 atm, using cinephotomicrography and closed bomb techniques
RDX	Korobeinichev et al. (1985) [119]	Spatial variation of mass fractions of H_2O, N_2, HCN, CO, NO	0.5 atm, using mass spectrometry
RDX	Ermolin et al. (1986) [74]	Spatial variation of mass fractions of H_2O, N_2, HCN, CO, NO, HNCO, NO_2, H_2CO, H_2, N_2O	0.5 atm
RDX, HMX	Zenin (1995) [15]	Spatial temperature distribution $T(x)$, r_b, surface temperature T_s, melt layer thickness l_{melt}	1–90 atm, using micro-thermocouples
RDX, HMX, XM39, HNF	Parr and Hanson-Parr (1994, 1995) [120–122]	$T(x)$, r_b, r_b (laser), spatial variation of mass fractions of NO,CN,OH,NH,NO_2, H_2CO	With and without laser at 1 atm, using UV absorption spectroscopy, PLIF (planar laser induced fluorescence), micro thermocouples
RDX, HMX, XM39, M43, GAP	Litzinger and coworkers (1995, 1999) [123–126]	$T(x)$, spatial variation of mass fractions of H_2O, HCN, CO, N_2, NO_2, CO_2, H_2, N_2O, CH_2O, NO, r_b (laser)	Laser-assisted combustion at 1 atm, using microprobe/mass spectrometry
HMX	Boggs (1984) [127]	r_b (P, T_{init})	1–3450 atm, using high-pressure window bomb and closed bomb
GAP, BAMO	Kubota and coworkers (1988, 1990, 1995) [128–130]	r_b, $T(x)$	1–50 atm, using microphotography and differential scanning calorimetry (DSC)
GAP	Flanagan et al. (1986) [131]	r_b, spatial variation of mass fractions of N_2, HCN, NH_3, CO, CH_2O, H_2, CH_4, C_2H_2, H_2O	6.8–68 atm
GAP	Korobeinichev et al. (2002) [132]	r_b, spatial variation of mass fractions of N_2, HCN, NH_3, CO, CH_2O, H_2, CH_4, C_2H_2, H_2O	1–20 atm, using mass spectroscopy
BTTN	Parr and Hanson-Parr (2002) [133]	$T(x)$	~1 atm, using spontaneous Raman spectroscopy
BTTN, NG, TMETN	Roos and Brill (2002) [134]	Spatial variation of mass fractions of NO, CO, NO_2, CH_2O, H_2, O_2, CH_4, CO_2, H_2O	5 atm, using T-Jump/FTIR and T-Jump/Raman spectroscopy
NG	Andreev (1957) [135]	r_b	10–100 atm
ADN	Fetherolf and Litzinger (1998) [136]	$T(x)$, spatial variation of mass fractions of H_2O, NH_3, N_2, NO_2, N_2O, NO	Laser assisted at 1–5 atm, using microprobe/mass spectrometry
ADN	Korobeinichev et al. (1988) [137]	r_b, $T(x)$, spatial variation of mass fractions of H_2O, NH_3, N_2, HNO_3, N_2O, NO	1–6 atm, using mass spectrometry

Table 6 (*continued*)

Propellant	Researchers	Type of data	Comments
RDX/BAMO RDX/GAP HMX/GAP	Litzinger et al. (2000) [138]	$T(x)$, spatial variation of mass fractions of N_2, HCN, NH_3, CO, H_2O, H_2, CH_4, CO_2, N_2O, NO_2	1 atm, using triple quadrupole mass spectrometry (TMQS)
GAP/HMX	Kubota and Sonobe (1990) [105]	r_b, $T(x)$	3–60 atm, using micro-photographs and micro-thermocouples
AP/HTPB	Korobeinichev et al. (1992) [139]	$T(x)$, spatial variation of mass fractions of HCl, H_2O, CO, NH_3, CO_2, NO, O_2, H_2, NO_2, N_2, HCN	0.08 atm
RDX/GAP/BTTN HMX/GAP/BTTN	Parr and Hanson-Parr (2001, 2002) [107,140]	$T(x)$, spatial variation of mass fractions of CO, NO, H_2, N_2, HCN, H_2O	~1 atm, using UV absorption spectroscopy, PLIF, micro-thermocouples

$T(x)$ is the spatial temperature distribution, r_b is the burning rate.

reaction steps are used to represent the complex chemistry in the subsurface layer. Table 7 provides a general description of chemical mechanisms employed in various models. The number of reactions increases for pseudo-propellants due to the involvement of more than one ingredient. Models describing experimentally well-investigated ingredients such as RDX usually consist of more reaction steps on account of the improved understanding, while those describing ingredients such as NG or BTTN have fewer steps. The ADN combustion model did not include a condensed-phase mechanism at all because of a lack of experimental data [94].

The pre-exponential factors in the rate equations are usually the most uncertain inputs, fitted to match the measured burning rate and distributions of temperature and species concentrations. Parametric and sensitivity studies are usually performed to evaluate the impact of such uncertainties due to pre-exponential factors. There are similarities in the chemical pathways and activation energies of the initial decomposition processes for ingredients belonging to the same chemical family. A significant trend can be noted based on the kinetics data reported in several experimental studies. Table 8 shows some of the similarities in the condensed-phase kinetic pathways and activation energies for ingredients belonging to nitramine, nitrate ester, and azide families. The experimentally measured surface decomposition products are also similar for ingredients from the same family. For azides (e.g., GAP, BAMO, and AMMO), N_2 was a dominant surface species (typically ~40%), along with CO, CH_2O and HCN (e.g. see Ref. [126]). Nitrate esters (BTTN, NG, PETN, NC, TMETN, TEGDN, PGN and PVN) are known to yield large concentrations of the decomposition gases NO and CO at the surface [134,141,142]. This supports the observation that similar processes occur for ingredients belonging to the same chemical family, consistent with Zenin's observation of a 'universal pyrolysis law' [15] for nitrate ester compound, and the Miller/Anderson approach [16] to describe condensed-phase activity with an Arrhenius-like expression [143].

The trends set out in Table 8 can be helpful in the construction of a mechanism for an ingredient belonging to a particular family. For example, while modeling BTTN monopropellant combustion, there was a lack of experimental data for the condensed-phase activation energy [90]. Extensive sets of data available for other nitrate esters were used with success in the modeling of the BTTN condensed-phase processes [90]. A model of a given ingredient can thus be extended to other ingredients of the same chemical family. Accordingly, several nitrate esters, including TEGDN, and PETN, can possibly be treated by extending the condensed-phase models for NG and BTTN. Similarly, azides such as BAMO and AMMO can be modeled by extending the analysis for GAP [11]. Subsurface two-phase models for pseudo-propellants are established based on the models for the constituent ingredients [20,23,100–103]. Reactions accounting for the interaction between different ingredients in a pseudo-propellant have also been considered, wherever applicable [20,23,101,103].

Table 9 summarizes the treatment of the condensed-phase reaction mechanism, including chemical reactions and rate parameters that were used in

Table 7
Chemical reaction mechanisms used in detailed combustion models

Compound	Researchers	Condensed phase			Gas phase	
		Decomposition	Evaporation	Gas-phase species reactions	Species	Reactions
RDX	Liau and Yang [6]	2	1	1	38	178
	Prasad et al. [79]	2	at surface	1	48	228
	Davidson and Beckstead [17]	2	1	1	45	231
RDX (Ignition)	Liau et al. [21]	2	1	1	49	250
HMX	Prasad et al. [88]	2	at surface	1	48	228
	Davidson and Beckstead [7]	2	1	1	45	232
HMX (Ignition)	Liau and Lyman [111]	—	1	—	45	232
	Meredith and Beckstead [112]	2	1	1	45	231
GAP	Davidson and Beckstead [89]	4	—	—	58	292
	Puduppakkam and Beckstead [11]	2	—	—	74	460
AP	Jing et al. [93]	4	—	—	33	79
BTTN	Puduppakkam and Beckstead [90]	1	1	—	85	538
NG	Miller and Anderson [16]	1	—	—	35	178
	Puduppakkam and Beckstead [92]	1	1		85	538
ADN	Liau et al. [94,96]	—	—	—	33	180
	Korobeinichev et al. [95]	—	—	—	31	172
AP/HTPB	Jeppson et al. [101]	8	—	—	44	157
RDX/GAP	Liau et al. [23]	4	1	5	71	520
	Puduppakkam and Beckstead [100]	4	1	1	76	488
HMX/GAP	Kim et al. [20]	4	1	5	74	532
RDX/GAP/BTTN	Puduppakkam and Beckstead [102]	5	2	1	76	488
	Yoon et al. [103]	5	2	5	72	429

the case of binary pseudo-propellant HMX/GAP and RDX/GAP [20,23]. The GAP sample considered [20] is composed of 56 monomer units, and denoted 'GAP56'. The models take into account the thermal decomposition of HMX (or RDX) and GAP, as well as subsequent reactions in the gas bubbles. Two global-decomposition pathways are employed for HMX (or RDX). Reaction (R.22) is an exothermic low-temperature pathway, whereas (R.23) is an endothermic high-temperature pathway. Subsequent reactions among the products of (R.22) and (R.23) may occur, and the reaction (R.27) between CH_2O and NO_2 is considered the most probable [157]. Thermodynamic phase transition consisting of both evaporation and condensation of HMX (R.26), is included to provide a complete description of the mass transfer process. A global, condensed-phase decomposition mechanism for GAP was established based on experimental data [126,147,158]. A first-order reaction is used with the pre-exponential factor and activation energy deduced by Sysak et al. [158], given by (R.24). The subsequent step in the decomposition of GAP releases NH_3. Finally, a rapid, highly exothermic event takes place, releasing HCN, CO, CH_2O, CH_2CO, CH_4, C_2H_4, H_2O, and GAP oligomers, in addition to NH_3 [147]. A species balance of the data acquired by Tang et al. [126] leads to a global reaction (R.25). To allow for a reduction of aldehydes (CH_3CHO and C_2H_3CHO) and imines (CH_3CHNH and $CH_2CHCHNH$), bimolecular decomposition reactions have also been formulated [23] as (R.28)–(R.31). In the subsurface layer, species $GAP56_{(l)}$, $GAP56^*_{(l)}$, and $C_{(s)}$ are dissolved in liquid HMX (or RDX), whereas all other species are gaseous and exist in bubbles.

Table 10 shows the 8-step subsurface chemical mechanism (R.32)–(R.39) and the corresponding

Table 8
Similarities in the chemical pathways in the subsurface region among ingredients from the same chemical family

Chemical family	Ingredients	Activation energy (kcal/mol)	Kinetic pathway	References	Comments
Nitramines	RDX, HMX	~50, with wide scatter	Parallel reactions; exothermic one leading to CH_2O and endothermic one leading to HCN	From summaries of Refs. [127,144]	
Nitrate esters	NG	34.4 ± 1.5, 35.1, 36, 40–45, 46.9	Initiation by the breaking of O-NO_2 bond (Refs. [57,144–146]	From summaries of Refs. [57,144]	Several nitrate esters have a similar activation energy of ~40 kcal/mol
	NC	30.7, 41.2, 43, 47		From summary of Ref. [57]	
	NG + NC	35.6, 41, 45.3		From summaries of Refs. [57,144]	
	CH_3O-NO_2, C_2H_5O-NO_2	39.5, 38, respectively		From summary of Ref. [57]	
Azides	GAP	32.4, 37, 39.3, 39.4 ± 1.1, 41.5, 41.6, 42.2, 43,	Initiation by the breaking of azide bond (–N_3) to release N_2 (Refs. [126,128,147–149])	Refs. [128,148,150–155]	Several azides have a similar activation energy of ~40 kcal/mol
	BAMO	43.2 ± 2.8, 43.5, 36, 40.8 ± 1.9, 42.7		Refs. [150,152,156]	
	AMMO	40.9 ± 0.8		Ref. [152]	

Table 9
Subsurface reaction mechanisms and rate parameters for HMX/GAP and RDX/GAP [20,23]

No.	Reaction	A^a	E^a	Ref.
(R.22)	$HMX_{(l)}$ ($RDX_{(l)}$) → 4(3)CH_2O + 4(3)N_2O	5.81×10^{10} ($1.00 \times 10^{13.78}$)	34,000 (36,000)	[7] [23,157]
(R.23)	$HMX_{(l)}$ ($RDX_{(l)}$) → 4(3)HCN + 2(1.5) (NO_2 + NO + H_2O)	1.66×10^{14} ($1.00 \times 10^{16.4}$)	44,100 (44,100)	[7] [23,157]
(R.24)	$GAP56_{(l)} \rightarrow GAP56^*_{(l)} + 56N_2$	5×10^{15}	41,500	[23]
(R.25)	$GAP56^*_{(l)} \rightarrow 25.6HCN + 15.8CO + 14.4NH_3 + 17.8CH_2O + 16CH_3CHO + H_2O + 6.4C_2H_3CHO + 1.5C_2H_4 + 8CH_3CHNH + 8CH_2CHCHNH + 14.6C_{(s)}$	1.28×10^{19}	53,000	
(R.26)	$HMX_{(l)} \Leftrightarrow HMX_{(g)}$ $RDX_{(l)} \Leftrightarrow RDX_{(g)}$	Ref. [6]	—	
(R.27)	$CH_2O + NO_2 \rightarrow CO + NO + H_2O$	$802 \times T^{2.77}$	13,730	
(R.28)	$CH_3CHO + M = CH_3 + HCO + M$	7×10^{15}	81,770	
(R.29)	$C_2H_3CHO + M = C_2H_3 + HCO + M$	10^{16}	97,600	
(R.30)	$CH_3CHNH + M = CH_3 + H_2CN + M$	10^{16}	63,700	
(R.31)	$CH_2CHCHNH + M = C_2H_3 + H_2CN + M$	10^{16}	66,900	

$k = A \exp(-E/R_u T)$.
[a]Units are in mol, cm, s, K, and cal.

rate parameters that were used in the case of binary pseudo-propellant AP/HTPB [101]. Reactions (R.36)–(R.39) were employed to describe a model of the condensed-phase mechanisms for AP monopropellant [93]. Table 11 shows the condensed-phase mechanisms (R.40)–(R.45), considered by Puduppakkam and Beckstead in the case of NG, BTTN, and TMETN monopropellant models [92].

Some researchers have used simplified modeling approaches to treat the condensed phase without solving for the conservation equations. Ermolin et al. [70,74] employed the experimentally determined surface temperature and major species concentrations at the propellant surface at a low pressure as the boundary condition for solving the gas-phase equations. Miller and Anderson [16,87] did not model the condensed-phase structure either, but computed the mass-burning rate iteratively by matching the heat flux at the propellant surface. In addition, they employed an Arrhenius-like pyrolysis

Table 10
Subsurface reaction mechanisms and rate parameters for AP/HTPB [101]

No.	Reaction	A^a	E^a	Ref.
(R.32)	$HTPB(1200)_{(l)} \rightarrow 2HTPB(580)_{(l)} + 3C_{(s)} + H_2$	1.0×10^{10}	10,000	[101]
(R.33)	$HTPB(580)_{(l)} \rightarrow 10C_4H_6 + C_2H_3 + CH_3$	2.0×10^{11}	10,000	
(R.34)	$HTPB(580)_{(l)} + 15AP \rightarrow 20CO + 10HCN + 13\ CH_4 + 32H_2O + 8ClO + 7Cl + 5N$	3.2×10^{11}	10,000	
(R.35)	$HTPB(580)_{(l)} + 20HClO_4 \rightarrow 8CO + 24CO_2 + 24H_2O + 20HCl + 5C_2H_2 + CH_4 + 2H_2$	1.0×10^{12}	10,000	
(R.36)	$AP_{(l)} \rightarrow NH_3 + HClO_4$	8.0×10^{12}	28,000	[159]
(R.37)	$AP_{(l)} \rightarrow H_2O + O_2 + HCl + HNO$	1.0×10^{8}	22,000	
(R.38)	$AP_{(l)} \rightarrow 2H_2O + Cl + NO_2$	5.0×10^{7}	22,000	
(R.39)	$AP_{(l)} \rightarrow ClO_3 + NH_3 + OH$	1.0×10^{9}	22,000	

$k = A\exp(-E/R_uT)$.
[a]Units are in mol, cm, s, K, and cal.

Table 11
Subsurface reaction mechanisms and rate parameters for nitrate esters

No.	Reaction	A^a	E^a	Ref.
(R.40)	$NG_{(l)} \rightarrow 3NO + 1.75CO + 1.75H_2 + 1.25CO_2 + 0.75H_2O + 0.5O_2$	1.0×10^{17}	20,130	[92]
(R.41)	$NG_{(l)} \Leftrightarrow NG_{(g)},\ P_v(\text{atm}) = 6.7 \times 10^8 \exp(-10{,}322/T)$			
(R.42)	$BTTN_{(l)} \rightarrow 2.2NO + 2.2CO + 1.5H_2 + 0.8CO_2 + 0.6H_2O + 0.6O_2 + 0.4CH_4 + 0.4CH_2O + 0.4NO_2 + 0.2N_2 + 0.1C_2H_4$	1.0×10^{17}	20,130	
(R.43)	$BTTN_{(l)} \Leftrightarrow BTTN_{(g)},\ P_v(\text{atm}) = 1.22 \times 10^9 \exp(-10{,}825/T)$			
(R.44)	$TMETN_{(l)} \rightarrow 1.875NO + 2.5CO + 1.125H_2 + 1.3125CH_4 + 0.6875CO_2 + 0.75O_2 + 0.25H2O + 0.3125\ N_2 + 0.5NO_2 + 0.5CH_2O$	1.0×10^{17}	20,130	
(R.45)	$TMETN_{(l)} \Leftrightarrow TMETN_{(g)},\ P_v(\text{atm}) = 5.45 \times 10^8 \exp(-10{,}590/T)$			

$k = A\exp(-E/R_uT)$.
[a]Units are in mol, cm, s, K, and cal.

expression to relate the mass burning rate and the surface temperature.

7.3.2. Detailed chemical kinetics for the gas-phase region

Analyzing the combustion of mono- and pseudo-propellants from an elementary level helps improve the predictive ability of the model, and can be achieved by using detailed chemical kinetics in the gas phase. The approaches used by most researchers to model the gas phase are very similar. For a set of N_R elementary reactions involving N species, the chemical reaction equations can be written in the general form

$$\sum_{i=1}^{N_g} \nu'_{ij} M_i \underset{k_{bj}}{\overset{k_{fj}}{\Leftrightarrow}} \sum_{i=1}^{N_g} \nu''_{ij} M_i, \quad j = 1, 2, \ldots, N_R, \tag{49}$$

where ν'_{ij} and ν''_{ij} are the stoichiometric coefficients for the ith species appearing as a reactant in the jth forward and backward reactions, respectively, and M_i is the chemical symbol for the ith species. The reaction rate constant k_j (either k_{fj} or k_{bj}) is given by the Arrhenius expression,

$$k_j = A_j T^{B_j} \exp\left(-E_j/R_uT\right). \tag{50}$$

The rate of change of molar concentration of species i by reaction j is

$$\dot{C}_{ij} = \left(\nu'_{ij} - \nu''_{ij}\right)\left(k_{fj}\prod_{i=1}^{N_g} C_i^{\nu'_{ij}} - k_{bj}\prod_{i=1}^{N_g} C_i^{\nu''_{ij}}\right). \tag{51}$$

The total mass production rate of gaseous species i in Eq. (16) is then obtained by summing up the changes due to all gas- and condensed-phase reactions:

$$\dot{w}_{g_i} = \phi_g W_{g_i} \sum_{j=1}^{N_R} \dot{C}_{ij} + \dot{w}_{c-g,g_i}. \tag{52}$$

It must be noted that Eq. (51) is strictly valid for elementary reactions. If a global kinetics scheme is used, the exponents for molar concentrations may

be varied from their stoichiometric coefficients in order to match experimental data.

The gas-phase process is relatively well understood as compared to the subsurface layer. Table 12 lists several detailed kinetic mechanisms that have been developed independently over the years based on both experimental data and theoretical predictions. These include the Yetter et al. mechanism for RDX [78], the GRI mechanism for natural gas [160], the Miller/Anderson mechanism for NG [16], the Korobeinichev/Ermolin mechanism for AP [161], and the Lin and Park mechanism [94] for ADN combustion. Table 7 describes the detailed gas-phase reaction mechanisms adopted in the various combustion models. The Yetter mechanism [78] has been used by Prasad et al. [79], Liau and Yang [6], and Davidson et al. [17], as the basis for modeling RDX monopropellant combustion. A few modifications to the Yetter mechanism [78] were subsequently made for treating HMX [7,88]. The Miller/Anderson mechanism for NG was developed to simulate the dark-zone temperature plateau and ignition-delay characteristics of gun propellants [16]. The AP combustion model by Jing et al. [93] was based on a modified Ermolin mechanism [161].

Considering the wide range of ingredients available, it is desirable to develop a common and universal platform for modeling mono- and pseudo-propellants. Efforts are underway to integrate various mechanisms to form a unified framework capable of analyzing and predicting the combustion characteristics of different solid propellants. The similarities between the reaction mechanisms of various compounds make this approach feasible. Most solid propellants are composed of the atomic species C, H, O, and N. While the initial decomposition pathways are markedly different for various ingredients, they eventually decompose to similar gas-phase species. For example, CO, CH_2O, HCN, NH_3, H_2O and N_2 have been observed with varying concentrations in the gas phases during the combustion of nitramines, azides, and nitrate esters. Consequently, the gas-phase mechanisms developed for a particular ingredient can be extended for other ingredients provided the initial decomposition schemes are known. This has especially been the case for pseudo-propellants. For example, the AP/HTPB combustion was modeled [101] based on reactions from the AP/CTPB [139], AP [161], and GRI [160] mechanisms. RDX/GAP was treated [23] using a combination of the Yetter mechanism for RDX [78] and the GRI mechanism [160]. The chemical kinetics schemes for GAP [11], BTTN [90], RDX/GAP [100], and RDX/GAP/BTTN [102,103] were essentially derived from the RDX [78], GRI [160], AP [161], and NG [16] mechanisms, along with additional reactions proposed by Park et al. [162].

Table 12
Gas-phase reaction mechanisms used in different detailed combustion models

Mechanism	Species	Reactions
GRI [160]	53	325
RDX [78]	45	232
NG [16]	35	178
ADN [94]	33	180
AP [161]	33	79
AP/CTPB [139]	35	58

It is noteworthy that there are uncertainties associated with the kinetic parameters of some reactions. Consequently, a same reaction present in different mechanisms may have slightly different kinetic parameters based on the corresponding literature sources. In some of the mechanisms (e.g., the GRI mechanism [160]), the kinetic parameters may be adjusted within the uncertainty limits. The number of such reactions, however, is relatively small, and the differences in the kinetic parameters are typically not large. Although such differences usually do not affect the calculated characteristics significantly, some reactions may bear a large impact. Thus, while assembling mechanisms based on multiple sources, care must be taken to evaluate the differences in the kinetic parameters. With caution, it seems possible to assemble a single comprehensive mechanism that can eventually be applied to several different compounds. The only ingredient-specific information needed will be obtained from the corresponding condensed-phase mechanisms.

7.3.3. Thermophysical properties of solid-propellant ingredients

The thermal conductivities and specific heats as a function of temperature of such solid-propellant ingredients as RDX, HMX, and GAP have been obtained by Hanson-Parr and Parr [163]. For liquid RDX, these properties are not available in the literature, and are assumed to have the same values as their solid counterparts [6,20], extrapolated to a slightly higher temperature. The thermal conductivity of liquid HMX was reported by Bedrov et al.

[164] and is consistent with the previously evaluated values. Table 13 provides the thermophysical properties of commonly used ingredients such as HMX, RDX, GAP, BTTN, NG, AP, HTPB, and ADN.

7.4. Numerical treatment

The theoretical formulation requires a time-accurate analysis and a robust computational scheme due to the numerical stiffness caused by chemical reactions and transport processes. All the conservation equations and associated boundary conditions are coupled and solved by an iterative procedure. The specific numerical approach depends on individual researchers. For example, Yang and colleagues used a double-iteration procedure [6,20,21,23,103], which treats the propellant surface temperature T_s, and burning rate r_b as eigenvalues. The procedure continues with T_s adjusted by an inner loop while r_b is corrected by the outer iteration. The conservation equations for the subsurface region are solved first. The resulting species concentrations at the surface are then used as the boundary conditions for the gas-phase region through the interfacial matching conditions. The next step involves integration of the gas-phase conservation equations to provide the spatial variations of the temperature and species concentrations. The non-equilibrium evaporation rate, Eq. (27), is employed to check the convergence of T_s. If this is not successful, another inner iteration is repeated using an updated value of T_s. The outer iteration follows the same procedure as the inner loop, except that r_b is used as the eigenvalue to check the interfacial energy continuity, Eq. (26). Since only the burning rate and surface temperature, not the interfacial species composition, are involved in the iterative procedure, the algorithm performs well and significantly reduces the computational burden.

The conservation equations (3)–(6) for the subsurface region are fully coupled. They are, however, solved in an uncoupled-iteration manner. The method starts with an estimated temperature profile obtained by solving an inert energy equation. The conservation equations of mass and species concentrations are then integrated by means of the fourth-order Runge–Kutta method. Eq. (6) is subsequently solved with the newly obtained void fraction and species concentrations to obtain another temperature profile. Since the equations are solved separately, iterations are required to ensure a converged solution that satisfies all the conservation laws and boundary conditions.

In solving the conservation equations for a chemically reacting flow in the gas phase, numerical stiffness problems are encountered due to the existence of a wide variety of time and length scales. If a two-phase formulation is used to accommodate condensed-phase particles, then the governing equations (14)–(17) are fully coupled. They are solved using an uncoupled-iteration method similar to the subsurface solver. Eq. (15) is first treated using a fourth-order Runge–Kutta method to determine the void fraction and the mass fractions of condensed species. Eqs. (14), (16) and (17) are then solved using the CHEMKIN/PREMIX package [98] with some modifications to account for a two-phase system. The numerical grids for the two solvers are different and direct interpolation is applied to match the grid information.

7.5. Modeling results and discussions

The calculated combustion characteristics from detailed models include the pressure and temperature sensitivities of the burning rate, spatial distributions of temperature and species concentrations, and propellant surface conditions. Representative results for the combustion of mono- and pseudo-propellants are presented below.

7.5.1. Combustion of monopropellants and pure ingredients

The monopropellants modeled with detailed chemistry, as listed in Table 4, represent a very diverse set of ingredients with some rather unique combustion characteristics. In general, the compounds are made up of the atomic species C, H, O, and N, with the exceptions of AP (excluding C and including Cl) and ADN (excluding C). AP and ADN are oxidizer-rich; GAP is a fuel-rich binder, whereas RDX, HMX, NG, and BTTN are relatively stoichiometric. The equilibrium flame temperatures range from ~1400 K for AP to greater than 3000 K for nitramines. A dark-zone temperature plateau exists in the range of 1–50 atm for nitrate esters [99,168] and up to 40 atm for ADN [10]. GAP [128,148,169], ADN [170], and AP [93] are known to release a significant amount of energy in the condensed phase, whereas the nitramines RDX and HMX release most of their energy in the gas-phase [7,17].

Table 13
Thermophysical properties of HMX, RDX, GAP, BTTN, NG, AP, HTPB, and ADN

Parameter	Units	Value	Ref. or comment
$c_{p,s,\mathrm{HMX}}$	cal/g K	$4.980\times10^{-2}+0.660\times10^{-3}\times T$	[163]
$c_{p,l,\mathrm{HMX}}$	cal/g K	$4.980\times10^{-2}+0.660\times10^{-3}\times T$	$c_{p,l,\mathrm{HMX}}=c_{p,s,\mathrm{HMX}}$
$c_{p,s,\mathrm{RDX}}$	cal/g K	$4.861\times10^{-3}+0.843\times10^{-3}\times T$	[163]
$c_{p,l,\mathrm{RDX}}$	cal/g K	$4.861\times10^{-3}+0.843\times10^{-3}\times T$	$c_{p,l,\mathrm{RDX}}=c_{p,s,\mathrm{RDX}}$
$c_{p,l,\mathrm{GAP}}$	cal/g K	$1.503\times10^{-1}+0.966\times10^{-3}\times T$	[163]
$c_{p,l,\mathrm{NG}}$	cal/g K	0.298	[92]
$c_{p,l,\mathrm{BTTN}}$	cal/g K	0.30	[103]
$c_{p,s,\mathrm{AP}}$	cal/g K	0.287	[62]
$\lambda_{s,\mathrm{HMX}}$	cal/K s cm	1.500×10^{-3}–$0.115\times10^{-5}\times T$	[163]
$\lambda_{l,\mathrm{HMX}}$	cal/K s cm	1.500×10^{-3}–$0.115\times10^{-5}\times T$	$\lambda_{l,\mathrm{HMX}}=\lambda_{s,\mathrm{HMX}}$
$\lambda_{s,\mathrm{RDX}}$	cal/K s cm	0.665×10^{-3}	[163]
$\lambda_{l,\mathrm{RDX}}$	cal/K s cm	0.665×10^{-3}	$\lambda_{l,\mathrm{RDX}}=\lambda_{s,\mathrm{RDX}}$
$\lambda_{l,\mathrm{GAP}}$	cal/K s cm	1.050×10^{-3}–$0.146\times10^{-5}\times T$	[163]
$\lambda_{l,\mathrm{BTTN}}$	cal/K s cm	0.63×10^{-3}	[103]
$\lambda_{l,\mathrm{NG}}$	cal/K s cm	0.63×10^{-3}	[92]
$\lambda_{s,\mathrm{AP}}$	cal/K s cm	0.96×10^{-3}	[62]
$\rho_{s,\mathrm{HMX}}$	g/cm^3	1.9	[46]
$\rho_{l,\mathrm{HMX}}$	g/cm^3	1.9	$\rho_{s,\mathrm{HMX}}=\rho_{l,\mathrm{HMX}}$
$\rho_{s,\mathrm{RDX}}$	g/cm^3	1.8	[46]
$\rho_{l,\mathrm{RDX}}$	g/cm^3	1.8	$\rho_{l,\mathrm{RDX}}=\rho_{s,\mathrm{RDX}}$
$\rho_{l,\mathrm{GAP}}$	g/cm^3	1.3	[147]
$\rho_{l,\mathrm{BTTN}}$	g/cm^3	1.521	[103]
$\rho_{l,\mathrm{NG}}$	g/cm^3	1.6	[92]
$\rho_{s,\mathrm{AP}}$	g/cm^3	1.9	[62]
$\rho_{s,\mathrm{HTPB}}$	g/cm^3	0.95	[62]
$\rho_{s,\mathrm{ADN}}$	g/cm^3	1.8	[10]
$T_{\delta\rightarrow l,\ \mathrm{HMX}}$	K	558	[46]
$T_{\beta\rightarrow\delta,\ \mathrm{HMX}}$	K	460	[7]
$T_{m,\mathrm{RDX}}$	K	478	[46]
$T_{m,\mathrm{ADN}}$	K	365–368	[10]
$H_{v,\mathrm{HMX}}$	kcal/mol	38.7	[165]
$H_{\delta\rightarrow l,\mathrm{HMX}}$	kcal/mol	16.7	[166]
$H_{\beta\rightarrow\delta,\mathrm{HMX}}$	kcal/mol	2.35	[167]
$H_{v,\mathrm{RDX}}$	kcal/mol	26.8	[79]
$H_{\mathrm{fus,RDX}}$	kcal/mol	8.1	[46]
$H_{\mathrm{sub,RDX}}$	kcal/mol	34.9	$H_{v,\mathrm{RDX}}+H_{\mathrm{fus,RDX}}$
$H_{v,\mathrm{BTTN}}$	kcal/mol	21.517	[103]
$H_{v,\mathrm{NG}}$	kcal/mol	20.5	[92]

The burning rate is the most important characteristic in solid-propellant combustion. The pressure dependence of the burning rate is universally represented by

$$r_b = ap^n. \tag{53}$$

Fig. 4 shows the calculated burning rates for monopropellants RDX [17], NG [16], GAP [11], BTTN [92], and AP [93] using detailed reaction mechanisms in the gas phase. The various modeling calculations agree well with experimental data with different degrees of accuracy. The predictions match 67% of the measurements within $\pm10\%$ and all data within $\pm15\%$ for BTTN, 60% of the data within $\pm5\%$ and 83% of the data within $\pm7\%$ for AP, 60% of the data within $\pm10\%$ and 85% of the data within $\pm15\%$ for RDX, 80% of the data within $\pm10\%$ for GAP, and 82% of the data within $\pm15\%$ for NG. The burning rates of the different monopropellants shown in Fig. 4 vary by almost an order of magnitude. GAP has one of the highest burning rates, in spite of its lowest flame temperature. This phenomenon is attributed to a large heat release in the condensed phase. The flame temperatures of RDX, BTTN and NG are similar (~3000 K), yet their burning rates vary significantly. The pressure

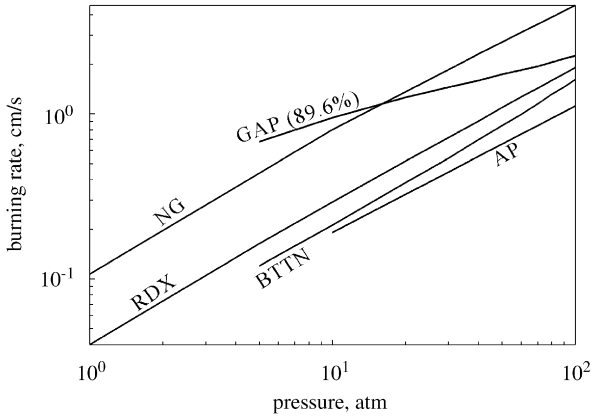

Fig. 4. Calculated burning rates of NG [16], AP[93], RDX [17], GAP [11], and BTTN [92] using detailed chemical kinetics in the gas phase.

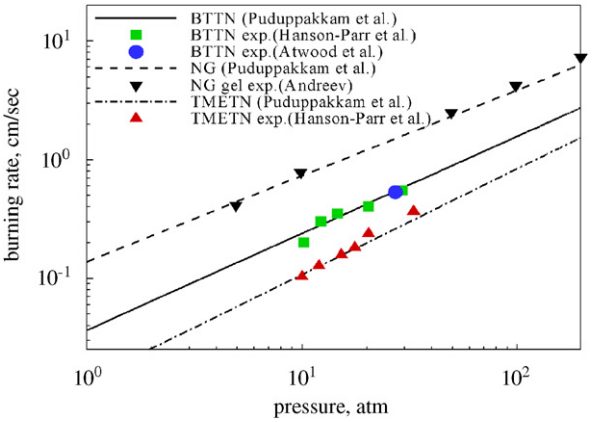

Fig. 5. Comparison of calculated [92] and measured burning rates of NG [135], BTTN [171] and TMETN [171].

exponents (n) of the calculated burning rates vary over a wide range (~0.4–0.85) for different ingredients. The values typically agree well with experimental data, within ±5%. The condensed-phase heat release is not significantly affected by pressure, mainly due to the global nature of the condensed-phase kinetics. The gas-phase reaction rates, however, are pressure dependent. With increasing pressure, the flame moves closer to the burning surface, thereby enhancing the heat feedback and increasing the burning rate. The pressure exponent thus provides a measure of the model accuracy in terms of the calculated gas-phase heat feedback and its impact on the burning rate.

Fig. 5 shows the calculated [92] and measured burning rates for the nitrate esters NG [135], BTTN [171], and TMETN [171]. The model predicts the wide range of burning rates fairly well. For TMETN, 66% of the experimental data is within ±10% of the calculations, and for NG and BTTN all data is within ±20% of the calculated values. The calculated pressure exponents for the burning rates of NG, BTTN and TMETN are 0.72, 0.82, and 0.89, respectively, showing a trend consistent with the corresponding experimental values of 0.77, 0.85, and 1.07. It is worth noting that although the condensed- and gas-phase reaction mechanisms and thermophysical properties of the three nitrate esters bear a close similarity, the model is sufficiently accurate to predict observed variations in burning rates. Fig. 6 shows the calculated [11] and measured [129,131] burning rates at 70 atm as a function of the azide content by varying the GAP mass fraction in the range of 75–90%. Excellent agreement between

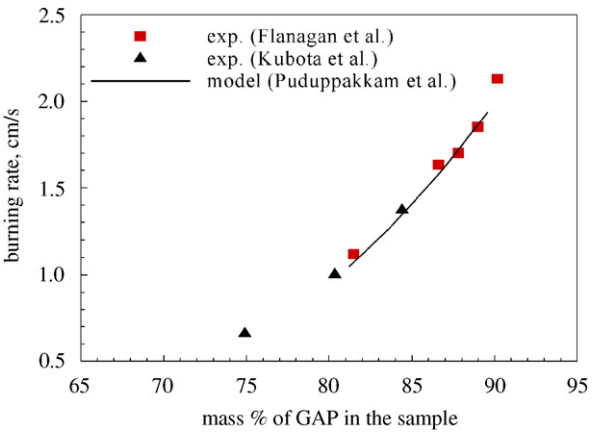

Fig. 6. Calculated burning rate [11] vs. mass percentage of GAP at 70 atm compared to experimental data [129,131].

the calculations and measurements is obtained. The burning rate for GAP has been observed to be strongly dependent on the amount of curative in the GAP polymer [131,169,172]. Kubota et al. [129] reported a correlation between the burning rate and N_3 bond energy contained within a unit mass of GAP. The burning rate increases significantly with increasing GAP content, nearly doubling over the range of bond-energy values typically used. The large effect of the azide content points to the significant impact of the condensed-phase energy release. The high burning rate of GAP results from the energy release close to the surface, even though the overall energy content is relatively low. Figs. 7 and 8 show the predicted [6] and measured [15,173,174] burning rates of RDX and HMX, respectively, as a function of pressure. The model

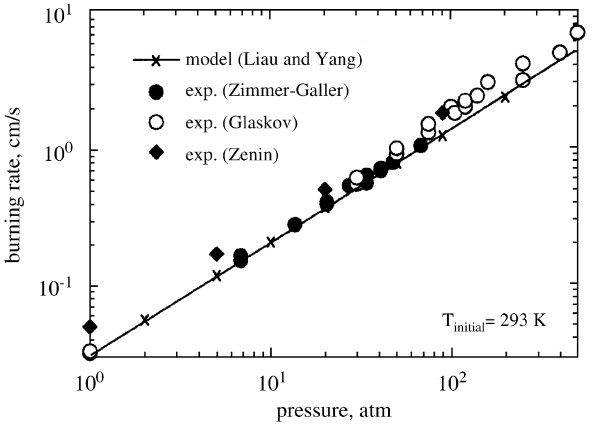

Fig. 7. Calculated [6] and measured [15,173,174] burning rates of RDX monopropellant as a function of pressure.

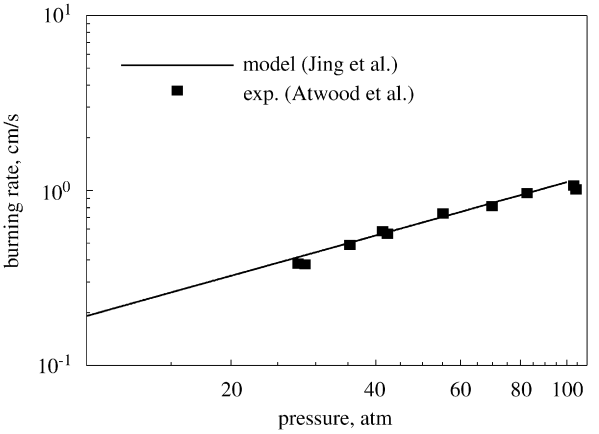

Fig. 9. Calculated [93] and measured [117] burning rates of AP monopropellant as a function of pressure.

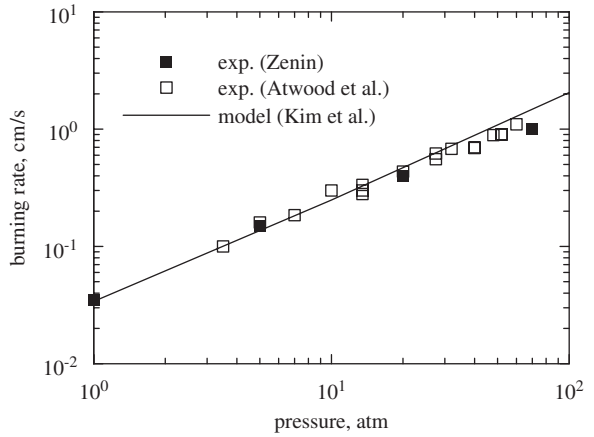

Fig. 8. Calculated [20] and measured [15,117] burning rates of HMX monopropellant as a function of pressure.

employs the gas-phase chemical kinetics mechanism proposed by Yetter et al. [78]. RDX and HMX have very similar burning rates in spite of the difference in the vapor pressure. The pressure exponent n in the burning-rate law is about 0.83 for RDX, and about 0.88 for HMX. Fig. 9 shows good agreement between the calculated [93] and measured [117] burning rates for AP monopropellant combustion. The pressure exponent is about 0.76.

In addition to the prediction of the burning rate and its pressure exponent, an advantage of the detailed combustion models lies in the capability to provide direct insight into the flame structure (including the temperature and species–concentration profiles) and heat-release mechanism, as well as the temperature sensitivity of the burning rate. The latter, defined as

$$\sigma_p = \left.\frac{\partial(\ln r_b)}{\partial T_i}\right|_p \tag{54}$$

is probably the most difficult property to match with experimental data, partly due to uncertainties in the condensed-phase mechanisms, and partly because it is a derivative quantity. Fig. 10 shows calculated and experimentally measured temperature sensitivities for AP, HMX, and RDX. For the range of propellant ingredients modeled, the temperature sensitivity varies from $\sim 0.001\,K^{-1}$ for nitramines such as RDX and HMX, to $\sim 0.004\,K^{-1}$ for nitrate esters such as BTTN, to $\sim 0.01\,K^{-1}$ for azides such as GAP. The temperature sensitivity is significantly affected by the condensed-phase heat release. Typically, monopropellants which have a large condensed-phase heat release exhibit high temperature sensitivity. Parametric studies for some models indicate that the thermophysical properties of the condensed phase also exert a substantial influence on the temperature sensitivity [11,90].

The experimental data in Fig. 10 indicates that the temperature sensitivity decreases with increasing pressure. At an elevated pressure, the enhanced heat transfer from the gas phase to the propellant surface due to increased energy release and reduced flame standoff distance overrides the influence of preconditioned temperature in determining the energy balance at the surface, and consequently the temperature sensitivity decreases. RDX and HMX both have very low values of the temperature sensitivity ($\sim 0.001\,K^{-1}$) at pressures above 50 atm,

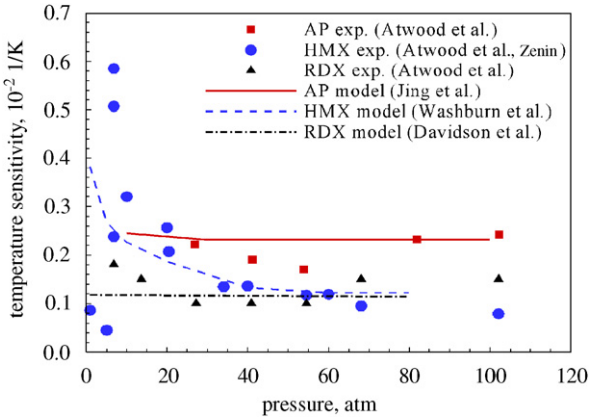

Fig. 10. Calculated temperature sensitivities of RDX [17], HMX [15,19] and AP [93] compared with experimental data [118].

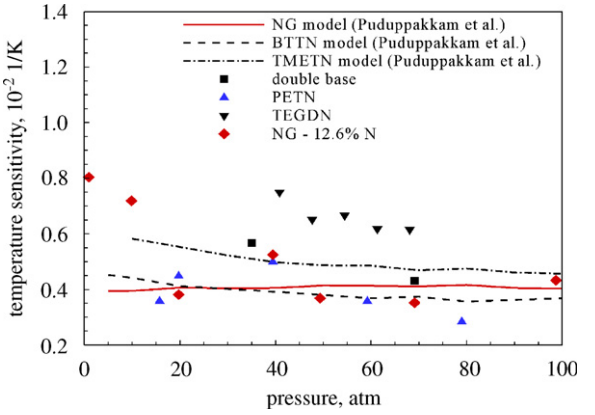

Fig. 11. Calculated temperature sensitivities [92] of nitrate esters, NG, BTTN and TMETN compared with experimental data [42,175].

but at pressures approaching 1 atm the values become close to 0.002 and 0.005 K^{-1}, respectively. Most existing models with detailed chemical kinetics [7,22,88] have not been able to reproduce this behavior. Some of the early simplified models [33,35,50,51] and a later simplified model [34] have shown the pressure dependence of the temperature sensitivity for either AP or HMX. But no model has been applied to both RDX and HMX to explore the underlying mechanisms for such a difference between the two monopropellants that are otherwise so similar in burning characteristics. However, a recent model of nitramine propellants developed by Washburn and Beckstead [19], which includes the surface tension of bubbles in the liquid layer, was able to predict the difference in the temperature sensitivities of RDX and HMX at lower pressures, as observed experimentally.

Fig. 11 shows the calculated [92] and measured [42,175] temperature sensitivities of the nitrate esters NG, BTTN and TMETN at 298 ± 50 K. The values for NG and BTTN are on the same order of magnitude, while TMETN has a slightly higher value. Owing to the lack of experimental data on the monopropellants, Fig. 11 compares the predicted values with the data summarized for double base propellants [42], and with the data on the nitrate esters PETN, TEGDN and NC from the FLAME database [175]. The predicted values are within the range of experimental measurements (recognizing the large scatter in the data). Nitrate esters, in general, seem to have relatively higher temperature sensitivities than typical solid-propellant ingredients (~0.001–0.002 K^{-1}). It should be noted that some of the data in Fig. 11 were obtained for initial temperature ranges different from those used in modeling calculations.

Experimental data for the temperature and species–concentration profiles, if available, provides a more comprehensive basis for model validation and improved understanding of the entire combustion process. Fig. 12 shows the predicted temperature distributions for self-sustained RDX combustion at various pressures [6]. The final flame temperature increases with increasing pressure, whereas the flame-standoff distance exhibits an opposite trend owing to enhanced chemical-reaction rates at higher pressures. Fig. 13 shows a comparison with the measured species–concentration profiles of the RDX monopropellant combustion at 0.5 atm, obtained by means of a time-of-flight mass spectrometry technique [119]. Good agreement was obtained except for the region very close to the burning surface. The discrepancy may be attributed to ambiguity in determining the precise location of the propellant surface in the experiments. Figs. 14 and 15 show the calculated temperature and species–concentration profiles in the gas-phase and subsurface region, respectively, at 90 atm [6]. The combustion-wave structure exhibits a close similarity to that at 1 atm, except for the shorter flame standoff distance (6 vs. 600 μm) and molten-layer thickness (2.1 vs. 66 μm). The shorter molten-layer thickness and higher burning rate yield a shorter residence time for condensed-phase reactions. As evidenced by the large ratio of HCN to CH_2O mole fraction, the endothermic decomposition to form HCN appears more profound at high-pressure conditions. This can be attributed to the higher surface temperature and heat transfer into the condensed phase. The species–concentration profiles

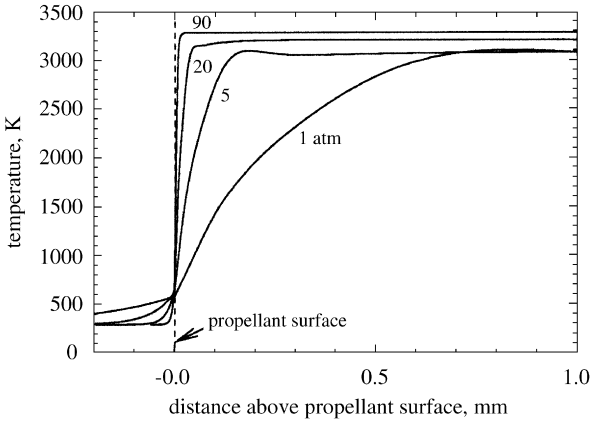

Fig. 12. Calculated temperature profiles [6] of self-sustained RDX combustion at various pressures.

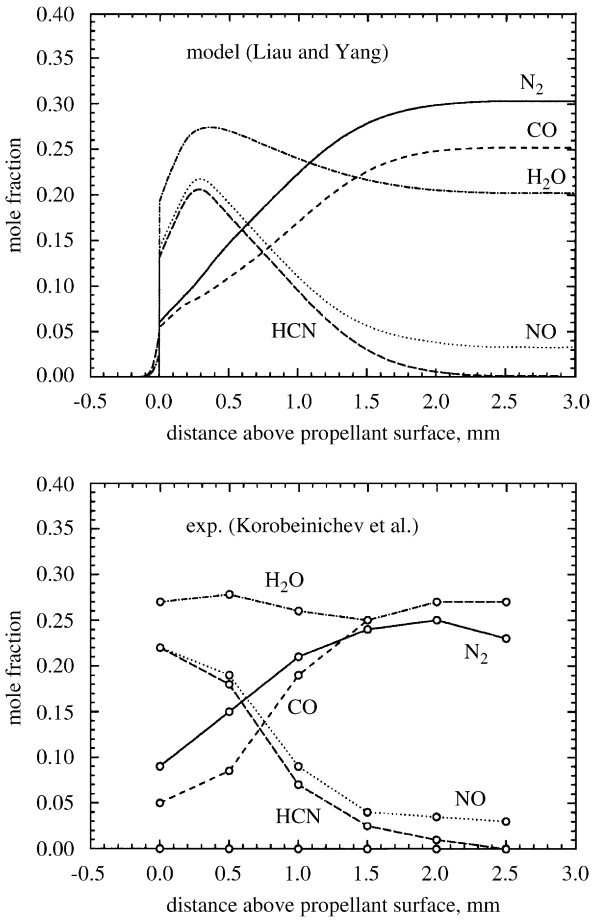

Fig. 13. Calculated [6] vs. measured [119] species–concentration profiles of self-sustained combustion of RDX at 0.5 atm.

revealed that the overall reaction mechanisms consist of three steps: (1) decomposition of RDX to CH_2O, HCN, NO_2, etc. near the surface, (2) first-stage

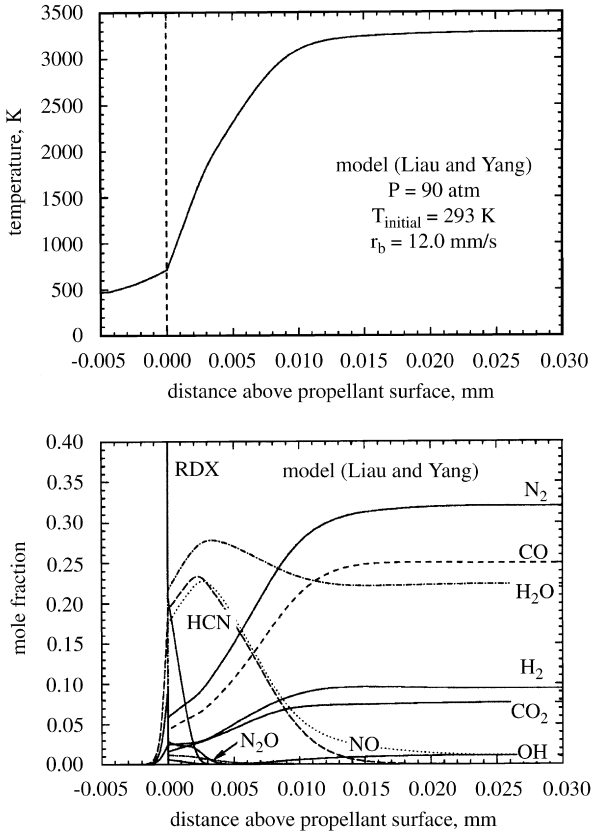

Fig. 14. Distributions of temperature and major species concentrations of self-sustained combustion of RDX at 90 atm [6].

oxidization which includes the formation of NO and H_2O and the removal of NO_2, and (3) second-stage oxidization which includes the conversion of HCN and NO to the final products such as CO, N_2, and H_2. Efforts were also made to model the self-deflagration of ADN [94,96]. Fig. 16 shows the good agreement between the calculated species profiles and experimental data [137]. The condensed-phase process was not included due to the lack of a reliable kinetic mechanism. A measured surface composition of species was used as an input for the gas-phase analysis.

Table 14 lists the concentrations of species entering the gas phase in different monopropellant combustion models, including RDX (nitramine), NG (nitrate ester), GAP (azide), AP, and ADN. The data is primarily based on experimental measurements. The largest concentration is in bold and concentrations of 0.2 or greater are in italics. The near-surface gas-phase reactions, which depend on the species concentrations and reactivity, dictate the gas-phase heat feedback, and subsequently the

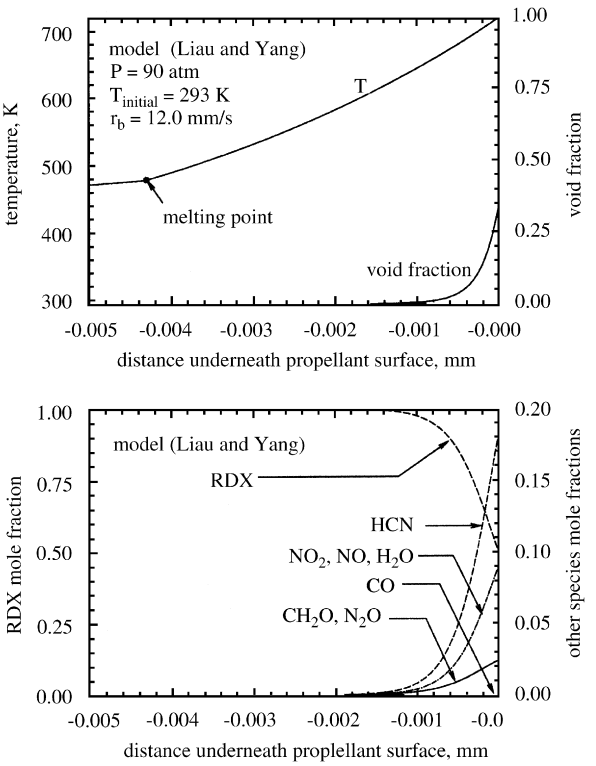

Fig. 15. Close-up view of temperature and species–concentration profiles in subsurface region of self-sustained combustion of RDX at 90 atm [6].

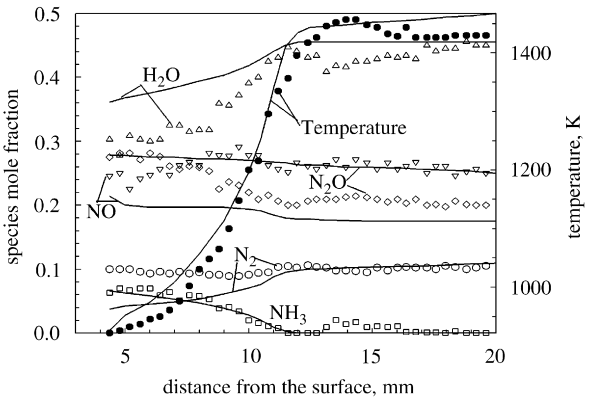

Fig. 16. Calculated [96] temperature and species concentration profiles of ADN gas flame at 6 atm compared with experimental data [137].

burning rate. AP has a large concentration of reactive species close to the surface, enabling a high heat feedback in spite of the low flame temperature (~1400 K).

Fig. 17 shows the calculated temperature profiles for AP at 0.6 atm and RDX, GAP, and BTTN at 5 atm. The secondary flame for BTTN is not shown in the figure. In comparison with other ingredients, GAP has a lower calculated flame temperature, which is consistent with experimental data. Fig. 18 shows the calculated temperature profiles for BTTN at three different pressures [92]. A dark-zone temperature plateau is clearly observed. A secondary flame exists at the end of the dark zone and the temperature rises to an equilibrium value greater than 3000 K. The length of the dark zone decreases with increasing pressure, a phenomenon consistent with the trend observed in experiments [133]. Fig. 19 shows the calculated gas-phase temperature profiles for NG, BTTN, and TMETN [92]. The large heat feedback from the gas phase for NG results from the shorter primary-flame standoff distance and the higher primary flame temperature. Thus, even though BTTN has a slightly higher flame temperature (or energy content) than NG, the former exhibits a lower burning rate. The temperature gradients in the condensed-phase (not shown in figure) also follow the order of NG > BTTN > TMETN. The temperature plateau in the NG flame starts closer to the surface than its counterparts for BTTN and TMETN, and also exhibits a flatter profile throughout the dark zone. Due to the presence of the temperature plateau, the heat release in the secondary flame zone has limited influence (except through radiation) on the gas-phase heat feedback at the burning surface and the resultant burning rate. The surface temperatures are similar for all three monopropellants considered herein.

The dark-zone temperature plateau in a solid-propellant flame is caused by a combined effect of fluid transport and high activation energies of reactions of some intermediate species, such as NO, CO, and HCN [99]. These species need a period of residence time before they can undergo vigorous exothermic reactions to form final equilibrium products (H_2O, N_2, CO_2, CO, etc.). Reaction rates in the gas phase increase with pressure, and consequently the dark zone shortens and eventually disappears at sufficiently high pressures. Nitrate esters (NG, BTTN, and TMETN) and ADN have large concentrations of NO_2 and/or N_2O at the burning surface, which react further to, form NO. The ADN flame exhibits two separate dark-zone temperature plateaus [10,94,96]. The first (800–1200 K) occurs in the range of 5–20 atm, due to the inhibition effect of NO in the reaction system of NH_3 and NO_2. The second (1200–1600 K) results from the low reactivity and high activation energies

Table 14
Mole fractions of species at the propellant burning surface (5 atm)

Monopropellant	Nitrogen-containing species						Carbon species		Other species			
	N_2	NO	HCN	NH_3	NO_2	N_2O	CO	CH_2O	O_2	H_2O	$HClO_4$	Other
RDX [17]		0.08	0.17		0.08	0.08		0.08		0.08		**RDX(g)—0.4**
AP [93]				*0.26*		0.05			0.12	0.17	*0.21*	HCl—0.09
GAP(89.6%) [11]	**0.18**		0.15	0.03			0.11	0.03		0.06		**C(s)—0.18**
												CH_4—0.1, H_2—0.08
ADN [94]	0.1	*0.23*		0.07		*0.28*				*0.3*		*HNO_3—0.2*
NG-Hatch [16]					*0.5*			*0.33*				HCO—0.17
NG-Levy [16]					*0.33*		0.17	*0.33*				HONO—0.17
NG-MSM4 [16]							0.17					*HONO—0.5, HCO—0.33*

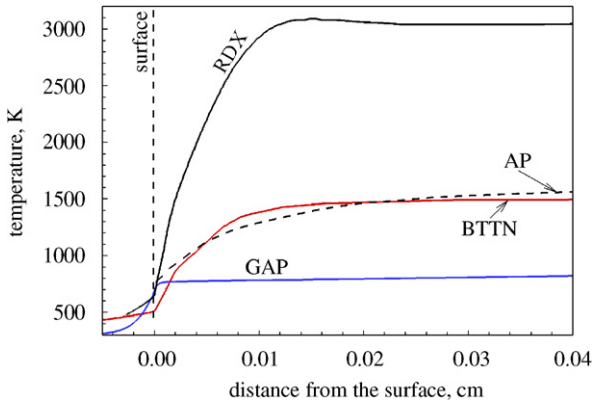

Fig. 17. Calculated temperature profiles of RDX [17], BTTN [92], AP [93], and GAP [11] monopropellants.

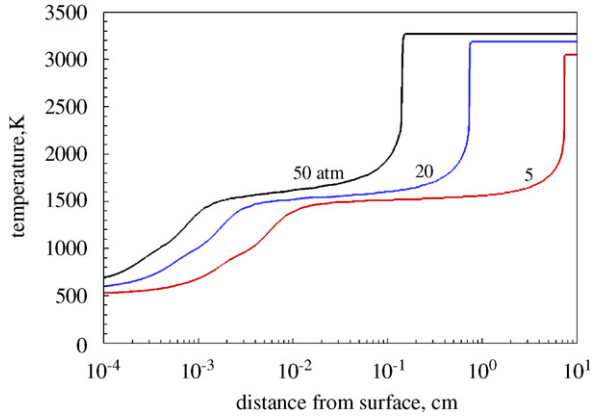

Fig. 18. Calculated temperature profiles of BTTN at three different pressures [92].

of reactions involving NO and N_2O [10]. Even though the elemental composition of RDX ($C_3H_6N_6O_6$) is similar to NG ($C_3H_5N_3O_9$) and BTTN ($C_4H_7N_3O_9$), a dark zone is not observed in the case of RDX self-deflagration. The situation,

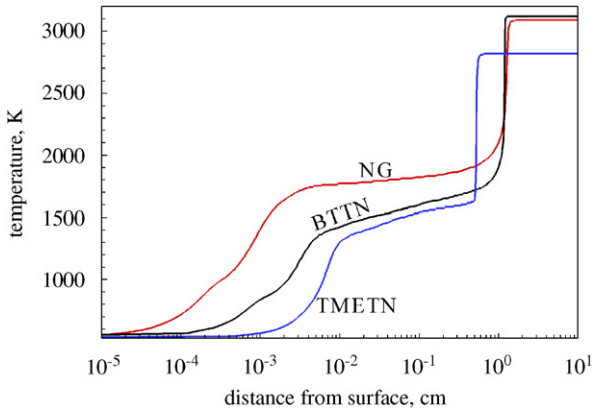

Fig. 19. Calculated temperature profiles [92] of nitrate esters showing dark-zone temperature plateaus at 10 atm.

however, becomes different under externally impressed radiative flux. Fig. 20 shows laser-assisted RDX combustion [120] at near-atmospheric pressures. A dark zone is clearly present and can be accurately modeled [17,21]. The existence of a dark-zone temperature plateau in the laser-assisted case is attributed to the enhanced transport effect near the propellant surface on account of increased burning rate (due to the laser heat flux) and dominance of the endothermic pathway producing HCN. The calculated dark-zone length increases with increasing laser flux [112]. A comprehensive discussion of this subject was recently presented by Yang et al. [99].

Fig. 21 shows the predicted and measured dark-zone lengths for NG [168,176,177], BTTN [133], and TMETN [133] at different pressures. Owing to the lack of data for pure NG, some double base (NG/NC) propellant results are included. The predicted values for NG show good agreement with the wide range of experimental data. The measured

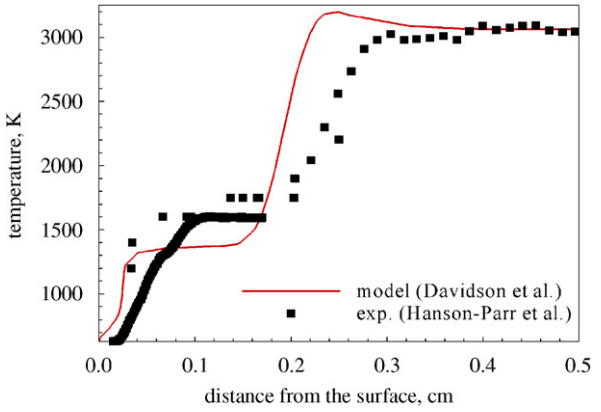

Fig. 20. Calculated [17] and measured [120] temperature profiles of RDX at 1 atm under laser-assisted combustion.

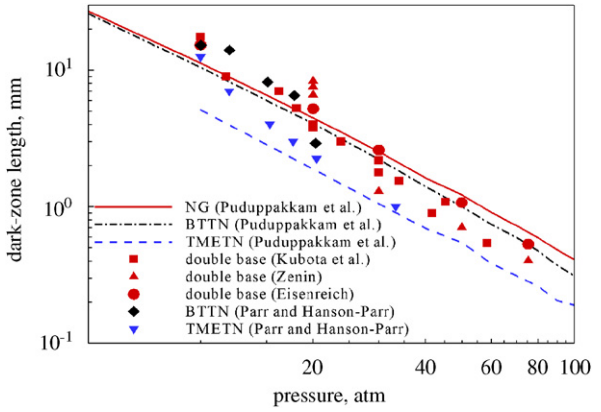

Fig. 21. Calculated [92] and measured [133,168,176,177] dark-zone lengths of nitrate ester as function of pressure.

dark-zone length for TMETN is lower than that for BTTN and the double base propellants. The dark-zone thickness can be correlated with pressure in the following form:

$$L_d = ap^d, \tag{55}$$

where the pressure exponent, d, has a negative value, which is consistent with the fact that the dark-zone length decreases with increasing pressure. Eq. (55) does not hold for very low pressures, since $L_d \to \infty$ as $p \to 0$. The calculated d (~ -1.7) is in good agreement with experimental values of -1.8 [168,178] and -2.2 [168].

The surface temperature signifies the commencement of the gas-phase process, and thus matching the calculated value with experimental data provides a good validation of the model. Fig. 22 shows

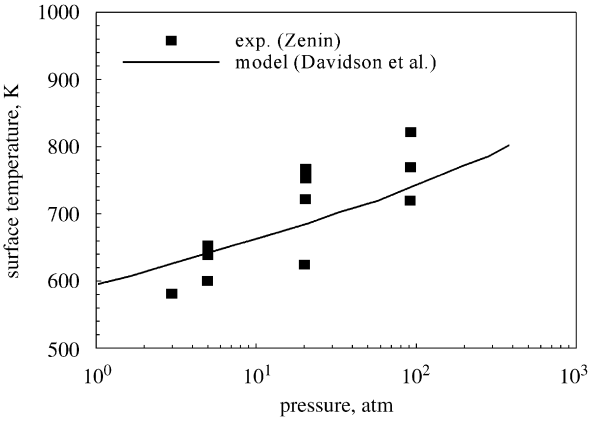

Fig. 22. Comparison between calculated [17] and measured [15] surface temperatures of RDX monopropellant combustion.

good agreement between measured and calculated surface temperatures for RDX [17]. It is worth noting that making a precise measurement of the burning-surface temperature is a formidable task, due to uncertainties in locating the surface, across which rapid property variations occur. In addition to the propellant surface temperatures, the adiabatic flame temperature provides another test for the employed gas-phase reaction mechanisms. In general, the models predict the equilibrium flame temperatures well, with the exception of GAP. The experimental flame temperatures of GAP are $\sim$1100 K, while equilibrium value is $\sim$1400 K. The discrepancy apparently arises from the fuel-rich character of GAP, which results in the formation of non-equilibrium, carbonaceous residue.

7.5.2. Combustion of mixtures of propellant ingredients

Mixtures of propellant ingredients may exhibit combustion characteristics distinct from those of the constituent monopropellants. One major factor contributing to this phenomenon is the difference in chemical kinetics that affects the spatial distribution of energy release. The heat released in the condensed phase and the species concentrations at the propellant surface depends on the employed material composition. This section presents the modeling results of binary and ternary mixtures of propellant ingredients.

7.5.2.1. Binary pseudo-propellants. As a logical step towards the modeling of an operational propellant, binary systems such as RDX/GAP [23,100], HMX/GAP [20], and AP/HTPB [101] have been modeled.

Fig. 23 shows schematically the combustion-wave structure of HMX/GAP pseudo-propellant [20]. In the solid-phase region, HMX powder and GAP are physically mixed. The former melts at 558 K with negligible chemical reactions, due to the low temperature and short residence time. Thermal decomposition and phase change of HMX occurs in the liquid phase to form a subsurface two-phase layer (i.e., foam layer). The propellant surface ($x = 0$) is defined herein as the interface between the foam layer and the gas-phase region, at which rapid gasification of HMX prevails. Since the surface temperature of HMX/GAP pseudo-propellant (~700 K) is lower than that of pure GAP, GAP leaves the surface as aerosol surrounded by vapor HMX and its decomposed gaseous products. In this region, GAP persists as a condensed species and continues to decompose. A significant amount of carbonaceous residue may be present on the surface during combustion.

Fig. 24 shows the comparison between the measured [138] and predicted [20] burning rates of HMX/GAP at different laser intensities. Fig. 25 shows the effect of propellant composition on burning rate at various pressures without external laser heat flux. The burning rate in general decreases with the addition of GAP, which releases a substantial amount of N_2 in the near-surface region. Although the process is exothermic, the presence of N_2 and large fuel fragments dilutes the concentrations of reactive species near the surface, and consequently reduces the rate of energy release from HMX reactions. The heat feedback to the surface decreases accordingly, rendering a lower burning rate. Another factor contributing to this phenomenon is the blowing effect of the GAP compound, which tends to push the primary flame away from the surface. The situation is, however, different at high pressures. The burning rate of HMX/GAP pseudo-propellant with a mass ratio of 9:1 is greater than that of pure HMX for $p > 30$ atm. The effects of laser heat flux and pressure on the burning rate of HMX/GAP pseudo-propellant

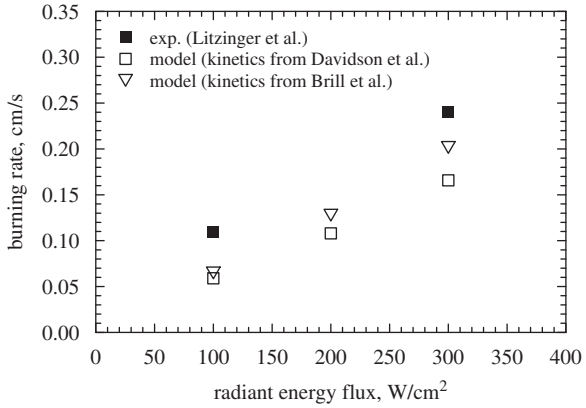

Fig. 24. Comparison between calculated [20] and measured [138] burning rate of HMX/GAP (mass ratio of 8:2) at 1 atm.

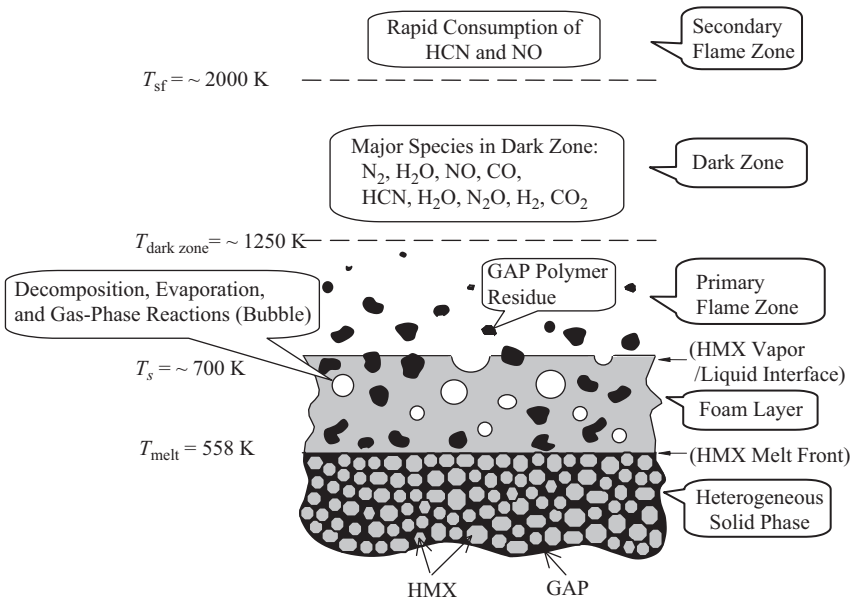

Fig. 23. Combustion-wave structure of HMX/GAP propellant at 1 atm [20].

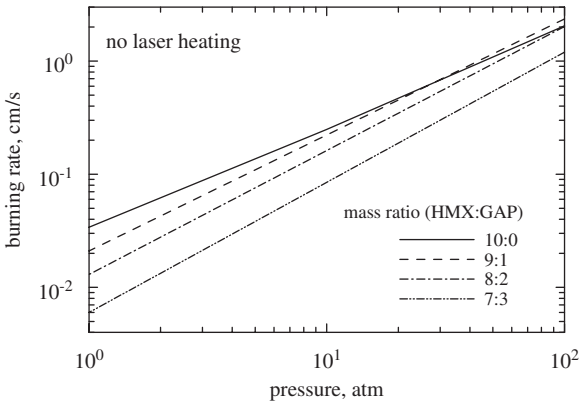

Fig. 25. Effect of composition on burning rate of HMX/GAP pesudo-propellant at various pressures; self-sustained combustion [20].

(80/20) have also been studied [20]. The impressed laser flux causes a substantial increase in burning rate at low pressures (e.g., 1 and 10 atm). The effect, however, diminishes at high pressure, since the heat feedback from the gas phase overshadows the surface laser absorption in determining the energy balance at the surface. The heat transfer to the burning surface increases almost linearly with pressure.

The flame structure of HMX/GAP pseudo-propellant observed in experiments using TQMS [138] was reasonably well predicted by Kim et al. [20]. Fig. 26 shows the predicted and measured species concentration profiles in the gas phase at 1 atm with a laser intensity of 100 W/cm^2. The temperature rises rapidly from 677 K at the surface followed by a dark-zone temperature plateau in the range of 1200–1600 K, and further increases to its final value of 2780 K. The concentrations of HCN, NO, and H_2O in the dark zone appear to be similar to those of pure nitramines. A rapid conversion of HCN and NO to N_2 and CO occurs in the secondary flame zone. The predicted flame standoff distance of 3 mm is slightly shorter than the measured value of 4 mm, partly due to the ambiguity in defining the propellant surface during experiments. Fig. 27 shows a close-up view of the primary flame of HMX/GAP pseudo-propellant immediately above the propellant surface, which extends over a length of 100 μm. The dominant reactions in this oxidation stage are listed as (R.22), (R.23) and (R.27) in Table 9. The prediction of N_2O concentration was satisfactory as compared with the measurement [138]; however, NO_2 and CH_2O appear to be consumed too fast. Intermediate reactions forming CH_2O and NO_2 are still lacking in the near-surface region in order to yield better agreement with experimental results. Conversion of GAP and GAP* to N_2, HCN, CO, NH_3, CH_2O, CH_3CHO, H_2O, C_2H_3CHO, C_2H_4, CH_3CHNH, and $CH_2CHCHNH$ occurs over a very short distance (~10 μm). The decomposed fuel fragments, such as CH_2CHO, C_2H_3CHO, CH_3CHNH, and $CH_2CHCHNH$, further react to form CH_3, HCO, C_2H_3, and H_2CN. Fig. 28 shows the predicted [20] species concentration and temperature profiles in the foam layer. An appreciable amount of HMX evaporates to form gas bubbles in this region, but the extent of decomposition through the pathways (R.22) and (R.23) in the condensed phase appears to be limited. On the other hand, most of the GAP compound is consumed to become GAP* and N_2, releasing heat to support pyrolysis in the condensed phase. Further decomposition of GAP* according to (R.24), however, is constrained due to the low-temperature condition. The predicted surface temperature and foam-layer thickness are 677 K and 30 μm, respectively.

Fig. 29 shows the RDX/GAP pseudo-propellant burning rate as a function of composition, calculated from two different models [23,100]. The experimental data [104] is also included for comparison. An interesting trend is noted, with both pure RDX and GAP having much higher burning rates than their mixtures. While the calculated values from Liau et al. [23] and Puduppakkam and Beckstead [100] differ, probably due to different gas-phase kinetic mechanisms and condensed phase treatments, they both show the consistent trend of decreasing burning rate with increasing GAP content over the composition range modeled. Fig. 30 shows the effects of initial composition and pressure on the burning rate of RDX/GAP pseudo-propellant [23]. The decrease in the burning rate with increasing GAP content is attributed to the decrease in the gas-phase heat feedback with increasing concentrations of inert gases such as N_2 from GAP decomposition. The condensed-phase heat release increases with the GAP content, but is apparently insufficient to counter the decrease in the gas-phase heat feedback. It is worth noting that the gas-phase mechanism used was not specifically developed for RDX/GAP, but still predicts the right trends. Fig. 31 shows the predicted [23] and measured species–concentration profiles using TQMS [138] in the gas phase at 1 atm with a laser intensity of 100 W/cm^2. Similar to the HMX/GAP

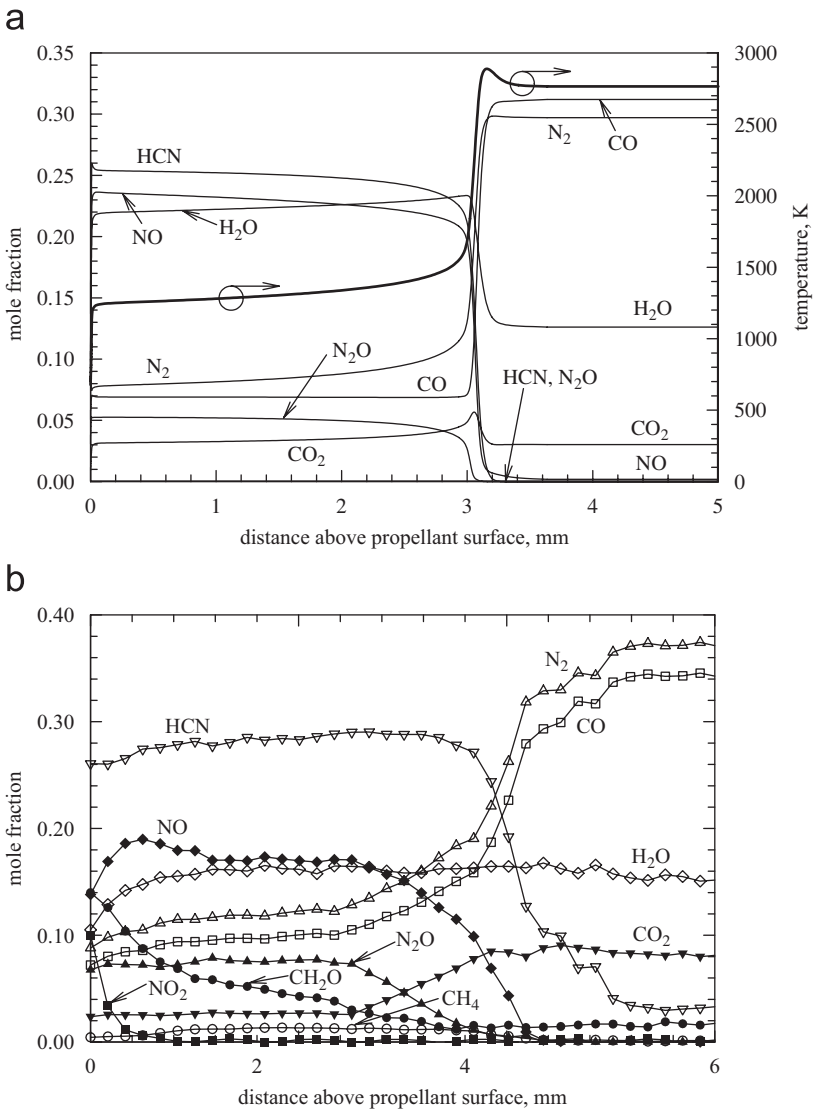

Fig. 26. (a) Calculated [20] and (b) measured [138] species–concentration profiles of the gas-phase flame of HMX/GAP pseudo-propellant (80/20) at 1 atm and laser intensity 100 W/cm^2.

combustion, HCN, NO, and H_2O are the major intermediate products in the dark zone. The conversion of HCN and NO to N_2 and CO dominates the luminous secondary flame, while the consumption of formaldehyde, NO_2, and N_2O accounts for the primary flame immediately above the burning surface. In contrast to pure RDX combustion, a noticeable amount (1–2%) of CH_3CHO is observed near the surface.

Fig. 32 shows the combustion-wave structure in the subsurface foam layer for RDX/GAP with a mass ration of 8:2. The predicted temperature [23] rises from the melting point of RDX at 478 K to around 590 K at the propellant surface. The mass fraction of liquid RDX originates at 0.8 and decreases slightly, mostly through evaporation and partially through decomposition. The void fraction increases from 0% to almost 9% due to the formation of bubbles containing vapor RDX and a small amount of decomposed gases. Consistent with the condensed-phase kinetics, the extent of GAP decomposition is negligible at temperatures lower than 600 K. The mass fraction of GAP remains at 0.2 throughout the foam layer, and then evolves into the gas phase. Fig. 33 shows the predicted temperature, void fraction, and condensed-species concentration

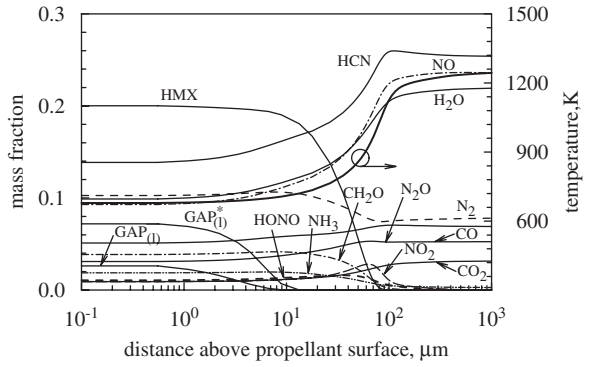

Fig. 27. Calculated [20] temperature and species–concentration profiles in near-surface region of HMX/GAP pseudo-propellant (80/20) combustion at 1 atm and laser intensity 100 W/cm^2.

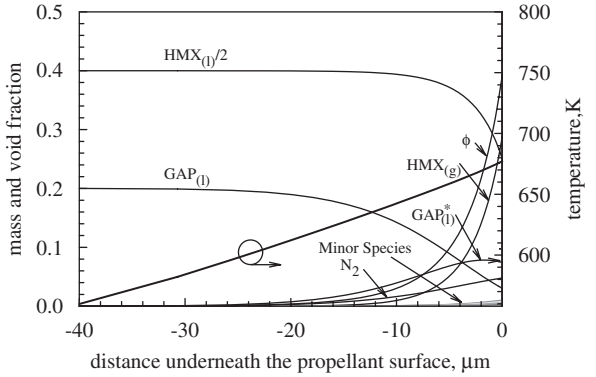

Fig. 28. Calculated [20] temperature and species–concentration profiles in subsurface region of HMX/GAP pseudo-propellant (80/20) combustion at 1 atm and laser intensity of 100 W/cm^2.

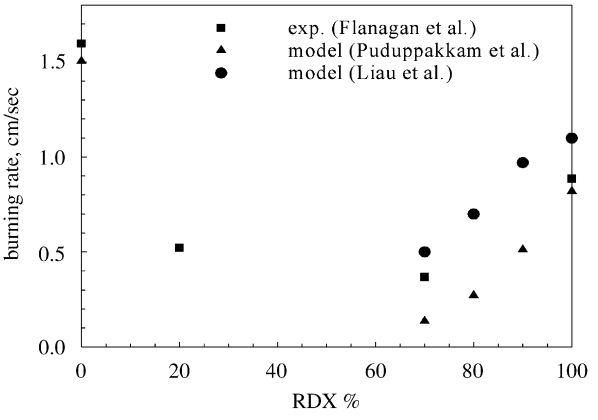

Fig. 29. Calculated [23,100] burning rates of RDX/GAP pseudo-propellants at 35 atm, compared with experimental data [104].

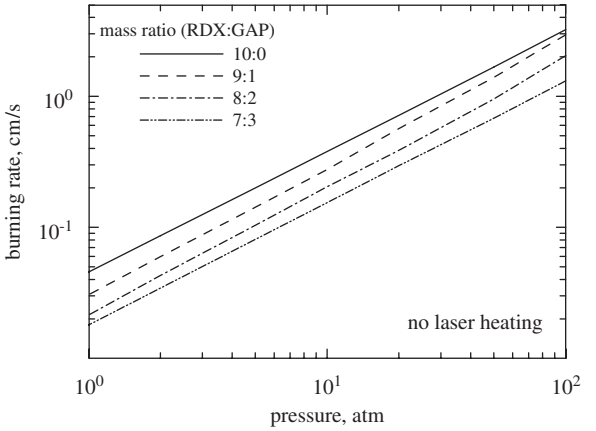

Fig. 30. Calculated burning rates of RDX/GAP pseudo-propellants as a function of mass composition at various pressures [23].

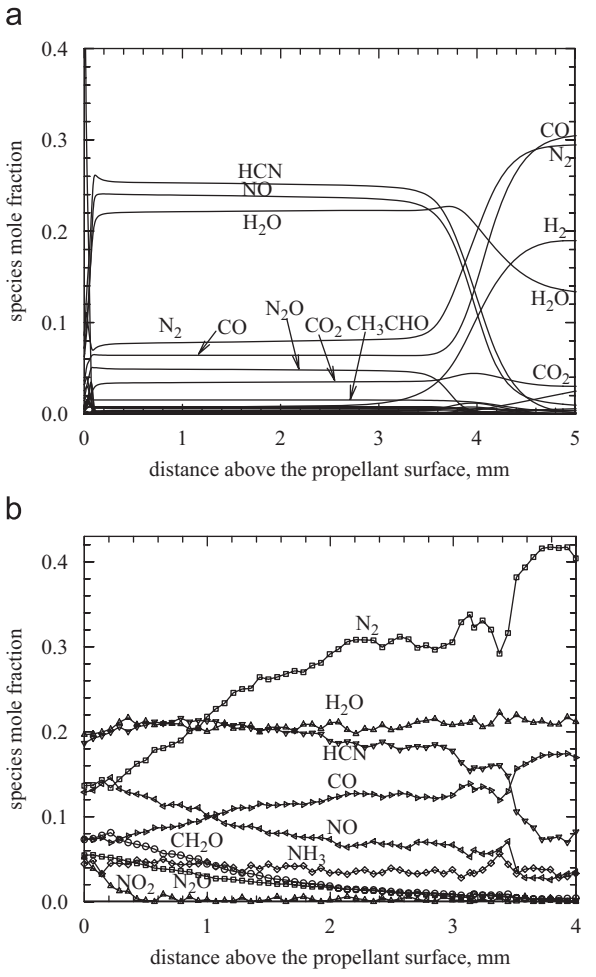

Fig. 31. (a) Calculated [23] and (b) measured [138] species–concentration profiles of the gas-phase flame of RDX/GAP pseudo-propellant (mass ratio 8:2) at 1 atm and laser intensity 100 W/cm^2.

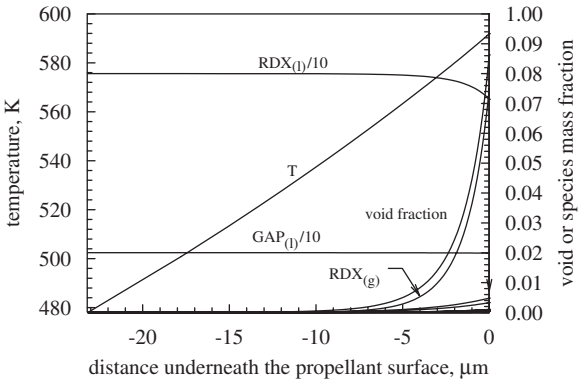

Fig. 32. Calculated flame structure in the foam layer of RDX/GAP pseudo-propellant (mass ratio 8:2) at 1 atm and laser intensity 100 W/cm^2 [23].

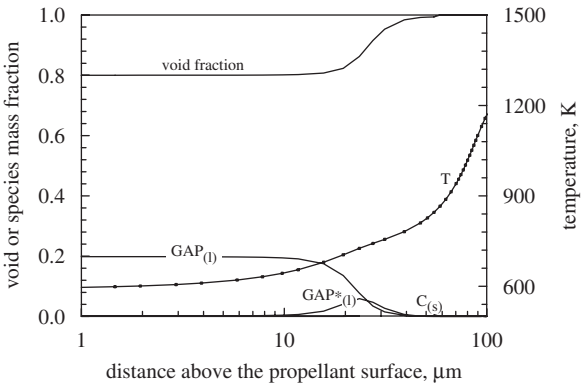

Fig. 33. Calculated temperature, void fraction, and condensed species–concentration profiles in the near surface region of RDX/GAP pseudo-propellant (mass ratio 8:2) at 1 atm and laser intensity 100 W/cm^2 [23].

profiles [23] in the region immediately above the propellant surface. The void fraction is not unity near the propellant surface, due to the fact that the condensed-phase species GAP, GAP*, and *C*(*s*) are dispersed in the gas-phase region. GAP starts to decompose in the gas phase when the temperature reaches 700 K. At this stage, GAP* forms immediately due to the elimination of N_2 (Table 9, (R.24)) and reaches its maximum concentration within a short distance (less than 4 μm).

A model for AP/HTPB pseudo-propellant combustion [101] was developed by assuming a premixed mixture of AP and HTPB. The reaction mechanism incorporates that proposed by Korobeinichev et al. [139] for AP/CTPB, the AP monopropellant mechanism, and some reaction steps from the GRI mechanism [160]. The model

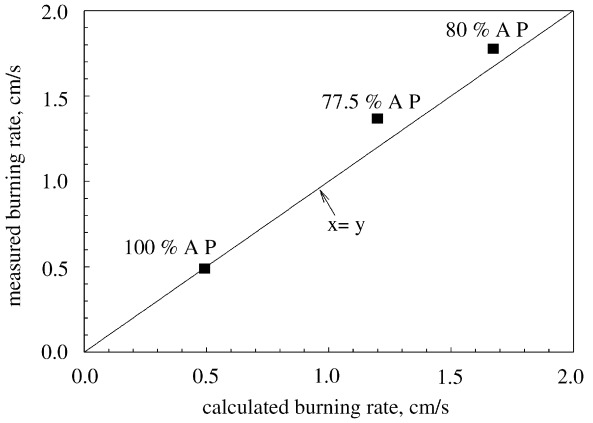

Fig. 34. Burning rate as a function of AP/HTPB composition at 34 atm: experimental data from Foster et al. [179] and Atwood et al. [117], model calculations from Jeppson et al. [101] and Jing et al. [93].

was validated against the experimental data of Foster and Miller [179] for two mixtures of 12 μm AP in an HTPB binder. As a monopropellant, AP has a moderate burning rate [117]. When combined with HTPB, which cannot self-sustain combustion as a monopropellant, the resultant mixture has a much higher burning rate [117]. Fig. 34 shows good agreement between the predicted [93,101] and measured [117,179] burning rates for different AP/HTPB compositions at 34 atm. The effect of pressure on burning rate was also examined; the result [101] and the comparison with measurements [180] are depicted in Fig. 35.

Miller and Anderson [91] modeled nitrate-ester based binary pseudo-propellants M2 and M9, as listed in Table 5. The nitrocellulose (NC) considered in the analysis was composed of three different nitration levels (mono, di, and tri). The burning rates and gas-phase temperature profiles of M2 and M9 were predicted reasonably well. In addition, the dependence of the burning rate and dark-zone temperature plateau on the detailed gas-phase chemistry was investigated. The discrepancies between measurements and predictions may be attributed to the exclusion of such trace components as stabilizer and flash suppressant in the model.

7.5.2.2. Ternary pseudo-propellants. Modeling of ternary systems has been conducted by Puduppakkam and Beckstead [102] and Yoon et al. [103] for RDX/GAP/BTTN, and by Miller and Anderson [91] for NC/NG/DEGDN (JA2). This is an important step closer to the treatment of an operational solid

propellant. In the system RDX/GAP/BTTN, RDX functions as an oxidizer, GAP a fuel, and BTTN a plasticizer. Fig. 36 shows a schematic view of the entire combustion-wave structure segmented into three distinct regions: the solid-phase, near-surface two-phase, and gas-phase regions [103]. In the solid-phase region, RDX powder, GAP, and BTTN are physically mixed. RDX melts at 478 K with negligible chemical reactions taking place. The decomposition temperature for pure BTTN is 523–773 K [134]. Thermal decomposition and phase change of RDX and BTTN occur to form a subsurface foam layer. Since the surface temperature of RDX/GAP/BTTN pseudo-propellant (~600 K) is lower than the gasification temperature of pure GAP (~1050 K), GAP leaves the surface as aerosol surrounded with the RDX and BTTN vapor and their decomposed gaseous products [103]. For simplicity, Puduppakkam and Beckstead [102] assumed that GAP decomposes completely in the condensed phase, where as in the model of Yoon et al. [103] the decomposition of GAP in the gas phase was included.

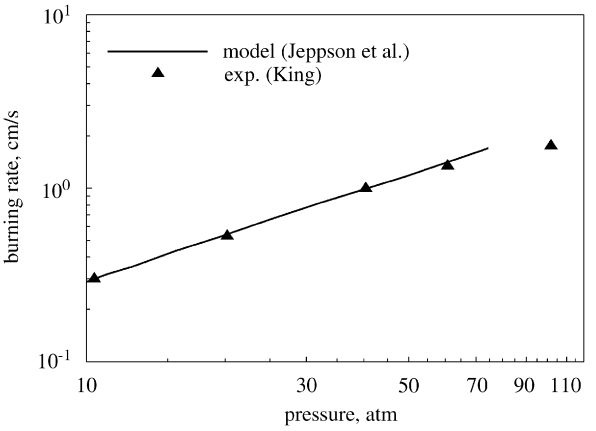

Fig. 35. Comparison of calculated [101] and measured [180] burning rate for AP/HTPB (73:27).

Parr and Hanson-Parr conducted detailed flame-structure measurements of a pseudo-propellant consisting of 70% RDX, 9% GAP, and 21% BTTN [107]. BTTN was added to the formulation, since a pure RDX/GAP mixture produced solid carbonaceous material prohibiting the implementation of laser diagnostic techniques. Fig. 37 shows the calculated and measured burning rates over the

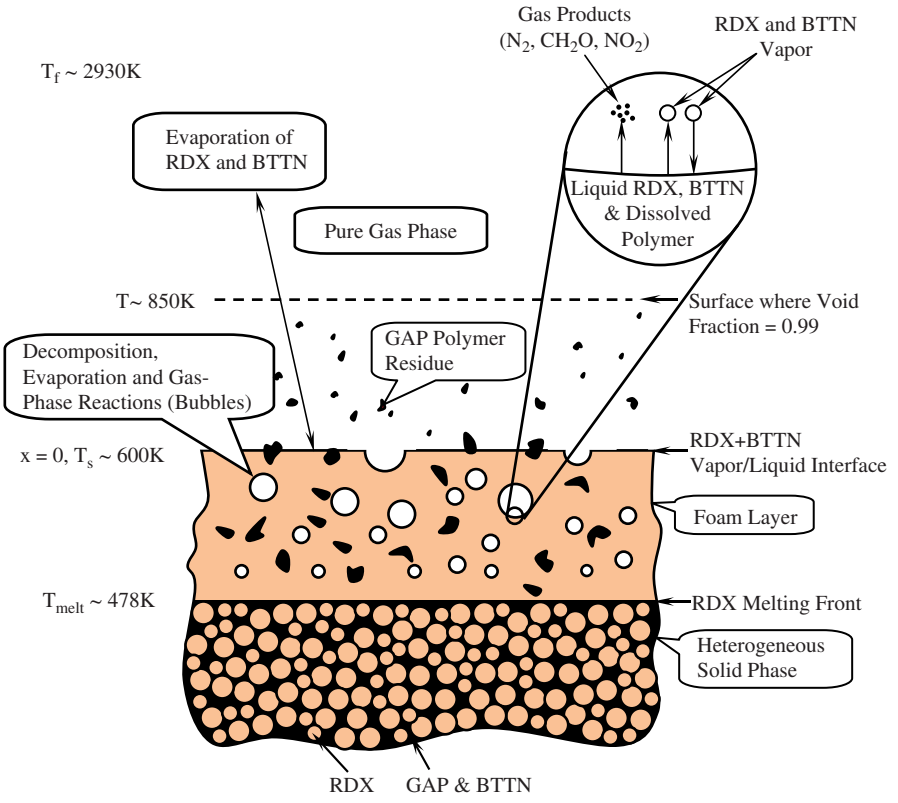

Fig. 36. Combustion-wave structure of RDX/GAP/BTTN pseudo-propellant at 1 atm (not to scale) [103].

pressure range of 1–100 atm. The pressure exponent is about 0.8. It is worth noting that the modeling results reported in Refs. [102,103] were blind predictions, wherein the chemical kinetics for each of RDX, GAP, and BTTN were combined to simulate the combustion of a ternary pseudo-propellant. None of the parameters in the reaction mechanisms were varied when extending from monopropellant to pseudo-propellant calculations. Fig. 38 presents the calculated burning rates for various propellant ingredients and their mixtures. The burning rates of the pseudo-propellants are less than those of the constituting ingredients. Fig. 39 compares the calculated temperature profiles for pseudo-propellants RDX/GAP/BTTN at 5 atm [102], RDX/GAP at 5 atm [23] and AP/HTPB at 0.6 atm [101]. The addition of BTTN to RDX/GAP leads to more heat release close to the surface, and consequently increases the burning rate.

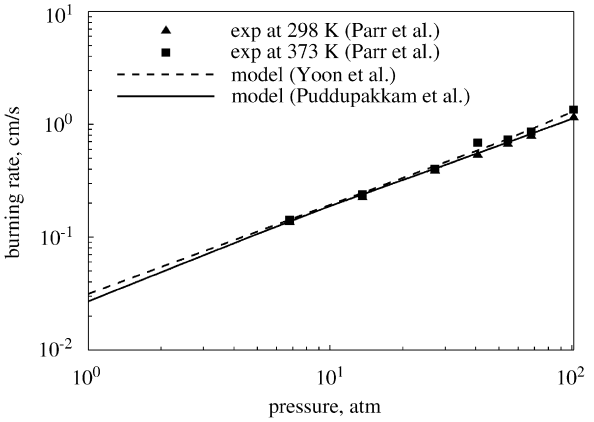

Fig. 37. Calculated [102,103] and measured [210] burning rates of RDX/GAP/BTTN pseudo-propellant (mass ratio 71:9:20) over the pressure range of 1–100 atm.

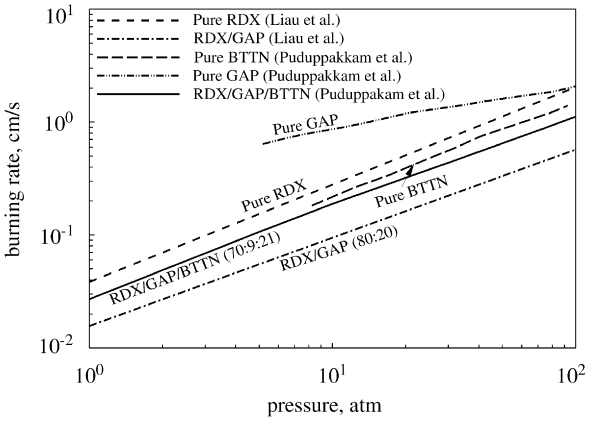

Fig. 38. Calculated [6,11,23,92,102] burning rates of mono- and pseudo-propellants as function of pressure.

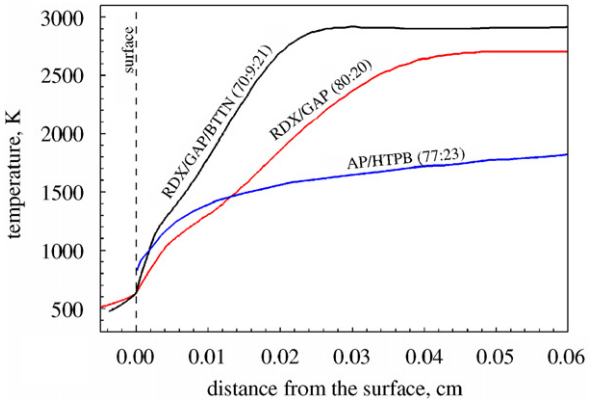

Fig. 39. Calculated temperature profiles of RDX/GAP/BTTN (5 atm) [102], RDX/GAP (5 atm) [23] and AP/HTPB (0.6 atm) [101] pseudo-propellant combustion.

The predictions for the burning characteristics and flame structures of the various propellant ingredients and their mixtures considered herein appear to be encouraging. The reaction mechanisms seem consistent, suggesting that a general framework can possibly be developed representing the chemical pathways of different compounds and their resultant mixtures. This could be a significant step towards a more detailed and accurate predictions of combustion characteristics. While quantitative results may not always be accurate, the models typically result in the right trends, which help to explain the combustion process.

8. Ignition of solid propellants

8.1. Simple ignition models

Ignition of solid propellants involves an array of intricate physiochemical processes under energetic stimuli, and has been the subject of extensive research since 1950. A comprehensive review of the early work was conducted by Price et al. in 1966 [181]. The experimental and theoretical literature pertaining to the ignition of solid propellants over the period of 1966 through 1980 was reviewed by Kulkarni et al. [182] and Hermance [183]. The state of understanding in Russia up to 1989 was presented by Vilyunov and Zarko [184], giving a detailed examination of the various ignition models and related experimental approaches. More recently, a review of laser and radiative ignition of

24 solid energetic materials, with emphasis on work performed in the Former Soviet Union, was provided by Strakouskiy et al. [185].

Liau et al. [21] compiled various simple models that have been developed to study the ignition of solid propellants and explosives. The result is summarized in Table 15, adopted from Ref. [21]. Within the context of those simple models, ignition can be broadly classified into three categories: solid-phase (or reactive solid), heterogeneous, and gas-phase reaction models. A single-step Arrhenius type of reaction is used in the above models. The solid-phase reaction models [186–189] assume that exothermic reactions in the condensed phase are the dominant mechanism of ignition, while the effects of surface and gas-phase processes are secondary and can be neglected. The formulation usually includes the energy equation for the condensed phase. The convection terms are often ignored for simplicity. Ignition criteria are defined based on conditions at which thermal run-away or steady-state combustion takes place. Primary results include: (1) ignition delays as functions of condensed-phase reaction parameters, external heat flux, ambient pressure, and propellant preconditioned temperature, among others; and (2) evolution of the temperature field in the regime of interest. Due to the basic assumptions employed, this type of model is suitable for materials in which condensed-phase heat release represents the rate-controlling step in determining the propellant burning behavior. The pressure dependence of ignition delay, however, is commonly under-estimated since the condensed-phase process is insensitive to pressure [21].

Heterogeneous reaction models [190–198] assume that heterogeneous reactions at the propellant surface are responsible for ignition due to the molecular diffusion of ambient oxidizer species to the propellant surface. The formulation takes into account the condensed-phase conservation equations of energy and species concentration along with interfacial boundary conditions. A number of ignition criteria, such as go/no-go, pre-specified flame and surface temperatures, and temperature gradient, have been used. Results indicate that the activation energies of surface heterogeneous reactions have strong influences on the ignition delay and temperature evolution in the condensed phase.

Unlike the previous two categories, the gas-phase reaction models [199–206] presume that exothermic gas-phase reactions and their heat feedback to the propellant surface are the primary mechanism of ignition. Conservation of energy and species concentration in the gas phase is of major concern, but the condensed-phase equations are also included for completeness. In addition to the commonly used ignition criteria, emission of light and achievement of steady-state combustion are employed in some studies. Results typically include ignition delay as a function of surface condition for shock-tube cases or heat flux and pressure for radiant cases. In spite of their contributions in correlating experimental data and providing qualitative understanding of ignition behavior, all the above models [186–206] are semi-empirical in nature and do not provide predictive capability at scales sufficient to resolve the detailed ignition mechanisms and flame evolution.

8.2. *Ignition models based on detailed chemical kinetics*

Liau et al. [21,111] extended the detailed steady-state combustion model for RDX, described in Refs. [6,18], to include the transient development for RDX and HMX. Similarly, Meredith and Beckstead [112] described the ignition process of HMX by extending a previously-developed steady-state model [7]. The models are capable of treating the entire ignition process from surface pyrolysis to steady-state combustion, with the instantaneous burning rate and surface conditions treated as part of the solution. Table 7 describes the subsurface two-phase and the gas-phase kinetics models employed by Liau et al. [111] for ignition of nitramine monopropellants. No condensed-phase reactions were taken into account in the case of HMX ignition .

Fig. 40 illustrates schematically the physiochemical processes involved in the laser-induced ignition of a strand of nitramine monopropellant [21]. The propellant and the ambient gas are initially at room temperature. Once the laser is activated, volumetric absorption of laser energy in the solid phase takes place, as shown in Fig. 40a. In the gas phase, only certain gaseous species, such as vapor RDX, absorb a noticeable amount of laser energy and the gas-phase absorption is negligible during the inert heating period. When the solid reaches its melting temperature, the absorbed radiant energy can not further raise the temperature without first melting the solid. Since the radiant energy absorbed is insufficient for instantaneous melting of the entire

Table 15
Theoretical models of solid-propellant ignition, adopted from Ref. [21]

Solid-phase reaction model	Heterogeneous reaction model	Gas-phase reaction model
Presumption		
Solid-phase reactions cause ignition	Heterogeneous reactions at surface cause ignition	Gas-phase reactions cause ignition
Primary concern		
Condensed phase	Condensed phase and interface	Gas phase and condensed phase
Formulation		
Energy equation for condensed phase Species equations for condensed phase (optional) Convection terms are usually neglected in analytical approach	Energy equation for condensed phase Species equations for condensed phase (optional) Convection terms are usually neglected in analytical approach	Energy equations for both phases Species equations for gas phase Species equations for condensed phase (optional) In-depth radiation absorption is usually neglected
Approach		
Asymptotic method Numerical method	Laplace transform Local similarity Asymptotic method Classical thermal theory Numerical method	Numerical method Asymptotic method
Ignition criteria		
Go/No-Go $T/T_{ref} \to \infty$ Steady-state combustion	Go/No-Go $T/T_{ref} \to \infty$ $dt/dT_s \to 0$ or $dT_s/dt \to \infty$ T_s rises to specified value	$T/T_{ref} \to \infty$ T_s, dT_s/dx, Y_i, or gas reaction rate (RR) rises to specified values Emission of light Steady-state combustion
Major results		
Ignition delay as function of rate constant, heat flux, pressure, and others $T(x, t)$ in the solid	Ignition delay as function of surface reaction rate and oxidizer concentration $T(x, t)$ in the solid and surface conditions	Ignition delay as function of surface condition for shock tube; or heat flux and pressure for laser $T(x, t)$ in both phases and $Y_i(x, t)$ in gas phase
References		
[186–189]	[190–198]	[199–206]
Remarks		
Suitable for condensed-phase controlled materials, such as double-based propellants Effect of pressure is under-estimated since condensed-phase process is insensitive to pressure	Suitable for the surface-reaction controlled material, such as polymers, hypergolic systems, etc. Effect of surface reaction is over-estimated for solid propellants, especially for homogeneous propellants Surface reaction with lowest activation energy dominates ignition	Suitable for gas-phase controlled material, such as low vulnerability ammunition (LOVA) propellants Detailed chemistry is established and ready to be employed in the model

solid in a short period, partial melting of the solid occurs, which leads to the formation of a mushy zone consisting of both solid and liquid (Fig. 40b). After a layer of pure liquid is formed, the solid-liquid interface starts to move, due to conductive and radiative heat transfer (Fig. 40c). In the liquid, thermal decomposition and subsequent reactions, as well as phase transition, take place, generating gas

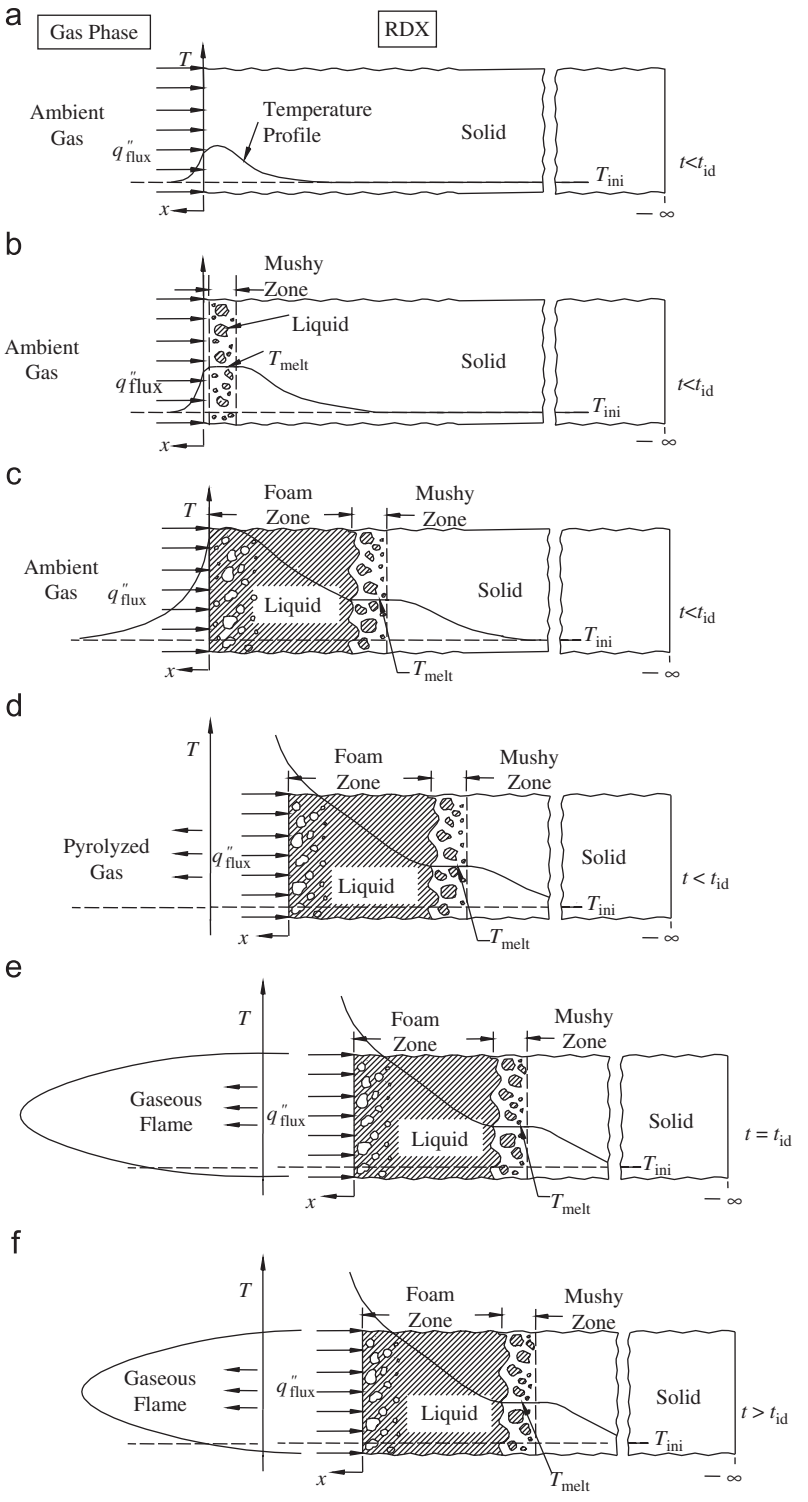

Fig. 40. Physiochemical processes involved in laser-induced ignition of RDX [21].

bubbles and forming a two-phase region. The propellant then undergoes a rapid evaporation at the surface (Fig. 40d). Ignition occurs if the heat flux is sufficiently large to initiate the subsequent self-accelerated exothermic reactions which result in substantial heat release in the gas phase and

emission of light. A luminous flame is produced (Fig. 40e) which regresses towards the surface, and finally reaches a stationary position (Fig. 40f) corresponding to its steady-state condition.

Fig. 41 shows the predicted temporal evolution of the temperature field for RDX monopropellant in argon [21] under an incident laser heat flux of 400 W/cm^2 at 1 atm and a preconditioned temperature of 300 K. The surface temperature rapidly increases to 475 K within 1 ms, due to the high intensity of the laser heat flux. The profiles for $t<1$ ms represent inert heating of the thin surface layer with conductive heat losses to both the solid- and gas-phase regions. The temperature rise in the gas phase at $t=2$ ms primarily results from radiant energy absorption rather than exothermic reactions, because the extent of RDX decomposition in the gas phase is very limited at this stage of the event. At $t=2.9$ ms, exothermic gas-phase reactions start to occur, and a flame appears near the propellant surface at $t=3$ ms. During the time period between 3 and 6 ms, the temperature continues to increase to around 1500 K, as a consequence of the heat release by exothermic reactions. As time further elapses, a luminous flame appears, and the temperature rises to its adiabatic flame temperature. The luminous flame is not stationary but regresses toward the surface. There is a time lag (about 4 ms) between the first appearances of the primary and secondary flames.

Fig. 42 shows the predicted temperature evolution for HMX monopropellant in air [111] under an incident laser heat flux of 400 W/cm^2 at 1 atm and a preconditioned temperature of 300 K. The processes leading to the ignition of HMX are similar to those observed in the case of RDX. For HMX, there is a longer time lag (~6 ms) between the first occurrence of the primary flame (~9 ms) and the secondary flame (~15 ms). It is worth noting that a dark-zone temperature plateau (~1500 K) exists in the laser-assisted combustion of RDX and HMX, while the presence of such a plateau is not evident in self-sustained combustion [6].

Figs. 43 and 44 show close-up views of the temperature evolution in the condensed phase underneath the propellant surface for RDX and HMX monopropellants, respectively. The transient development of thermal-wave penetration into the subsurface region is clearly observed. In Fig. 43, the phase transition from solid to liquid RDX is indicated by the distinct change in the temperature gradient at $T_{melt}=478$ K. Similarly in Fig. 44, the HMX phase transitions from the β to δ state and then from the δ to liquid state are indicated by the discontinuities in the temperature gradient at $T=460$ K and $T_{melt}=553$ K, respectively. The relatively flat profiles in liquid HMX compared to the β and δ phases can be attributed to the higher liquid thermal conductivity [7]. The slightly negative temperature gradient at 17 ms near the surface is an indication of the 'overdriven' state of the system, wherein the in-depth laser energy absorbed in the condensed phase exceeds the energy transfer from the decomposing HMX.

Fig. 45 shows the first appearance of the primary flame at $t=4$ ms. The RDX decomposition products, especially CH_2O and NO_2, undergo rapid reactions, which lead to the formation of NO, HCN, H_2O, CO, and N_2O in the flame. The temperature increases to about 1400 K. The species

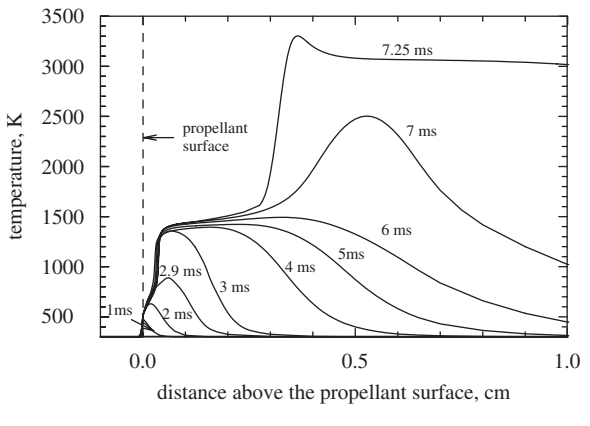

Fig. 41. Evolution of temperature field during laser-induced ignition of RDX in argon at $p=1$ atm and $\dot{Q}''_{laser}=400$ W/cm^2 [21].

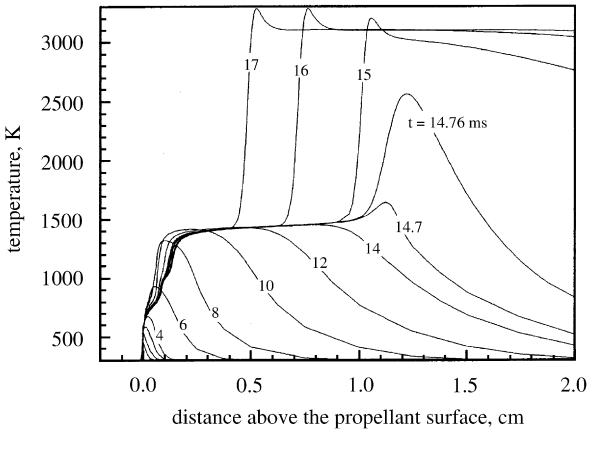

Fig. 42. Evolution of temperature field during laser-induced ignition of HMX in air at $p=1$ atm and $\dot{Q}''_{laser}=400$ W/cm^2 [111].

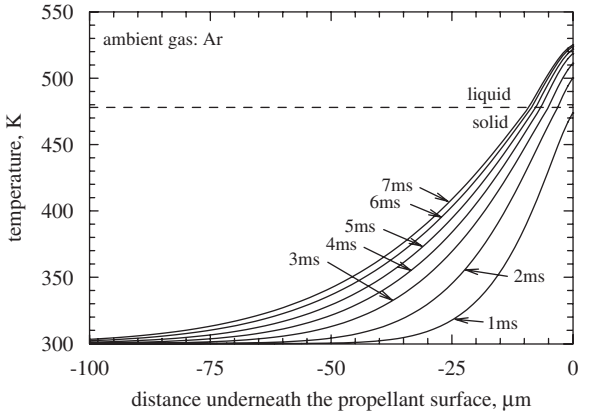

Fig. 43. Close-up view of temperature evolution in subsurface region during laser-induced ignition of RDX at $p = 1$ atm and $\dot{Q}''_{laser} = 400\,\mathrm{W/cm^2}$ [21].

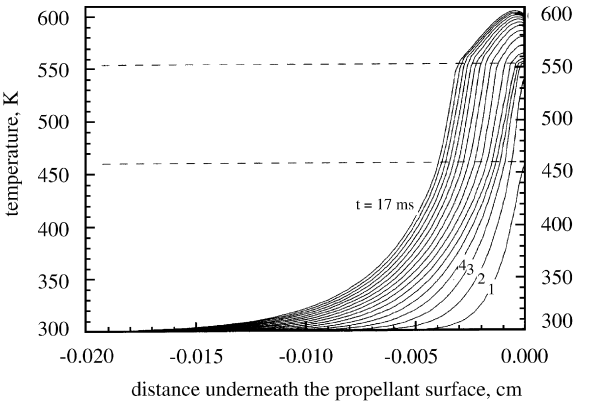

Fig. 44. Close-up view of temperature evolution in subsurface region during laser-induced ignition of HMX in air at $p = 1$ atm and $\dot{Q}''_{laser} = 400\,\mathrm{W/cm^2}$ [111].

formed in the primary flame are relatively stable due to the high activation energies of their associated reactions, and require a finite time to oxidize further. Figs. 46 and 47 show the development of the secondary flame at $t = 7$ and 7.25 ms, respectively. The temperature increases from 1500 to 3000 K at this stage and a secondary flame is established. The conversion of HCN and NO to the final products seems to be the dominant net reaction in the secondary flame. Once the secondary flame appears, the intense energy release and heat transfer in the gas phase cause the flame to regress toward the propellant surface.

The overall ignition process for nitramine propellants can be divided into five distinct stages:

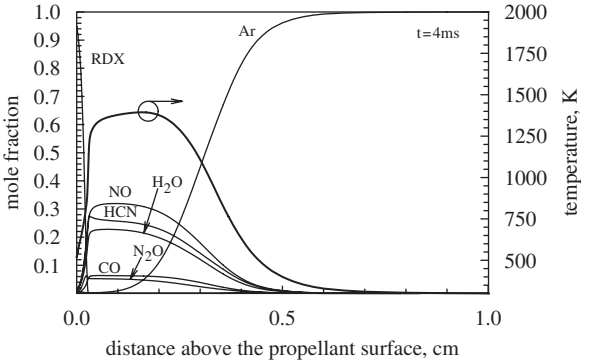

Fig. 45. Temperature and species–concentration profiles in gas phase for laser-induced ignition of RDX at $t = 4$ ms [21].

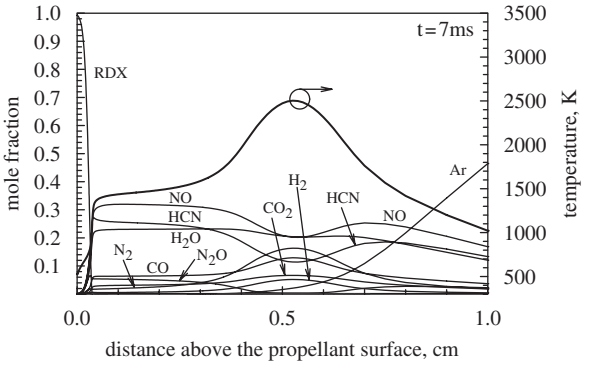

Fig. 46. Temperature and species–concentration profiles in gas phase for laser-induced ignition of RDX at $t = 7$ ms [21].

thermal decomposition, first oxidation, chemical preparation, second oxidation, and completion. In stage I, nitamines decompose to low molecular-weight species, such as CH_2O, N_2O, NO_2, HCN, and HONO. This process is basically thermally neutral, depending on the initial temperature. In stage II, oxidation reactions occur and release a significant amount of energy, with the temperature reaching about 1500 K. The heat release in stage II is mainly caused by the conversion of CH_2O and NO_2 to H_2O, NO, and CO, and to a lesser extent by the reactions of HCN and HONO. Stage III represents the chemical preparation period prior to the occurrence of the second oxidation reactions (stage IV). The reduction of HCN and NO to N_2, CO, H_2O, and H_2 is largely responsible for the heat release in stage IV. Finally, all the final products are formed; no further reactions occur in stage V.

Figs. 48 and 49 show the calculated and measured ignition delays of RDX and HMX, respectively,

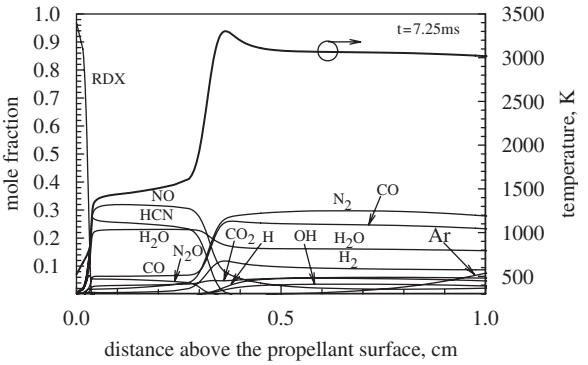

Fig. 47. Temperature and species–concentration profiles in gas phase for laser-induced ignition at $t = 7.25$ ms [21].

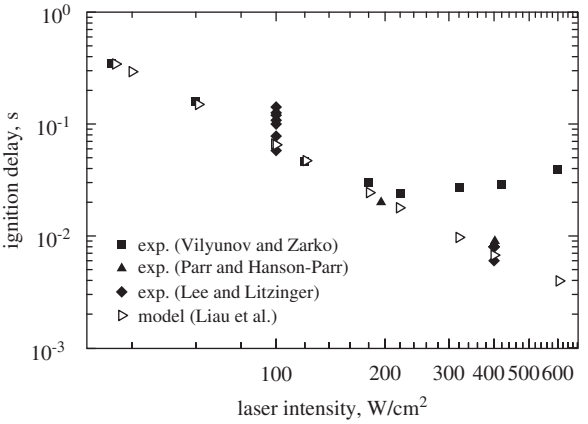

Fig. 48. Effect of CO_2 laser intensity on ignition delay of RDX monopropellant: predictions [21] and measurements [184,207,208].

induced by CO_2 laser under atmospheric pressure. The ignition delays are calculated based on the 'first light' criterion by detecting the appearance of CN flame. For RDX at 400 W/cm^2, the predicted ignition delay matches the measurements by Parr and Hanson-Parr [207] and Lee et al. [208]. However, the measured data of Vilyunov and Zarko [184] does not agree with the model prediction for laser intensities above 200 W/cm^2. The agreement for HMX is excellent for the entire range of laser intensities. Flame expansion (about 8 times at 2.0 cm above the surface) was incorporated in the HMX model according to the observations made in the experiments by Ali et al. [209]. Parr and Hanson-Parr [207] noticed a significant time lag between the first light and the go/no-go criterion (about 85–100 ms). The former was defined as the time when the luminous flame was first detected,

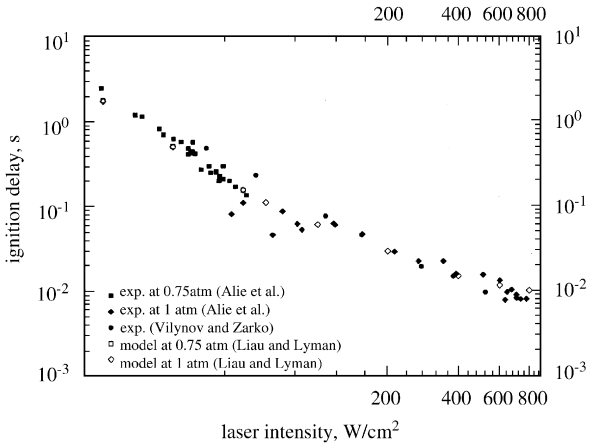

Fig. 49. Effect of CO_2 laser intensity on ignition delay of HMX monopropellant: predictions [111] and measurements [184,209].

whereas the latter was the time when a stable flame was achieved without the laser-assisted heating. The luminous flame progressed towards the propellant surface immediately after the first light, and then moved away from the surface after the maximum temperature gradient was achieved near the surface. The RDX ignition model [21], however, did not predict this type of flame movement. The luminous flame continuously progressed toward the surface until steady-state deflagration was achieved. The discrepancy between model predictions and experimental observations may be attributed to the heat loss to the surrounding. The entire ignition process was treated as adiabatic in the model. In reality, heat losses from both the gas-phase flame and the condensed-phase region to the surrounding environment may significantly affect ignition behavior.

9. Summary

Tremendous progress has been achieved during the last two decades in modeling the combustion and ignition of solid-propellant ingredients. There has been a paradigm shift in predictive capability, as the state-of-the-art has advanced from simple to detailed models. The earlier simple and global-kinetics type of models were based on parameters estimated from known experimental data, and could only predict the overall combustion characteristics, such as the burning rate as a function of pressure and initial temperature. In the case of detailed models, the treatment of the gas phase involves a variety of species undergoing a gamut of chemical reactions coupled with the processes of molecular

diffusion, convection, conduction, and radiation. The condensed-phase analysis includes global decomposition reactions and/or evaporation in the foam layer with subsequent reactions in the embedded bubbles. The recent comprehensive models are able to predict not only the burning-rate properties, but also the surface conditions and spatial structures of the entire combustion wave throughout both the condensed and gas phases. Various key parameters and underlying processes that dictate the propellant burning and ignition behavior have been identified.

The present work provides a comprehensive review of recent advances in modeling and simulation of solid-propellant ingredient combustion and ignition over a wide range of ambient conditions. The specific materials of concern include nitramines (RDX, HMX), azides (GAP), nitrate esters (NG, BTTN), ADN, and AP monopropellants, as well as their homogeneous mixtures representing binary (RDX/GAP, HMX/GAP, and AP/HTPB) and ternary (RDX/GAP/BTTN) pseudo-propellants. Good agreement between model predictions and experimental observations is achieved, except for processes in which the condensed-phase heat release plays a dominant role. Examples include the burning-rate irregularity of ADN as a function of pressure, the equilibrium flame temperature of GAP, and the burning-rate temperature sensitivity of HMX in the low-pressure range. The developed gas-phase kinetic mechanisms perform consistently well in representing the chemistry of monopropellants and their homogeneous mixtures, and have helped to explain the intricate processes of solid-propellant combustion better. It should be possible to extend the predictive capability to other ingredients of the same chemical families with relative ease. Most of the pseudo-propellant models discussed herein are based on the corresponding monopropellant models. It is likely that by assembling a large database of monopropellant models, a comprehensive mechanism capable of simulating pseudo-propellants of varying compositions and ingredients can be developed. With further improvements, the detailed models may fulfill the long-held hope of computing the effects of chemical additives on the burning rate in order to rationalize the performance tailoring of propellants. The current state of modeling thus appears to be headed towards more accurate and comprehensive predictions.

In spite of the accomplishments made so far, the present modeling techniques suffer from several deficiencies. One of the major constraints lies in the limited understanding of chemical reaction pathways and associated rate parameters in the condensed phase. The lack of experimental diagnostics and theoretical modeling at scales sufficient to resolve the underlying processes poses a serious challenge. All the existing models for the subsurface layer are based on a global treatment of the overall reaction, and consequently involve many uncertainties. Some of the reactions in the gas phase, especially the initial decomposition of those large molecules emerging from the propellant surface, need further investigation. The pressure and temperature dependence of the reaction mechanisms also warrant a careful study, such that the results can be applied to conditions representative of realistic system operations. In addition, thermophysical properties of many constituent species are not currently available over the range of the thermodynamic states of concern. A reliable database of properties is required. Another major constraint of existing models is the assumption of one-dimensional combustion-wave structure that neglects the effects of flame expansion and particle size. Modeling is thus not yet a predictive tool, but it is a useful guide. In the near future, it is likely that detailed combustion models can assist the formulation of advanced solid propellants meeting various performance and emission requirements.

Acknowledgments

This work was sponsored party by subcontracts from SEA, Carson City, NV, funded by ONR Contract N00014-02-C-0292, Judah Goldwasser as Contract Monitor, and partly by Brigham Young University and Pennsylvania State University.

References

[1] Kubota N. Survey of rocket propellants and their combustion characteristics. In: Kuo KK, Summerfield M, editors. Fundamentals of solid-propellant combustion, vol. 90. Progress in Astronautics and Aeronautics, AIAA; 1984. p. 1–52.

[2] Kubota N. Propellants and explosives, thermochemical aspects of combustion. Weinheim, Germany: Wiley-VCH; 2002.

[3] Beckstead MW. Overview of combustion mechanisms and flame structures for advanced solid propellants. In: Yang V, Brill TB, Ren WZ, editors. Solid propellant chemistry, combustion, and motor interior ballistics, vol. 185.

Progress in Astronautics and Aeronautics, AIAA; 2000. p. 267–85.
[4] Beckstead MW. Combustion mechanisms of composite solid propellants. In: 19th JANNAF combustion meeting, vol. II(CPIA No. 366), 1982, p. 93–100.
[5] Beckstead MW, Davidson JE, Jing Q. A comparison of solid monopropellant combustion and modeling. AIAA 97-0586, 1997.
[6] Liau Y-C, Yang V. Analysis of RDX monopropellant combustion with two-phase subsurface reactions. J Propulsion Power 1995;11(4):729–39.
[7] Davidson JE, Beckstead MW. A three-phase model of HMX combustion. In: 26th Symposium (international) on combustion, The Combustion Institute, Pittsburgh, 1996, p. 1989–96.
[8] Price CF, Boggs TL, Derr RL. Modeling of solid monopropellant deflagration. AIAA-78–219, 1978.
[9] Behrens R, Minier L. Thermal decomposition behavior of ammonium perchlorate and of an ammonium perchlorate based composite propellant. In: 33rd JANNAF combustion meeting, vol. I(CPIA No. 476), 1996.
[10] Yang R, Thakre P, Yang V. Thermal decomposition and combustion of ammonium dinitramide (review). Combust Explosion Shock Waves 2005;41(6):657–79.
[11] Puduppakkam KV, Beckstead MW. Combustion modeling of glycidyl azide polymer with detailed kinetics. Combust Sci Technol 2005;177(9):1661–97.
[12] Parr TP, Hanson-Parr DM. Optical diagnostics of solid-propellant flame structure. In: Yang V, Brill TB, Ren WZ, editors. Solid propellant chemistry, combustion, and motor interior ballistics, vol. 185. Progress in Astronautics and Aeronautics, AIAA; 2000. p. 381–412.
[13] Brill TB, Beckstead MW, Flanagan JE, Lin MC, Litzinger TA, Waesche RHW, et al. Chemical speciation and dynamics in the surface combustion zone of energetic materials. J Propulsion Power 2002;18(4):824–34.
[14] Gusachenko LK, Zarko VE. Combustion models for energetic materials with completely gaseous reaction products. Combust Explosion Shock Waves 2005;41(1): 20–34.
[15] Zenin AA. HMX and RDX: combustion mechanism and influence on modern double-base propellant combustion. J Propulsion Power 1995;11(4):752–8.
[16] Miller MS, Anderson WR. Energetic-material combustion modeling with elementary gas-phase reactions: a practical approach. In: Yang V, Brill TB, Ren WZ, editors. Solid propellant chemistry, combustion, and motor interior ballistic, vol. 185, 2000, p. 501–31.
[17] Davidson JE, Beckstead MW. Improvements to steady-state combustion modeling of cyclotrimethylenetrinitramine. J Propulsion Power 1997;13(3):375–83.
[18] Liau Y-C. A comprehensive analysis of RDX propellant combustion and ignition with two-phase subsurface reactions. PhD dissertation, Pennsylvania State University, 1996.
[19] Washburn EB, Beckstead MW. Modeling multi-phase effects in the combustion HMX and RDX. J Propulsion Power 2006;22(5):938–46.
[20] Kim ES, Yang V, Liau Y-C. Modeling of HMX/GAP pseudo-propellant combustion. Combust Flame 2002;131: 227–45.
[21] Liau Y-C, Kim ES, Yang V. A comprehensive analysis of laser-induced ignition of RDX monopropellant. Combust Flame 2001;126:1680–98.
[22] Kim ES. Modeling and simulation of laser-induced ignition of RDX monopropellant and steady-state combustion of HMX/GAP pseudo-propellant. PhD dissertation, The Pennsylvania State University, 2000.
[23] Liau Y-C, Yang V, Thynell ST. Modeling of RDX/GAP propellant combustion with detailed chemical kinetics. In: Yang V, Brill TB, Ren WZ, editors. Solid propellant chemistry, combustion, and motor interior ballistics. AIAA Progress in Astronautics and Aeronautics, vol. 185, 2000, p. 477–500.
[24] Miller MS. In search of an idealized model of homogeneous solid propellant combustion. Combust Flame 1982;46: 51–73.
[25] Merzhanov AG, Dubovitskii FI. Proc USSR Acad Sci 1959;129:153–6.
[26] Lengelle G. Thermal degradation kinetics and surface pyrolysis of vinyl ploymers. AIAA J 1970;8(11):1989–98.
[27] Beckstead MW, Derr RL, Price CF. A model of composite solid-propellant combustion based on multiple flames. AIAA J 1970;8(12):2200–7.
[28] Tseng IS, Yang V. Combustion of a double-base homogeneous propellant in a rocket motor. Combust Flame 1994;96:325–42.
[29] Mitani T, Williams FA. A model for the deflagration of nitramines. In: 21st symposium (international) on combustion. The Combustion Institute, Pittsburgh, 1986, p. 1965–74.
[30] Williams FA. Quasi-steady gas-phase flame theory in unsteady burning of a homogeneous solid propellant. AIAA J 1973;11:1328–30.
[31] Denison RM, Baum E. A simplified model of unstable burning in solid propellants. ARS J 1961;31(8):1112–22.
[32] Schultz RD, Dekker AO. In: Fifth symposium (international) on combustion. The Combustion Institute, Pittsburgh, 1960, p. 260.
[33] Beckstead MW, Derr RL, Price CF. The combustion of solid monopropellants and composite propellants. In: 13th symposium (international) on combustion. The Combustion Institute, Pittsburgh, 1971, p. 1047–56.
[34] Ward MJ, Son SF, Brewster MQ. Steady deflagration of HMX with simple kinetics: a gas phase chain reaction model. Combust Flame 1998;114(3–4):556–68.
[35] Beckstead MW, McCarty KP. Calculated combustion characteristics of nitramine monopropellants. In: 13th JANNAF combustion meeting, vol. I, 1976, p. 57–68.
[36] Gusachenko LK, Zarko VE. Analysis of contemporary models of steady state combustion of composite solid fuels. Combust Explosion Shock Waves 1986;22(6):643–53.
[37] Manelis GB, Strunin VA. The mechanism of ammonium perchlorate burning. Combust Flame 1971;17:69–77.
[38] Guirao C, Williams FA. A model for aluminium perchlorate deflagration between 20 and 100 atm. AIAA J 1971;9(7):1345–56.
[39] Ibiricu MM, Williams FA. Influence of externally applied thermal radiation on the burning rates of homogeneous solid propellants. Combust Flame 1975;24:185–98.
[40] Sohn HY. A unified theory of ammonium perchlorate deflagration and low-pressure deflagration limit. Combust Sci Technol 1975;10:137–54.

[41] Strunin VA, Firsov AN, Shkadinskii KG, Manelis GB. Stationary combustion of decomposing and evaporating comdensed substances. Combust Explosion Shock Waves 1977;13(1):1–9.
[42] Beckstead MW. Model for double-base propellant combustion. AIAA J 1980;18(8):980–5.
[43] Miller MS, Coffee TP. A fresh look at the classical approach to homogeneous solid propellant combustion modeling. Combust Flame 1983;50:65–74.
[44] Miller MS, Coffee TP. On the numerical accuracy of homogeneous solid monopropellant combustion models. Combust Flame 1983;50:75–88.
[45] Beckstead MW. Modeling AN, AP, HMX, and double base monopropellants. In: 26th JANNAF combustion meeting, vol. 4(CPIA No. 529), 1989, p. 255–68.
[46] Li SC, Williams FA, Margolis SB. Effects of two-phase flow in a model for nitramine deflagration. Combust Flame 1990;80:329–49.
[47] Louwers J, Gadiot GMHJL, Brewster MQ, Son SF, Parr TP, Hanson-Parr D. Steady-state hydrazinium nitroformate (HNF) combustion modeling. J Propulsion Power 1999;15(6):772–7.
[48] Brewster MQ, Ward MJ, Son SF. Simplified combustion modeling of double base propellant: gas phase chain reaction vs. thermal decomposition. Combust Sci Technol 2000;154:1–30.
[49] Kuznetsov IR, Stewart DS. Burning rate of homogeneous energy materials with thermal expansion and varying thermal properties in the condensed phase. Combust Theory Modeling 2005;9(2):255–72.
[50] Price CF, Boggs TL, Derr RL. The steady-state combustion behavior of ammonium perchlorate and HMX. AIAA-79-0164, 1979.
[51] Price CF, Boggs TL, Parr TP, Hanson-Parr DM. A modified BDP model applied to the self-deflagration of HMX. In: 19th JANNAF combustion meeting, vol. I(CPIA No. 366), 1982, p. 299–310.
[52] Price CF, Boggs TL. A simultaneous mathematical treatment of deflagration and ignition phenomena. In: 22nd JANNAF combustion meeting, vol. I(CPIA No. 432), 1985, p. 505–13.
[53] Price CF, Boggs TL. Transient combustion: an important aspect of deflagration-to-detonation transition. In: DeLuca L, editor. AIAA Progress Series, 1992, p. 143.
[54] BenReuven M, Caveny L, Vichnevetsky R, Summerfield M. Flame zone and sub-surface reaction model for deflagrating RDX. In: 16th international symposium on combustion. The Combustion Institute, Pittsburgh, 1976, p. 1223–33.
[55] BenReuven M, Caveny L. HMX deflagration and flame characterization. Report AFRPL-TR-79-94, vol. II, 1980.
[56] Cohen N, Lo G, Crowley J. Model and chemistry of HMX combustion. AIAA J 1985;23(2):276–82.
[57] Lengelle G, Bizot A, Duterque J, Trubert JF. Steady-state burning of homogeneous propellants. In: Kuo KK, Summerfield M, editors. Fundamentals of solid-propellant combustion, progress in astronautics and aeronautics, vol. 90, 1984, p. 361–98.
[58] Bizot A, Beckstead MW. A model for double base propellant combustion. In: 22nd international symposium on combustion. The Combustion Institute, Pittsburgh, 1988, p. 1827–34.
[59] Roh T-S, Tseng I-S, Yang V. Effects of acoustic oscillations on flame dynamics of homogeneous propellants in rocket motors. J Propulsion Power 1995;11(4):640–50.
[60] Price CF, Boggs TL, Bradley Jr HH. Modeling the combustion of monopropellants. In: 14th JANNAF combustion meeting, vol. I(CPIA No. 292), 1977, p. 307–24.
[61] Smooke MD, Yetter RA, Parr TP, Hanson-Parr DM. Modeling two-dimensional ammonium perchlorate diffusion flames. In: 36th JANNAF combustion meeting, vol. I(CPIA No. 691),1999, p. 359–68.
[62] Cai W, Yang V. A model of AP/HTPB composite propellant combustion. AIAA 2000-0311, 2000.
[63] Felt SA, Beckstead MW. A model of the AP/HTPB diffusion flame. In: 39th JANNAF combustion meeting, 2003.
[64] Knott GM, Brewster MQ. Modeling the combustion of propellant sandwiches. Combust Sci Technol 2002;174: 61–90.
[65] Massa L, Jackson TL, Short M. Numerical solution of three-dimensional heterogeneous solid propellants. Combust Theory Modeling 2003;7:579–602.
[66] Jackson TL, Buckmaster J. Heterogeneous propellant combustion. AIAA J 2002;40(6):1122–30.
[67] Massa L, Jackson TL, Buckmaster J. New kinetics for a model of heterogeneous propellant combustion. J Propulsion Power 2005;21(5):914–24.
[68] Ermolin NE, Zarko VE. Modeling of cyclic nitramine compounds. Combust Explosion Shock Waves 1998;34(5): 485–501.
[69] Ermolin NE, Korobeinichev OP, Tereshchenko AG, Fomin VM. Measurement of the concentration profiles of reacting components and temperature in an ammonium perchlorate flame. Combust Explosion Shock Waves 1982;18(1):46–9.
[70] Ermolin NE, Korobeinichev OP, Tereshchenko AG, Fomin VM. Kinetic calculations and mechanism definition for reactions in an ammonium perchlorate flame. Combust Explosion Shock Waves 1982;18(2):180–9.
[71] Ermolin NE, Korobeinichev OP, Tereshchenko AG, Fomin VM. Simulations of kinetics and chemical reaction mechanism of ammonium perchlorate burning. Sov J Chem Phys 1984;1(12):2872–83.
[72] Hatch RL. Chemical kinetics combustion model of the NG/binder system. In: 23rd JANNAF combustion meeting, vol. 1(CPIA No. 457), 1986, p. 157–65.
[73] Hatch RL. Chemical kinetics modeling of HMX combustion. In: 24th JANNAF combustion meeting, vol. 1(CPIA No. 476), 1987, p. 383–91.
[74] Ermolin NE, Korobeinichev OP, Kuibida LV, Fomin VM. Study of the kinetics and mechanism of chemical reactions in hexogen flames. Combust Explosion Shock Waves 1986;22(5):544–53.
[75] Melius CF. Thermochemical modeling, I: application to decomposition of energetic materials. Chem Phys Energetic Mater 1990:21–49.
[76] Melius CF. Thermochemical modeling, II: application to ignition and combustion of energetic materials. Chem Phys Energetic Mater 1990:51–78.
[77] Miller JA, Bowman CT. Mechanism and modeling of nitrogen chemistry in combustion. Prog Energy Combust Sci 1989;15(4):287–338.

[78] Yetter RA, Dryer FL, Allen MT, Gatto JL. Development of gas-phase reaction mechanism for nitramine combustion. J Propulsion Power 1995;11(4):683–97.
[79] Prasad K, Yetter RA, Smooke MD. An eigenvalue method for computing the burning rates of RDX propellants. Combust Sci Technol 1997;124:35.
[80] Chakraborty D, Lin MC. Gas-phase chemical kinetics of [C,H,O,N] systems relevant to combustion of nitramines. In: Yang V, Brill TB, Ren WZ, editors. Solid propellant chemistry, combustion, and motor interior ballistics, progress in astronautics and aeronautics, AIAA, vol. 185, 2000, p. 33–71.
[81] Cor JJ, Branch MR. Structure and chemical kinetics of flames supported by solid propellant combustion. J Propulsion Power 1995;11(4):704–16.
[82] Narahari HK, Mukunda HS, Jain VK. A model for combustion monopropellants (AP) with complex gas kinetics. In: 20th symposium (international) on combustion, The Combustion Institute, Pittsburgh, 1984, p. 2073–82.
[83] Sahu H, Sheshadri T, Jain V. Novel kinetics scheme for ammonium perchlorate gas phase. J Phys Chem 1990; 94:294–5.
[84] Cohen N. A review of kinetic models for high temperature gas phase decomposition of ammonium perchlorate. Aerospace report no. ATR-92(9558)-3, The Aerospace Corporation, 1992.
[85] Anderson WR, Ilincic N, Meagher NE, Seshadri K, Vanderhoff JA. Detalied and reduced chemical mechanisms for the dark zones of double base and nitramine propellants in the intermediate temperature regimes. In: 32nd JANNAF combustion meeting, vol. I(CPIA No. 638), 1995, p. 197.
[86] Park J, Chakraborty D, Lin MC. Thermal decomposition of gaseous ammonium dinitramide at low pressure: kinetic modeling of product formation with ad initio MO/cVRRKM calculation. In: 27th symposium (international) on combustion. The Combustion Institute, 1998, p. 2351–7.
[87] Homan BE, Miller MS, Vanderhoff JA. Absorption diagnostics and modeling investigations of RDX flame structure. Combust Flame 2000;120:301–17.
[88] Prasad K, Yetter RA, Smooke MD. An eigenvalue method for computing the burning rates of HMX propellants. Combust Flame 1998;115:406–16.
[89] Davidson JE, Beckstead MW. A mechanism and model for GAP combustion. In: 33rd JANNAF combustion meeting, vol. 2 (CPIA No. 653), 1996, p. 91–100.
[90] Puduppakkam KV. Modeling the steady-state combustion of solid propellant ingredients with detailed kinetics. PhD dissertation, Brigham Young University, 2003.
[91] Miller MS, Anderson WR. Burning-rate predictor for multi-ingredient propellants: nitrate-ester propellants. J Propulsion Power 2004;20(3):440–54.
[92] Puduppakkam KV, Beckstead MW. Combustion modeling of nitrate esters with detailed kinetics. AIAA-2005-3770, 2005.
[93] Jing Q, Beckstead MW, Jeppson MB. Influence of AP solid phase decomposition on temperature profile and sensitivity. AIAA 98-0448, 1998.
[94] Liau Y-C, Yang V, Lin MC, Park J. Analysis of ammonium dinitramide (ADN) combustion with detailed chemistry. In: 35th JANNAF combustion meeting, 1998 (CPIA No. 680).
[95] Korobeinichev OP, Bolshova TA, Paletsky AA. Modeling the chemical reactions of ADN in a flame. Combust Flame 2001;126:1516–23.
[96] Liau Y-C, Yang V, Lin MC, Park J. An improved model of ammonium dintramide (ADN). In: 36th JANNAF combustion meeting 1999.
[97] Kee RJ, Rupley FM, Miller JA. CHEMKIN II: A FORTRAN chemical kinetics package for the analysis of gas-phase chemical kinetics. Sandia report SAND89-8009, 1989.
[98] Kee RJ, Grcar JF, Smooke MD, Miller JA. A fortran program for modeling steady, laminar, one-dimensional, premixed flames. Sandia report SAND85-8240, 1985.
[99] Yang R, Thakre P, Liau Y-C, Yang V. Formation of dark zone and its temperature plateau in solid-propellant flames: a review. Combust Flame 2006;145(1):38–58.
[100] Puduppakkam KV, Beckstead MW. RDX/GAP pseudo-propellant combustion modeling. In: 38th JANNAF combustion meeting, vol. 1 (CPIA No. 712), 2002, p. 143–56.
[101] Jeppson MB, Beckstead MW, Jing Q. A kinetic model for the premixed combustion of a fine AP/HTPB composite propellant. In: 36th aerospace sciences meeting and exhibit AIAA 98-0447, 1998.
[102] Puduppakkam KV, Beckstead MW. Combustion modeling of RDX/GAP/BTTN pseudo-propellant. In: 39th JANNAF combustion subcommittee meeting, 2003.
[103] Yoon J-K, Thakre P, Yang V. Modeling of RDX/GAP/BTTN pseudo-propellant combustion. Combust Flame 2006;145:300–15.
[104] Flanagan JE, Woolery DO, Kistner RL. Combustion characteristics of GAP/RDX gumstocks. In: 24th JANNAF combustion meeting, vol. 3(CPIA No. 476), 1987, p. 29–38.
[105] Kubota N, Sonobe T. Burning rate catalysis of azide/nitramine propellants. In: 23rd international symposium on combustion, The Combustion Institute 1990:1331–37.
[106] Tang CJ, Lee YJ, Litzinger TA. The chemical and thermal processes of GAP/nitramine pseudo-propellants under CO_2 laser heating. In: 34th JANNAF combustion meeting, vol. II(CPIA No. 662), 1997, p. 491–504.
[107] Parr TP, Hanson-Parr DM. RDX/GAP/BTTN propellant flame studies. Combust Flame 2001;127(1–2):1895.
[108] Erikson WW, Beckstead MW. Modeling unsteady monopropellant combustion with full chemical kinetics. AIAA 98-0804, 1998.
[109] Erikson WW, Beckstead MW. Modeling pressure and heat flux responses of nitramine monopropellants with detailed chemistry. AIAA 99-2498, 1999.
[110] Yang V, Liau Y-C. A Time-accurate analysis of RDX monopropellant combustion with detailed chemistry. In: 32nd JANNAF combustion meeting, vol. I(CPIA No. 631), 1995, p. 57–68.
[111] Liau Y-C, Lyman JL. Modeling laser-induced ignition of nitramine propellants with condensed and gas-phase absorption. Combust Sci Technol 2002;174(3):141.
[112] Meredith KV, Beckstead MW. Laser-induced ignition modeling of HMX. In: 39th JANNAF combustion meeting, 2003.
[113] Meredith KV, Beckstead MW. Fast cook-off modeling of HMX. In: 39th JANNAF combustion meeting, 2003.
[114] Ermolin NE, Zarko VE. Investigation of the properties of a kinetic mechanism describing the chemical structure of

RDX flames, I: role of individual reactions and species. Combust Explosion Shock Waves 2001;37(2):123–47.
[115] Ermolin NE, Zarko VE. Investigation of the properties of a kinetic mechanism describing the chemical structure of RDX flames, II: construction of a reduced kinetic scheme. Combust Explosion Shock Waves 2001;37(3):247–54.
[116] Paletsky AA, Korobeinichev OP, Tereschenko AG, Volkov EN, Polyalov PD. Flame structures of HMX/GAP propellant at high pressure. In: Proceedings of the Combustion Institute, vol. 30, 2005, p. 2105–12.
[117] Atwood AI, Boggs TL, Curran PO, Parr TP, Hanson-Parr D, Price CF, et al. Burning rate of solid propellant ingredients, part 1: pressure and initial temperature effects. J Propulsion Power 1999;15(6):740–7.
[118] Atwood AI, Boggs TL, Curran PO, Parr TP, Hanson-Parr D, Price CF, et al. Burning rate of solid propellant ingredients, part 2: determination of burning rate temperature sensitivity. J Propulsion Power 1999;15(6):748–51.
[119] Korobeinichev OP, Kuibida LV, Orlov VN, Tereshchenko AG, Kutsenogii KP, Mavliev RV, et al. Mass spectrometric probe study of the flame structure and kinetics of chemical reactions in flames. Mass-Spektrom Khim Kinet 1985: 73–93.
[120] Hanson-Parr DM, Parr TP. RDX laser-assisted flame structure. In: 31st JANNAF combustion subcommittee meeting, vol. 2(CPIA No. 620), 1994, p. 407–23.
[121] Hanson-Parr DM, Parr TP. RDX flame structure. In: 25st symposium (international) on combustion. The Combustion Institute, 1994, p. 1635–43.
[122] Parr TP, Hanson-Parr DM. RDX, HMX, and XM39 self-deflagration flame structure. In: 32nd JANNAF combustion meeting, vol. I(CPIA No. 638), 1995.
[123] Litzinger TA, Fetherolf BL, Lee Y-J, Tang C-J. Study of the gas-phase chemistry of RDX: experiments and modeling. J Propulsion Power 1995;11(4):698–703.
[124] Tang CJ, Lee YJ, Kudva G, Litzinger TA. A study of the gas-phase chemical structure during CO_2 laser-assisted combustion of HMX. Combust Flame 1999;117: 170–88.
[125] Lee YJ, Tang CJ, Kudva G, Litzinger TA. The near-surface gas-phase structure of RDX during CO_2 laser-assisted combustion. In: 32nd JANNAF combustion meeting, vol. I(CPIA No. 638), 1995.
[126] Tang CJ, Lee Y, Litzinger TA. Simultaneous temperature and species measurements of the glycidyl azide polymer (GAP) propellant during laser-induced decomposition. Combust Flame 1999;117:244–56.
[127] Boggs TL. The thermal behavior of cyclotrimethylenetrinitramine (RDX) and cyclotetramethylenenitramine (HMX). In: Kuo KK, Summerfield M, editors. Fundamentals of solid-propellant combustion, progress in astronautics and aeronautics, vol. 90, 1984, p. 121–75.
[128] Kubota N, Sonobe T. Combustion mechanism of azide polymer. Propellants Explosives Pyrotech 1988;13:172–7.
[129] Kubota N, Sonobe T, Yamamoto A, Shimizu H. Burning rate characteristics of GAP propellants. J Propulsion Power 1990;6:686–9.
[130] Kubota N. Combustion of energetic azide ploymers. J Propulsion Power 1995;11(4):677–82.
[131] Flanagan JE, Woolery DO, Kistner RL. Fundamental studies of azide decomposition and combustion. AFRPL-TR-86-094 Edwards, CA, 1986.
[132] Korobeinichev OP, Kuibida LV, Volkov EN, Shmakov AG. Mass spectrometric study of combustion and thermal decomposition of GAP. Combust Flame 2002;129:136–50.
[133] Parr TP, Hanson-Parr DM. BTTN flame structure. 38th JANNAF combustion subcommittee meeting, vol. I(CPIA No. 712), 2002, p. 43–9.
[134] Roos BD, Brill TB. Thermal decomposition of energetic materials 82: correlations of gaseous products with the composition of aliphatic nitrate esters. Combust Flame 2002;128:181–90.
[135] Andreev KK. Thermal decomposition and combustion of explosives. Gosenergoizdat, 1957.
[136] Fetherolf BL, Litzinger TA. CO_2 laser-induced combustion of ammonium dinitramide (ADN). Combust Flame 1998;114:515–30.
[137] Korobeinichev OP, Kuibida LV, Paletstky AA, Shmakov AG. Development and application of molecular beam mass-spectroscopy to the study ADN combustion chemistry. J Propulsion Power 1998;14(6):991–1000.
[138] Litzinger TA, Lee Y-J, Tang C-J. Experimental study of nitramine/azide propellant combustion. In: Yang V, Brill TB, Ren WZ, editors. Solid propellant chemistry, combustion, and motor interior ballistics, Reston, VA, vol. 185, 2000, p. 355–79.
[139] Korobeinichev OP, Ermolin NE, Chernov AA, Emel'yanov ID. Flame structure, kinetics and mechanism of chemical reactions in flames of mixed composition based on ammonium perchlorate and polybutadiene rubber. Combust Explosion Shock Waves 1992;28(4):366–71.
[140] Parr TP, Hanson-Parr DM. HMX/GAP/BTTN propellant flame structure. In: 38th JANNAF combustion subcommittee meeting, 2002
[141] Chen JK, Brill TB. Thermal decomposition of energetic materials 50: kinetics and mechanism of nitrate ester polymers at high heating rates by SMATCH/FTIR spectroscopy. Combust Flame 1991;85:479–88.
[142] Hiyoshi RI, Brill TB. Thermal decomposition of energetic materials 83: comparison of the pyrolysis of energetic materials in air versus argon. Propellants Explosives Pyrotech 2002;2:23–30.
[143] Rice OK, Ginell R. The theory of the burning of double-base rocket powders. J Phys Colloid Chem 1950;54:929–52.
[144] Fifer RA. Chemistry of nitrate ester and nitramine propellants. In: Kuo KK, Summerfield M, editors. Fundamentals of solid propellant combustion, progress in astronautics and aeronautics, vol. 90, 1984, p. 177–219.
[145] Crawford BL, Huggett C, McBrady JJ. The mechanism of the burning of double-base propellants. J Phys Colloid Chem 1950;54(6):854–62.
[146] Wilfong RE, Penner SS, Daniels F. A hypothesis for propellant burning. J Phys Colloid Chem 1950;54(6): 863–71.
[147] Arisawa H, Brill TB. Thermal decomposition of energetic materials 71: structure-decomposition and kinetic relationships in flash of glycidyl azide polymer (GAP). Combust Flame 1998;112:533–44.
[148] Trubert JF, Duterque J, Lengelle G. Study of the condensed phase degradation and combustion of glycidyl azide polymer. In: 30th international annual conference of ICT, 1999.
[149] Haas Y, Eliahu YB, Welner S. Infrared laser-induced decomposition of GAP. Combust Flame 1994;96:212–20.

[150] Farber M, Harris SP, Srivastav RD. Mass spectrometric kinetic studies on several azido polymers. Combust Flame 1984;55:203–11.
[151] Goshgarian BB. The mechanism of nitramine and advanced propellant ingredient initial thermochemical decomposition. AFRPL-TR-82-040, Edwards Air Force Base, 1982.
[152] Chen JK, Brill TB. Thermal decomposition of energetic materials 54, kinetics and near-surface products of azide polymers AMMO, BAMO and GAP in simulated combustion. Combust Flame 1991;87:157–68.
[153] Dhar SS, Singh H. Burn rate & catalysis behavior of GAP based CMDB propellants. In: Joint propulsion conference, AIAA 95-2586, 1995.
[154] Korobeinichev OP, Kuibida LV, Shmakov AG, Paletsky AA. GAP decomposition and combustion chemistry studied by molecular beam mass-spectrometry. In: 37th AIAA aerospace sciences meeting and exhibit, 1999, AIAA-99-0596.
[155] Oyumi Y. Thermal decomposition of azide polymers. Propellants Explosives Pyrotech 1992;17:23–231.
[156] Kimura E, Oyumi Y. Effects of copolymerization ratio of BAMO/NMMO and catalyst on sensitivity and burning rate of HMX propellant. Propellants Explosives Pyrotech 1995;20:215–21.
[157] Brill TB. Multiphase chemistry considerations at the surface of burning nitramine monopropellants. J Propulsion Power 1995;11(4):740–51.
[158] Sysak GS, Kim ES, Thynell ST. Decomposition rates of glycidyl azide polymer from confined rapid thermolysis/infrared spectroscopic technique. In: 35th JANNAF combustion meeting, 1998.
[159] Kraeutle KJ. The response of ammonium perchlorate to thermal stimulus. In: Boggs TL, editor. Response of ammonium perchlorate to thermal and mechanical shock stimuli. China Lake, CA: Naval Weapons Centre; 1990.
[160] Frenklach M, Bowman T, Smith G, Gardiner B. GRI-MECH 3.0. Downloaded from 〈http://www.me.berkeley.edu/gri_mech/〉
[161] Ermolin NE. Model for chemical reaction kinetics in perchloric acid-ammonia flames. Combust Explosion Shock Waves 1995;31(5):555–65.
[162] Park J, Lin MC. A mass spectrometric study of the $NH_2 + NO_2$ reaction. J Phys Chem A 1997;101(14):343–7.
[163] Hanson-Parr DM, Parr TP. Thermal properties measurements of solid rocket propellant oxidizers and binder materials as a function of temperature. J Energetic Mater 1999;17:1–49.
[164] Bedrov D, Smith GD, Sewell TD. Thermal conductivity of liquid HMX from molecular dynamics simulations. Chem Phys Lett 2000;324:64–8.
[165] Taylor JW. Crookes. J Chem Soc Faraday Trans I 1976;72:723–9.
[166] Maksimov YuYa. Zhur Fiz Khim 1992;66:540–42.
[167] Hall PG. Trans Faraday Soc 1971;67:556–62.
[168] Kubota N. Determination of plateau burning effect of catalyzed double-base propellant. In: 17th international symposium on combustion. The Combustion Institute, 1979, p. 1435–41.
[169] Zenin AA, Finjakov SV. Physics of GAP combustion. In: 38th aerospace sciences meeting & exhibit, AIAA 2000-1032, 2000.
[170] Zenin AA, Puchkov VM, Finjakov SV. Physics of ADN combustion. AIAA-99-0595, 1999.
[171] Parr TP, Hanson-Parr DM. 2003. Private Communication.
[172] Frankel MB, Grant LR, Flanagan JE. Historical development of glycidyl azide polymer. J Propulsion Power 1992;8:560–3.
[173] Zimmer-Galler R. Correlations between deflagration characteristics and surface properties of nitramine-based propellants. AIAA J 1968;6(11):2107–10.
[174] Glaskov AP. The effect of catalysts on the combustion of explosives. Fiz Goreniya i Vzryva 1974;10(3):323–34.
[175] Fogelzang AE. Combustion of explosives and propellants. Database FLAME, Version 2.43, 1996.
[176] Zenin AA. Structure of the temperature distribution in the steady combustion of a double-base propellant. Combust Explosion Shock Waves 1966;2:67–76.
[177] Eisenreich N. A photographic study of the combustion zones of burning double base propellant strands. Propellants Explosives 1978;3:141–6.
[178] Heller CA, Gordon AS. Structure of the gas phase combustion region of a solid double base propellant. J Phys Chem 1955;59:773–7.
[179] Foster RL, Miller RR. The burn rate temperature sensitivity of aluminized and non-aluminized HTPB propellants. 1980 JANNAF propulsion meeting, vol. IV(CPIA No. 315), 1981, p. 667–93.
[180] King MK. Model for steady state combustion of unimodal composite solid propellants. In: AIAA 16th aerospace sciences meeting, AIAA paper 1978, p. 78–216.
[181] Price EW, Bradley Jr HH, Dehority GL, Ibiricu MM. Theory of ignition of solid propellants. AIAA J 1966;4:1153–81.
[182] Kulkarni AK, Kumar M, Kuo KK. Review of solid-propellant ignition studies. AIAA J 1982;20:243–4.
[183] Hermance CE. In: Kuo KK, Summerfield M, editors. Fundamentals of solid propellant combustion. Progress in astronautics and aeronautics series, AIAA, 1984, 90, p. 239–304.
[184] Vilyunov VN, Zarko VE. Ignition of solids. New York: Elsevier Science Publishers; 1989.
[185] Strakouskiy L, Cohen A, Fifer R, Beyer R, Forch B. Laser ignition of propellants and explosives. ARL-TR-1699, Army Research Laboratory Aberdeen Proving Ground, MD, 1998.
[186] Baer SD, Ryan NW. An approximate but complete model for the ignition response of solid propellants. AIAA J 1968;6:872–7.
[187] Bradley Jr HH. Theory of igntion of a reactive solid by constant energy flux. Combust Sci Technol 1970;2:11–20.
[188] Linan A, Williams FA. Theory of igntion of a reactive solid by constant energy flux. Combust Sci Technol 1971;3:91–8.
[189] Linan A, Williams FA. Radiant ignition of a reactive solid with in-depth absorption. Combust Flame 1972;18:85–97.
[190] Williams FA. Theory of propellant ignition by heterogeneous reaction. AIAA J 1966;4:1354–7.
[191] Waldman CH, Summerfield M. Theory of propellant ignition by heterogenous reaction. AIAA J 1969;7:1359–61.
[192] Waldman CH. Theory of heterogenous ignition. Combust Sci Technol 1970;2:81–93.
[193] Bradley Jr HH, Williams FA. Theory of radiant and hypergolic ignition of solid propellant. Combust Sci Technol 1970;2:41–52.

[194] Andersen WH. Theory of surface ignition with application to cellulose, explosives, and propellants. Combust Sci Technol 1970;2:213–21.
[195] Andersen WH. Analysis of ignition behavior of M2 propellants. Combust Sci Technol 1972;5:43–6.
[196] Andersen WH. Model of transient ignition of self-sustained burning. Combust Sci Technol 1972;5:75–81.
[197] Linan A, Crespo A. An asymptotic analysis of radiant and hypergolic heterogeneous ignition of solid propellants. Combust Sci Technol 1972;6:223–32.
[198] Niioka T. Heterogeneous ignition of a solid fuel in a hot stagnation-point flow. Combust Sci Technol 1978;18: 207–15.
[199] Hermance CE, Shinnar R, Summerfield M. Ignition of an evaporating fuel in a hot oxidizing gas, including the effect of heat feedback. Astronautica Acta 1966;12:95–112.
[200] Kashiwagi T, MacDonald BW, Isoda H, Summerfield M. Ignition of the hot polymeric fuel in a hot oxidizing gas stream. In: 13th symposium (international) on combustion, Combustion Institute, Pittsburgh, 1971, p. 1073–86.
[201] Hermance CE, Kumar RK. Gas phase ignition theory for homogeneous propellants under shock tube conditions. AIAA J 1970;8:1551–8.
[202] Kumar RK, Hermance CE. Ignition of homogeneous solid-propellants under shock tube conditions. AIAA J 1971;9: 1615–20.
[203] Kumar RK, Hermance CE. Gas phase ignition theory of a heterogeneous solid propellant. Combust Sci Technol 1972;4:191–6.
[204] Kumar RK, Hermance CE. Role of gas-phase reactions during radiant ignition of solid propellants. Combust Sci Technol 1976;14:169–75.
[205] Kindelan M, Williams FA. Gas-phase ignition of a solid with in-depth absorption of radiation. Combust Sci Technol 1977;16:47–58.
[206] Ritchie S, Thynell S, Kuo KK. Modeling and experiments of laser-induced ignition of nitramine propellants. J Propulsion Power 1997;13(3):367–74.
[207] Parr TP, Hanson-Parr DM. RDX ignition flame structure. In: 27th symposium (international) on combustion, The Combustion Institute, Pittsburgh, 1998, p. 2301–8.
[208] Lee YJ, Litzinger TA. Private Communication, 1995.
[209] Ali AN, Son SF, Sander RK, Asay BW. Ignition dynamics of high explosives. AIAA 99-0862, Washington, DC, 1999.
[210] Hanson-Parr DM, Parr TP. Private Communication, 2005.